Measuring Vegetation Structure and Modeling Ecological Functions for a Heterogeneous Savanna Ecosystem in California

by

Qi Chen

B.S. (Nanjing University, China) 1998
M.S. (Nanjing University, China) 2001

A dissertation submitted in partial satisfaction of the
requirements for the degree of
Doctor of Philosophy

in

Environmental Science, Policy, and Management

in the

GRADUATE DIVISION

of the

UNIVERSITY OF CALIFORNIA, BERKELEY

Committee in charge:

Professor Peng Gong, Co-Chair
Professor Dennis D. Baldocchi, Co-Chair
Professor Greg Biging
Professor Maggi Kelly
Professor Todd Dawson

Spring 2007

The Dissertation of Qi Chen is approved:

Co-Chair Date

Co-Chair Date

Date

Date

Date

University of California, Berkeley

Spring 2007

Measuring Vegetation Structure and Modeling Ecological Functions for a Heterogeneous Savanna Ecosystem in California

by

Qi Chen

Abstract

Measuring Vegetation Structure and Modeling Ecological Functions for a Heterogeneous Savanna Ecosystem in California

by

Qi Chen

Doctor of Philosophy in Environmental Science, Policy, and Management

University of California, Berkeley

Professor Peng Gong, Co-Chair

Professor Dennis D. Baldocchi, Co-Chair

Western savanna is one of the most complex ecosystems due to its horizontal and vertical heterogeneity. It is generally assumed that individual-tree based models are needed to capture canopy structure at utmost details so that the radiation and ecological processes can be model realistically. Accompanying that, there are two fundamental research questions for modeling such a heterogeneous landscape: 1) how to parameterize an individual-tree based model at the landscape level, especially with the aid of remote sensing, and 2) since it is unrealistic to apply individual-tree model at the regional and global scales, is it possible to develop simple models that can achieve comparable performance as individual-tree models? If yes, how?

To address these two research questions, this dissertation is divided into two parts. This first part includes three chapters which introduce how I use an innovative remote sensing technology called LIDAR (Light Detection and Ranging) to extract the

individual-tree structural information at the landscape level. The three chapters presents the methods I have developed for processing LIDAR data and extracting canopy structure information. In the second part, I proposed an analytical approach to calculate clumping factors, which are used in a Markov big-leaf model for estimation radiation and ecological processes. It was found that the Markov big-leaf model can achieve comparable performance as individual-tree based model, which indicates its potential in broad-scale biosphere-atmosphere modeling and global climate change studies.

Prof. Peng Gong, Committee Co-Chair

Prof. Dennis Baldocchi, Committee Co-Chair

Acknowledgements

First of all, I would like to thank my advisors Prof. Peng Gong and Prof. Dennis Baldocchi for their support and guidance in almost every aspect of my life at UC, Berkeley. Prof. Peng Gong gives me freedom to develop my research interests, sets a high standard for me just as for himself, teaches me how to cope with difficult encounters not only in research but also in personal life, and provides me generous help in uncountable occasions. I am also deeply thankful for Prof. Dennis Baldocchi, who helps me to develop my dissertation topic in his course, who never hesitates to provide his best support in my research and studies, who can always pull out a long list of papers from his computer and file cabinet whenever I have a research question, who gives ovations for every little move I made. Their knowledge and personality are lifetime fortune for me. I am very grateful to Prof. Greg Biging, Prof. Maggi Kelly, and Prof. Todd Dawson for their constructive and insightful comments in improving my research and their generous help in my academic career.

I am also indebted to Prof. Yong Tian, Prof. Ruiliang Pu, Dr. Jianwu Tang, and Dr. Liukang Xu who share me their knowledge and successful experiences and help me in field work. Special thanks are given to Richard Battrick and Cora Basada for their kind administrative help that makes my life at Berkeley easy and enjoyable.

Finally, this dissertation is dedicated to my wife and parents. I cannot imagine the life without their support.

Contents

List of Figures

List of Tables

Chapter 1 Filtering Airborne Laser Scanning Data with Morphological Methods

Abstract

Filtering methods based on morphological operations have been developed in some previous studies. The biggest challenge for this kind of methods is how to keep the terrain features unchanged while using large window sizes for morphological opening. Zhang *et al.* (2003) tried to achieve this goal but their method required the assumption that the slope is constant. This paper presents a new method to achieve this goal without such restrictions. Besides, methods for filling missing data and removing outliers are proposed. The experimental test results using the ISPRS Commission III/WG3 dataset show that this method performs well for most sites, except those with missing data due to the lack of overlap between swaths. This method also shows encouraging results for laser data with low pulse density.

1 Introduction

Airborne laser scanning (ALS) is gaining popularity in various environmental applications, ranging from DEM mapping, transportation, and urban studies to forest management, hydrology, and ecology (Flood and Gutelius, 1997). Compared with digital photogrammetry (Gong *et al*., 2000; Sheng *et al*., 2001; Gong *et al*., 2002) and radar interferometry (Hoekman and Varekamp, 1998), laser altimetry has the advantage of recording the elevation of earth surface directly. Nevertheless, there is a great need of efficient data processing methods (Axelsson, 1999). In particular,

filtering, the abstraction of bare earth from ALS points is a crucial procedure for ALS data processing (Sithole and Vosselman, 2004). It, with quality control, generally consumes an estimated 60 to 80% of processing time (Flood, 2001). However, the details of filtering algorithms were seldom reported due to the tendency of some commercial and academic practitioners to keep their work proprietary (Haugerud and Harding, 2001; Huising and Gomes Pereira, 1998; Haugerud and Harding, 2001; and Sithole and Vosselman, 2004).

Sithole and Vosselman (2004) divided current filtering algorithms into four categories including slope-based, block-minimum, surface-based, and clustering/segmentation methods, among which the surface-based method is widely used. The idea of surface-based methods is to create a surface with a corresponding buffer zone above it and the buffer zone defines the region in 3D space where terrain points are expected to reside (Sithole and Vosselman, 2004). The key of this method is to create a surface approximating the bare earth. Depending on the means of creating the surface, surface-based filtering methods can be further divided into the following two subcategories:

1) *Interpolation-based methods*: Kraus and Pfeifer (1998) proposed an algorithm to iteratively approximate the ground using weighted linear least squares interpolation. Since terrain points usually have negative residuals and non-terrain points have positive ones, a weight function was designed to assign high weight to the points with negative residuals. This algorithm was extended by incorporating the hierarchical approach (Pfeifer *et al*., 2001) and it was found that the hierarchical interpolation can improve the filter result and speed up the computation. Lee and Younan (2003) improved Kraus and Pfeifer's method by replacing the least squares

method with a normalized least squares method called adaptive line enhancement (ALE). The implementation of ALE required *a priori* knowledge of a number of parameters such as the delay factor and the adaptation parameter. In another study, iterative regression was also used by Brandtberg *et al*. (2003) to derive DEM in a forest area.

2) *Morphological methods*: The idea of morphological methods is approximating the terrain surface using morphological operations such as opening. Compared with other methods, morphological methods are conceptually simple and can be easily implemented. When there are enough pulses reaching the ground, morphological opening with a small window size can effectively remove the surface objects and generate a surface approximating the ground. However, when there are not many pulses hitting the ground, such as the places where buildings are located, the window size for morphological opening has to be large to remove the objects. The problem of using a morphological opening with larger window sizes is that it will produce a surface with more protruded terrain features flattened. Therefore, how to keep the terrain features unchanged while using large window sizes for opening is the biggest challenge.

Some researchers have made efforts in trying to solve this problem. Kilian *et al.* (1996) used different window sizes into their data set starting from the smallest one; then each point was assigned a weight related to the window size if it was classified as a ground point, and the terrain surface was estimated by using all points with assigned weights. Zhang *et al*. (2003) proposed a method to remove surface objects while preserving terrain using gradually increased window sizes. They compared the elevation difference between surfaces after morphological opening with successively increased window sizes. If the elevation difference of a point was less

than a threshold, it was classified as a terrain point. The threshold was determined by the terrain slope. The major limitation of this method is that it assumed the slope over an area is constant and the slope had to be chosen by iteratively comparing the filtered and unfiltered data. The assumption of a constant slope is not always realistic, especially for complex scenes. If the actual terrain slope is greater the predetermined slope, the points will be classified as non-terrain points. Correspondingly, the omission errors of identifying terrain points will increase.

The objective of this paper is to present a method that can remove non-ground objects and preserve terrain features during the morphological opening, even with large window sizes. Similar to Zhang *et al*. (2003)'s method, progressively increased window sizes are used for morphological operations. However, the method of this study doesn't require the assumption of a constant slope. The method is developed based on the fact that non-terrain objects such as buildings usually have abrupt elevation changes along their boundaries while the change of terrain elevation is gradual and continuous. Since this fact typically holds, this method is adaptive to local terrain and can readily work over rugged areas. To evaluate its performance, this method is compared with a benchmark study conducted by ISPRS (International Society for Photogrammetry and Remote Sensing) Commission III/WG 3 (Sithole and Vosselman, 2004), which tested eight filtering algorithms over sites ranging from urban to rural areas with different complexity.

2 Method

This section is organized as follows: 1) for completeness, some concepts of morphological operations are revisited first, and the remainder of this section introduces the steps of processing; 2) the first step of this method is to fill missing

data since missing data exist in the dataset we used; 3) after missing data have been filled and a grid has been created, the objects on the ground can be removed by morphological opening with progressively increased windows sizes. Vegetated areas typically require smaller window sizes than built areas since laser pulses can penetrate canopy and reach the ground. In this step, how to determine the minimum window size in vegetated areas is discussed. After a morphological opening with the minimum window size, trees have been removed in the surface, with large objects such as buildings remaining; 4) a common issue in the data set is the existence of outliers, which are unrealistically higher or lower than their surrounding terrain. The higher outliers can be removed in the morphological opened surface, while the lower outliers cannot. Therefore, a method is developed to detect the lower outliers and fill the surface; 5) after the trees and outliers are removed, the next step is to remove large artificial objects such as buildings. An algorithm is designed to remove buildings using progressively increased window sizes and avoid cutting terrain features; and 6) finally, terrain points are extracted from the approximated surface and a DEM is generated.

2.1 Morphological Operations

Mathematical morphology stems from set theory and is widely used in image processing (Soille, 2003). The basic operations in mathematical morphology are erosion and dilation, which are performed over a neighborhood specified by a structural element. The erosion of a set X by a structural element *B* is denoted by:

$$[\varepsilon_B(\mathrm{X})](x) = \min\{x_B\} \tag{1}$$

where $[\varepsilon_B(\mathrm{X})](x)$ means the erosion of x in X with structural element *B* and x_B

means values within x's neighborhood specified by B. Conversely, the dilation of a set X by a structural element B is:

$$[\delta_B(\mathrm{X})](x) = \max\{x_B\} \tag{2}$$

Consider a one-dimensional laser point series evenly distributed (Figure 1.1 (a)): erosion is to obtain the elevation of the lowest point within its neighborhood and dilation is to obtain the elevation of the highest point within its neighborhood. Based on erosion and dilation, two other operations, opening and closing, can be derived. Opening means erosion followed by dilation while closing means dilation followed by erosion. A nice property of opening is that it can remove "outstanding" objects smaller than the specified neighborhood window size. For example, when the neighborhood of a point is defined to be its nearest three points, the tree B in Figure 1.1 will be removed (Figure 1.1(b)) and the elevation of each point will be updated with the value after morphological opening. The updated elevation can approximate the bare earth well, especially over flat areas. Comparing the original elevation with the opened elevation of each laser point, a laser point will be classified as a terrain point if the difference is less than a threshold, otherwise it will be an object point.

The importance of window sizes can be demonstrated in Figure 1.1. Whatever a window size is, the morphological opening will flatten any protruded terrain feature within the window size (see C in Figures 1.1 (b) and (c)). When a larger window size is needed to remove large objects such as building A, more terrain will be flattened and cut off. This can be observed by comparing the terrain after opening around the location C in Figures 1.1(b) and (c).

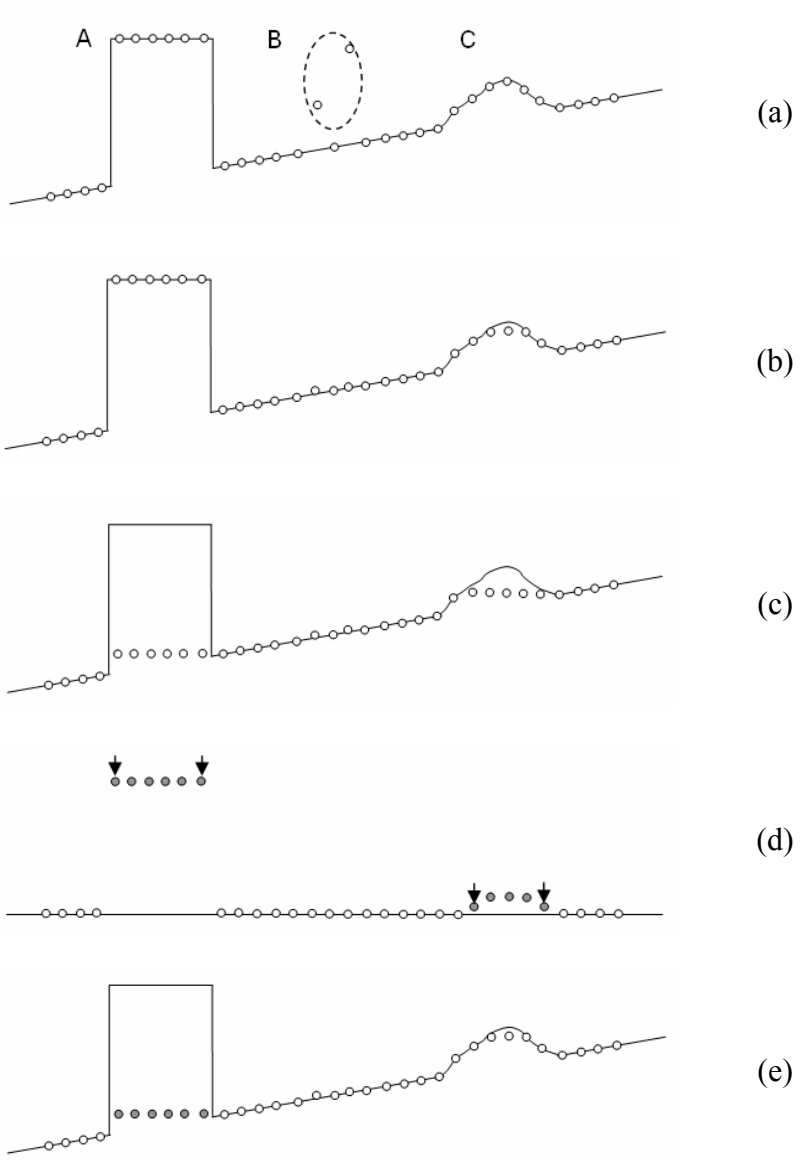

Figure 1.1. Example of one-dimensional laser points. (a) measured points, (b) points whose elevations are updated by opening with a neighborhood of 3 (*originalOpen*), (c) points whose elevations are updated by opening with a neighborhood of 7 (*newOpen*), (d) the point-wise difference between *originalOpen* and *newOpen*, and (c), and (e) the updated *originalOpen* after one iteration (the gray points are the updated points).

2.2 Rasterization and Filling Missing Data

Morphological operations are typically performed over a grid. Thus, the first step of this method is to record the elevation of the last return of each pulse into a grid.

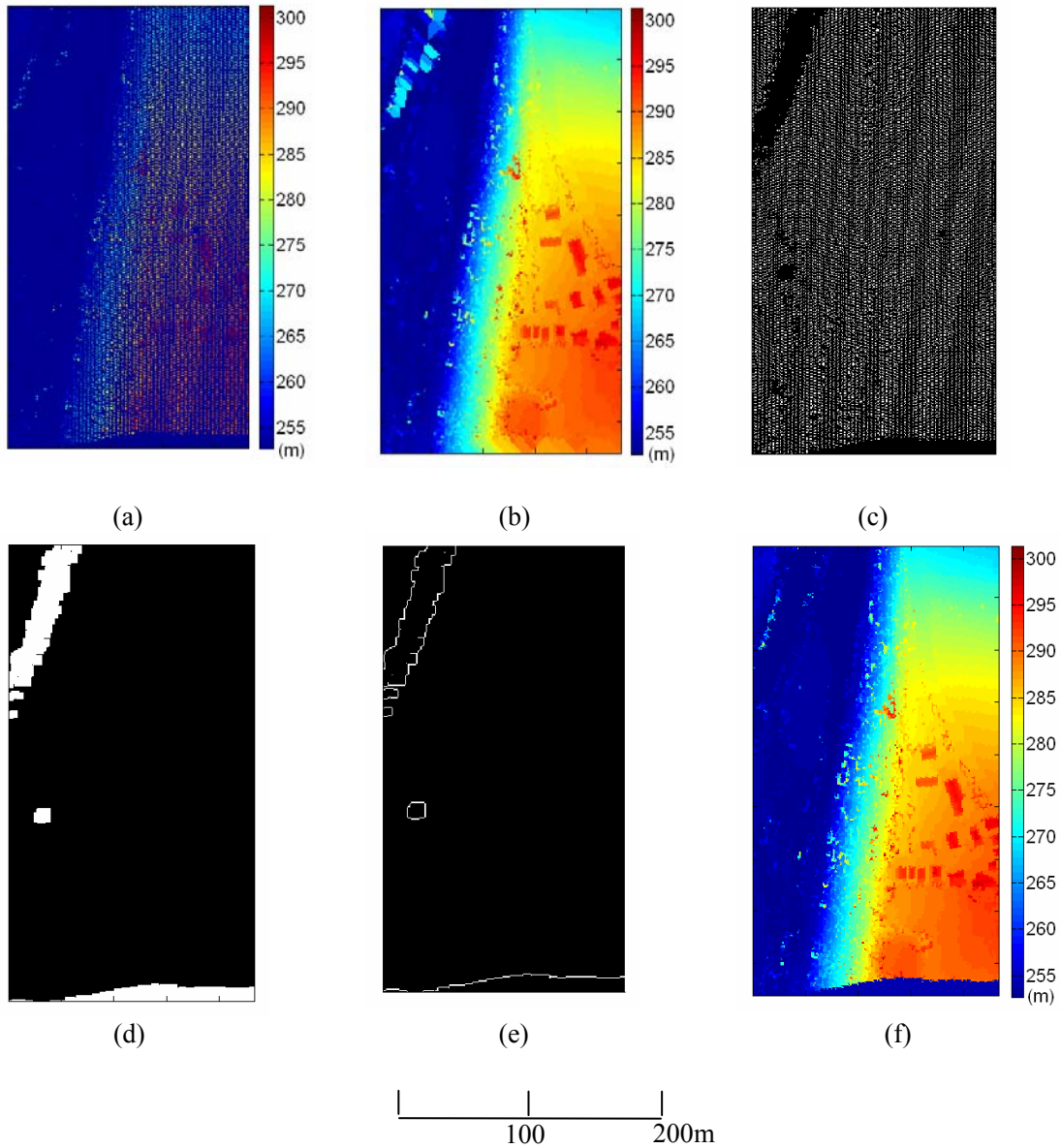

Figure 1.2. Rasterization and missing data filling. (a) $g_{\min}$, (b) filled raster with the nearest elevation before filling missing data, (c) binary grid indicating whether there are pulses within it, (d) the areas of missing data, (e) the boundary of each area in (d), and (f) filled raster with the nearest elevation after filling missing data.

Because the minimum point spacing for the data used in this study is about 1m, the grid size is set to be 1m by 1m. If there are several pulses falling in one cell, only the minimum elevation is recorded. This grid is denoted as $g_{\min}$ (Figure 1.2(a)). As in Zhang *et al*. (2003), the X and Y positions of the lowest pulse for each cell are also

recorded. When the pulse spacing is greater than the 1m, there are no values for some cells. For these cells, the general strategy is to iteratively fill them with the elevation of the nearest cell that has a value. However, problems occur when there are large areas of missing data. In the upper-left of the area shown in Figure 1.2 exist missing data caused by the water in the river since water is highly absorptive in the laser wavelength (1064nm for the Optech instrument). There are trees alongside the river, leading to artifacts in the filled grid (Figure 1.2(b)).

Missing data could be resulted in typically due to three factors: 1) lack of overlap between laser swaths. Usually, side overlap is required between laser swaths to guarantee continuous data coverage, but data gaps can be produced due to the yaw, roll, and pitch of the airplane, 2) instrument malfunction, and 3) absorption of laser pulses by highly absorptive materials, typically water body. The first two problems can be avoided by well prepared operations. However, the missing data caused by absorptive materials have to be filled with some data processing techniques. Since water is the most typical material that causes large-area absorption, a technique for filling missing data is developed as follows specifically for water. Based on the fact that water usually has the lowest elevation among the adjacent areas, this technique is to find the areas of missing data and fill each area with the lowest elevation around it:

a) Locate the areas of having missing data. This is accomplished by 1) first creating a binary image where 1 stands for cells which have values and 0 for cells with no data (Figure 1.2(c)), and 2) then morphologically closing (dilation followed by erosion) this binary image with a “disk” structural element with radius *r*:

$$r = (\frac{1}{d})^{0.5} \cdot \frac{1}{c} \quad (3)$$

where d is the pulse density (number of pulses per square meter) and can be calculated from the raw data, c is the cell size in meter. $(\frac{1}{d})^{0.5}$ is the average distance between pulses, therefore, $(\frac{1}{d})^{0.5} \cdot \frac{1}{c}$ is the average cell number between two cells with values. After closing, the data gaps caused by sparse pulse density disappear and the large areas with missing data can be found (Figure 1.2(d));

b) For each area, replace the values of $g_{\min}$ with the lowest elevation of cells within the boundary of each area. The boundary of each area is found by subtracting original area from the dilated area (Figure 1.2(e)). The structural element for dilating each area is a "disk" with radius 1;

c) For the above modified $g_{\min}$, iteratively replace the cells of no values with the elevation of the nearest cell that has a value (Figure 1.2(f)). The difference between Figure 1.2(b) and Figure 1.2(f) shows the effects of missing data filling.

This filled grid is denoted as $g_{f\min}$, each cell of which records the elevation of the nearest and lowest last return of laser pulses.

2.3 Filtering over Areas with Trees

In vegetated areas, the bare earth can be approximated by morphological opening $g_{f\min}$. As mentioned earlier, the window size used in morphological opening is critical. Consider laser point cloud in Figure 1.3(a). They could hit on three

completely different surfaces: 1) three trees above a flat terrain (Figure 1.3(b)), 2) three short vegetation (such as shrubs) over a slightly protruding terrain (Figure 1.3(c)), and 3) an over-rugged terrain (Figure 1.3(d)). Therefore, it is theoretically impossible to differentiate vegetation and terrain pulses and therefore choose window sizes only based on the spatial arrangement of laser points.

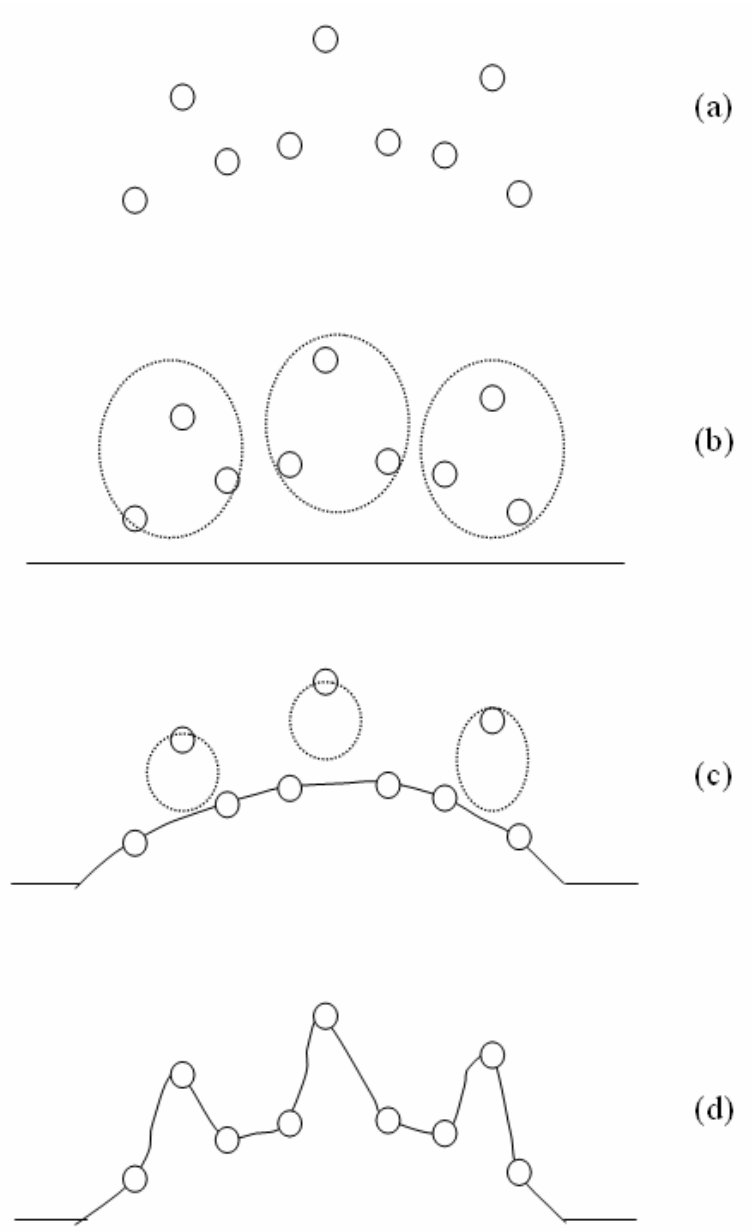

Figure 1.3. (a) arbitrary point cloud, which could hit (b) on three trees (indicated by dashed line), (c) on vegetation and terrain, and (d) on terrain only.

The morphologically opened grid can approximate the bare earth better using the neighborhood window size containing at least one terrain return than larger window sizes. For example, if it is known that there is at least one terrain return every two laser pulses such as in Figure 1.3(c), the neighborhood window size can be set to be its nearest three laser pulses (including itself). Therefore, ideally, the window size should be as small as possible but containing at least one terrain pulse. However, it is difficult to know whether there is at least one terrain pulse within a certain neighborhood window size. In practice, such a window size can be found by morphologically opening the filled grid $g_{f\min}$ with different window sizes and choosing the smallest one that can visually produce a smooth terrain. With such a method, it is possible to remove most, if not all, vegetation. This window size is denoted as d_{min}. The opened grid of $g_{f\min}$ with d_{min} is called $g_{o(f\min)}$.

2.4 Low Outliers Detecting and Filling

There are two kinds of outliers in the datasets of this study: high outliers and low outliers. Commonly, high outliers emerge from laser returns from birds, aircrafts, etc. and low outliers come from pulses that are reflected for several times or malfunction of a laser rangefinder (Sithole and Vosselman, 2004). High outliers can be removed by morphological opening. Thus, there are usually no high outliers in the opened grid $g_{o(f\min)}$. However, low outliers still exist (Figure 1.4(a)). Low outliers are assumed to be: 1) *h* meters lower than its surrounding cells, and 2) scattered. Based on these, low outliers are detected and filled as follows:

a) Compute the extended-minima transform of $g_{o(f\min)}$, denoted as $EMIN_h(g_{o(f\min)})$. $EMIN_h(g_{o(f\min)})$ is the regional minima of the h-minima

transform of $g_{o(f\min)}$. The h-minima transformation of the $g_{o(f\min)}$ is to perform the reconstruction by erosion of $g_{o(f\min)}$ from $g_{o(f\min)}+h$.

$$g_{o(f\min),\,h\min}=\mathrm{R}^{\varepsilon}_{g_{o(f\min)}}(g_{o(f\min)}+h) \tag{4}$$

where $g_{o(f\min),\,h\min}$ is the h-minima transformation of $g_{o(f\min)}$ (Soille, 2003). The regional minima of $g_{o(f\min),\,h\min}$, $\mathrm{EMIN_h}(g_{o(f\min)})$, was marked as treetops. An h-minima transform can fill up all regional minima the depths of which are less than *h* meters (Figure 1.4(b)). Note that the regional minima of $g_{o(f\min),\,h\min}$ include not only the minima caused by the outliers but also the local minima of terrain (Figure 1.4(c)).

b) Select the regional minima of $\mathrm{EMIN_h}(g_{o(f\min)})$ the area of which are smaller than threshold *a*. Since outliers are scattered, only the regional minima smaller than *a* are classified as outlier areas.

c) Fill the cells of each outlier area using a similar procedure for filling missing data. That is, to find their boundary of each outlier area and fill cells of the area with the minimum elevation of their boundary cells (Figure 1.4(d)). The $g_{o(f\min)}$ with outliers removed and filled is denoted as $\tilde{g}_{o(f\min)}$.

The choices of *h* and *a* are data-dependent and should be set by trial and error. The values of *h* and *a* are 3m and 100m^2 respectively for the dataset tested in this study.

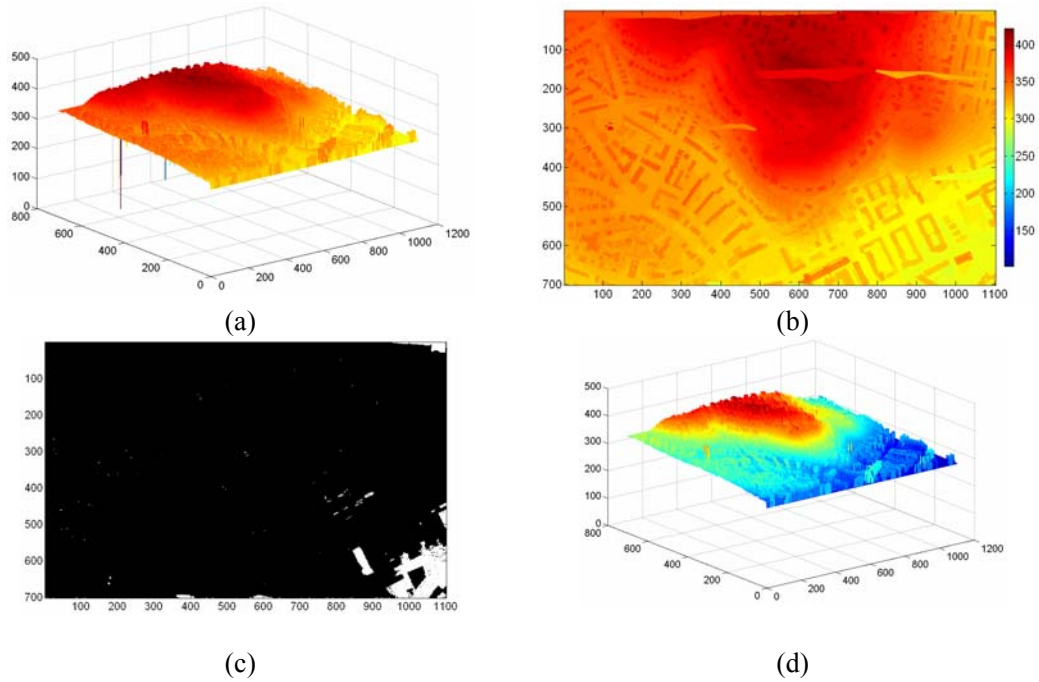

Figure 1.4. Outlier detection and filling. (a) a 3D view of a grid with outliers, (b) the planer view of this grid, (c) the extended-minima transform of (b) where white stands for the area of regional minima, and (d) the grid after outliers filling.

2.5 Filtering over Areas with Buildings

Assume trees have been removed in $\tilde{g}_{o(f\min)}$. However, the window size $d_{\min}$ is usually not large enough to remove large objects such as buildings. Consider the one-dimensional example in Figure 1.1. When the window size is as small as three neighboring points, the building is kept intact although the tree has been removed (Figure 1.1(b)). As mentioned in Section II.A., when the window size increases to seven neighboring points, the building can be removed (see building A in Figure 1.1(c)); however, more protruded terrain will be cut off (see the location C in Figure 1.1(c)). The following way is used to determine whether the cut points are from buildings or terrain:

Suppose there are points that are opened with a small window size called

orginalOpen (Figure 1.1(b)). Now open these points with a larger window size and create new points called *newOpen* (Figure 1.1(c)). The cut points can be easily found by calculating the elevation differences between *newOpen* and *originalOpen*. For simplicity, assume the points with difference greater than zero are cut points (the gray points in Figure 1.1(d)). If considering the neighboring cut points as a group, it can be found that the group from building A has abrupt elevation changes along its edges while the group from terrain C has little changes along its edges. Therefore, if the group of cut points has high elevation difference along its edges, it will be classified as building points; otherwise, it will be classified as terrain points. For the building points, they will be marked and their elevation in *originalOpen* will be updated with the values from *newOpen*; while for the terrain points, the elevation of *originalOpen* will be unchanged (Figure 1.1(e)).

The above procedure will be iteratively performed with progressively increased window sizes until all building points are marked. To find all building areas, the maximum window size should be greater than the size of the largest building, which is denoted as d_{max}. The window size w_i , where $i \in [1,\ldots, n]$, is:

$$w_i = \begin{cases} d_{\min} + 2^i & \text{if } w_i < d_{\max} \\ d_{\max} & \text{if } w_i \le d_{\max} \end{cases} \tag{5}$$

The illustration of the above procedure is somewhat simplified for clarification. The pseudo code of the actual procedure is as follows:

1. *buildingMask* =0 # binary image indicating it is a building or not. 1 for buildings and 0 for else
2. *originalOpen*= $\tilde{g}_{o(f\min)}$

3. for $w_i = w_1$ to w_n

4. *newOpen*=imopen(*originalOpen*, w_i) # open originalOpen with window size w_i

5. *diff=originalOpen-newOpen*

6. create cut areas m_j which satisfy $diff_B$>1m

7. remove m_j that are smaller than $d_{min}*d_{min}$ m^2.

the following loop checks whether each binary area m_j is truly a building area or not.

8. for each m_j

9. get the list of *diff* along boundary of m_j, that is, $\{diff(m_{j,b})\}$

10. if min($\{diff(m_{j,b})\}$)>p_min (condition 1) OR

prctile5($\{diff(m_{j,b})\}$)>p_prctile5 (condition 2) OR

prctile20($\{diff(m_{j,b})\}$)>p_prctile20 (condition 3) OR

(prctile80($\{diff(m_{j,b})\}$)>p_prctile80 AND prctile40($\{diff(m_{j,b})\}$)>p_prctile40) (condition 4), then

11. mark the m_j as a building area

12. end

13. end

14. replace the elevation of *originalOpen* with the value of *newOpen* where those m_j are marked as building areas

15. change the value of *buildingMask* to 1 where those m_j are marked as building areas

16. end

where p_area, p_min, p_prctile5, p_prctile20, p_prctile40, and p_prctile80 are parameters. And prctile5({$diff(m_{j,b})$}), prctile20({$diff(m_{j,b})$}), prctile40({$diff(m_{j,b})$}), and prctile80({$diff(m_{j,b})$}) are 5, 20, 40, 80 percentiles of {$diff(m_{j,b})$}, respectively. In code line 9, the boundary cells of m_j are found by subtracting m_i and the morphologically eroded area.

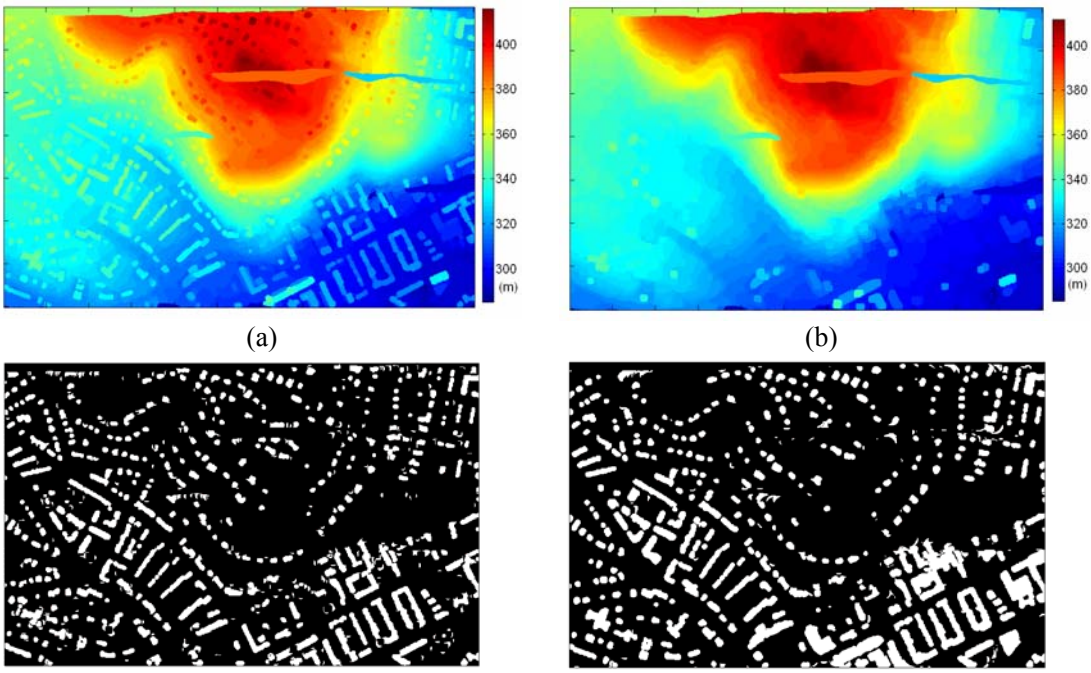

Figure 1.5. (a) *originalOpen*, (b) *newOpen*, (c) binary grid where each area is larger than d_{min}*d_{min} and *diff*>1m, and (d) *buildingMask*.

The above pseudo code is slightly different from the one-dimensional simplified procedure: firstly, note that the points in Figure 1.1 correspond to the cells in a grid and a group of cut points is referred to a cut area here; secondly, based on the fact that buildings are typically higher than 1m, only the areas where the differences between *originalOpen* and *newOpen* are greater than 1m are treated as cut areas (code lines 5 and 6, and see Figures 1.5 (a)-(c)). Such a setting can reduce the chance of

classifying terrain areas as building areas; thirdly, considering the fact that buildings generally occupy relatively large area, only the areas larger than a certain threshold are chosen to save computation (code line 7). This threshold is set to be $d_{min}*d_{min}$ m^2 because smaller buildings have been removed in $\tilde{g}_{o(f\min)}$ (Figure 1.5(c)).

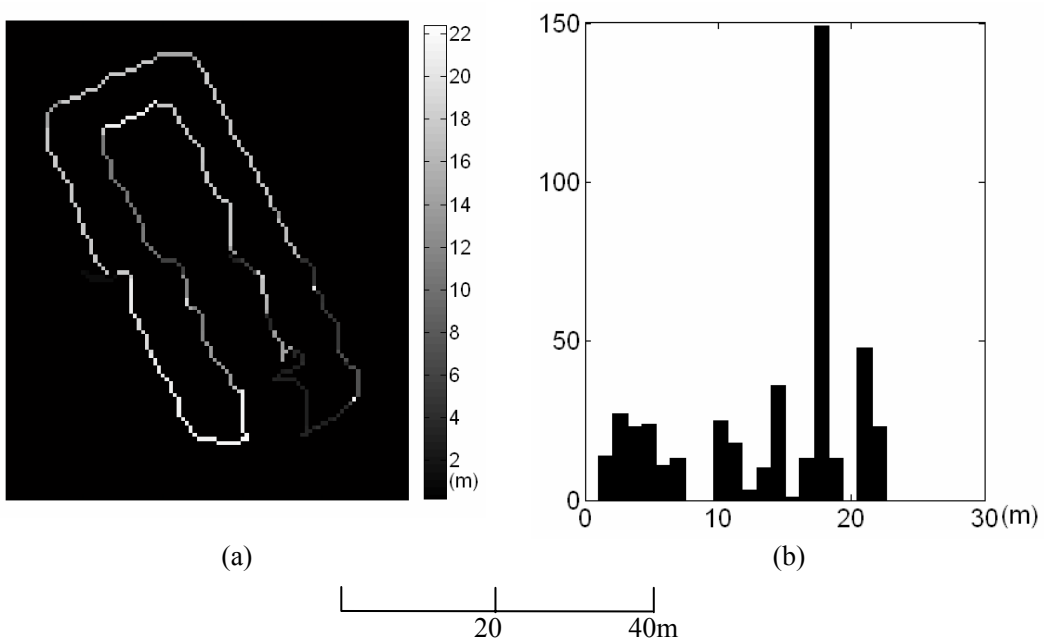

Figure 1.6. (a) $\{diff(m_{X,b})\}$ along the edge of the building X indicated by X in Figure 1.5(d), and (b) the histogram of $\{diff(m_{X,b})\}$

Another difference is that a combination of conditions, rather than one threshold, is used to determine whether each cut area m_j belongs to buildings or not. The reasons for this are illustrated as follows: originally we assumed that a group of cut points (referred to a cut area in a grid) belongs to either buildings or terrain exclusively (Figure 1.1(d)). This assumption is not necessarily true in practice. For example, Figure 1.5(d) indicates the cut area for the building X, the major portion of which covers the building while the rest covers the surrounding terrain. This can be easily observed by examining its values of $\{diff(m_{i,b})\}$ for the boundary cells (Figure 1.6(a)). The low values $\{diff(m_{i,b})\}$ indicates the positions of terrain covered by m_j.

Figure 1.6(b) is the histogram of $\{diff(m_{X,b})\}$, where $diff(m_{X,b})$ is list of elevation differences along the boundary of m_X. In such a situation, it is insufficient to differentiate building and terrain cut areas if only based on min($\{diff(m_{X,b})\}$) or max($\{diff(m_{X,b})\}$). Therefore, the heuristic criteria in code line 10, which characterize the histogram of the $\{diff(m_{X,b})\}$ for a typical building, are used.

There are four conditions for determining whether a cut area m_j is a building or not. In condition 1, the area is classified as a building if all of its boundary cells are p_min meters higher than the terrain. The value of p_min can be determined by common or prior knowledge of building heights in a study site. In this study, it was set to be 2m. As indicated in Figure 1.6(b), there are cases where most of the area's boundary cells are 2m higher than the terrain while some of them are less than 2m above the terrain. For such cases, it is counted as a building area only if 95% of boundary cells are higher than p_prctile5 (condition 2), or 80% of boundary cells are higher than p_prectile20 (condition 3). Condition 4 is to avoid misclassifying some terrain areas as building areas. Finally, a binary mask for buildings *buildingMask* is created (Figure 1.5(d)).

2.5 Terrain Returns Identification

A set of terrain pulses is initially identified by calculating the difference between $g_{\min}$ and $\tilde{g}_{o(f\min)}$, excluding the areas indicated by *buildingMask*. Those cells with absolute value of difference less than 0.5m are treated as terrain. Recall that the X and Y coordinates of the lowest pulse for each cell in $g_{\min}$ have been recorded. The triplex $\{X_i, Y_i, g_{\min,i}\}$ are extracted to generate a DEM by kriging with the ArcGIS 3D Analyst package (ESRI, Redlands, CA). To evaluate the filtering accuracy,

a new set of terrain pulses is obtained by comparing the elevation of last return of each pulse with its DEM value. If the absolute value of difference is less than 0.5m, it is treated as a terrain pulse.

3 Experiment and Results

3.1 Data

Table 1.1 Descriptions for site conditions and relevant LIDAR data

Location	Sites	Special features	Point Spacing	Samples
urban	1	Steep slopes, mixture of vegetation and buildings on hillside, buildings on hillside, data gaps	1-1.5m 2-3.5m 4-6m	Sample 11 Sample 12
	2	Large buildings, irregularly shaped buildings, road with bridge and small tunnel, data gaps	1-1.5m	Sample 21 Sample 22 Sample 23 Sample 24
	3	Densely packed buildings with vegetation between them, building with eccentric roof, open space with mixture of low and high features, data gaps	1-1.5m	Sample 31
	4	Railway station with trains (low density of terrain points), data gaps	1-1.5m	Sample 41 Sample 42
rural	5	Steep slopes with vegetation, quarry, vegetation on river bank, data gaps	2-3.5m	Sample 51 Sample 52 Sample 53 Sample 54
	6	Large buildings, road with embankment, data gaps	2-3.5m	Sample 61
	7	Bridge, underpass, road with embankments, data gaps	2-3.5m	Sample 71

The ISPRS Commission III/WG3 dataset includes four urban sites and four rural sites. Since site 8 does not have reference dataset, it was excluded for analysis. For completeness, Table 5.1 on site information in Sithole and Vosselman (2004) is cited as Table 1.1 here. These sites are located in the Vaihingen/Enz test field and Stuttgart city center, which cover various land use and land cover types including buildings, vegetation, river, roads, railroads, bridges, etc. The laser data were collected with an Optech ALTM scanner, with both first and last pulses recorded. The point spacing is 1-1.5m for urban sites and 2-3.5m for rural sites. Moreover, to test the

effects of point spacing on filtering, site 1 has data with degraded point density. There are a total of 15 reference samples for testing the filtering accuracy. The reference data were generated by manual filtering with knowledge of the landscape and available aerial imagery (Sithole and Vosselman, 2004)

3.2 Parameterization

Table 1.2 summarized the parameters used for sites 1 to 7. The parameters d_{min} and d_{max} can be easily determined by trial and error. Recall that d_{min} is the minimal size of structural elements with which vegetation can be removed by morphological opening and d_{max} is the size of the largest building in the site.

Table 1.2 Parameters used for each site

Parameters	site 1	site 2	site 3	site 4	site 5	site 6	site 7
d_{min}(m)	10	10	10	10	10	4	6
d_{max}(m)	42	60	60	50	30	74	42
p_min(m)	2	2	2	2	2	2	2
p_prctile5(m)	2.5	2.5	2.5	2.5	2.5	2.5	2.5
p_prctile20(m)	3	3	3	3	2.5	3	3
p_prctile40(m)	3.5	3.5	3.5	3.5	3	3.5	3.5
p_prctile80(m)	5	5	5	5	4.5	5	5

For the conditions of differentiating buildings and terrain, their parameters are almost the same for different sites because some characteristics of a building, especially the minimum height, do not vary much even at different places. For example, it is conservative to think that all buildings in an area have a minimum height of 2m. In this study, all sites except site 5 used the same set of parameters for p_min, p_prctile5, p_prctile20, p_prctile40, and p_prctile80, which were 2m, 2.5m, 3m, 3.5m, 5m, respectively. For site 5, the values for p_prctile20, p_prctile40, p_prctile80 were 0.5m smaller than those in other sites because there are some low buildings at this site.

3.3 Results

Fifteen reference samples were used to quantitatively assess the accuracy at all sites. The type I, type II, and total errors were calculated for each sample. Due to the limitation of space, only the accuracy table of sample 11 is shown for illustration purpose (Table 1.3). The type I error is the percentage of bare earth returns misclassified as object returns. The type II error is the percentage of object returns misclassified as bare earth returns. The total error is the error weighted with the portion of each category of reference returns.

Table 1.3 Accuracy assessment table for sample 11

Sample 11		Filtered		Total	Error
		BE	OBJ		
Reference	BE	17607	4179	21786	19.18%
	OBJ	1040	15184	16224	6.85%
	Total	18647	19363	38010	13.92%

The total errors of these fifteen samples for all filtering algorithms reported in Sithole and Vosselman (2004) and our algorithm were summarized in Table 1.4. Our method obtained the lowest total errors for seven samples. The remaining eight samples are close to the lowest errors, except samples 41, 52, 53, and 23. For sample 41, it was found that there are missing data in the north and middle of the area, where is much lower than the terrain after filling. There is also a large group of low outliers and the 100m^2 threshold cannot remove such a large area of outliers. The abrupt elevation changes caused by both outliers and missing data filling lead to that the terrain was treated as buildings. The total errors for samples 52 and 53 are relatively high (greater than 10%). They are both caused by the missing data over the terrain with abrupt changes. The missing data in samples 41, 52, and 53 are all caused by the lack of overlap between swaths. Because the data filling strategy used is to assume that the missing data are caused by water absorption, this problem can be avoided also

by well prepared data collection or changing the ways for filling data. Despite the fact that sample 23 has a total error that is 5.05% higher than the lowest error, the results should not be considered seriously because it is a complicated scene (Figures 1.7(a)-(c)) and it is difficult to define whether some areas belong to bare earth or not (Sithole and Vosselman, 2004).

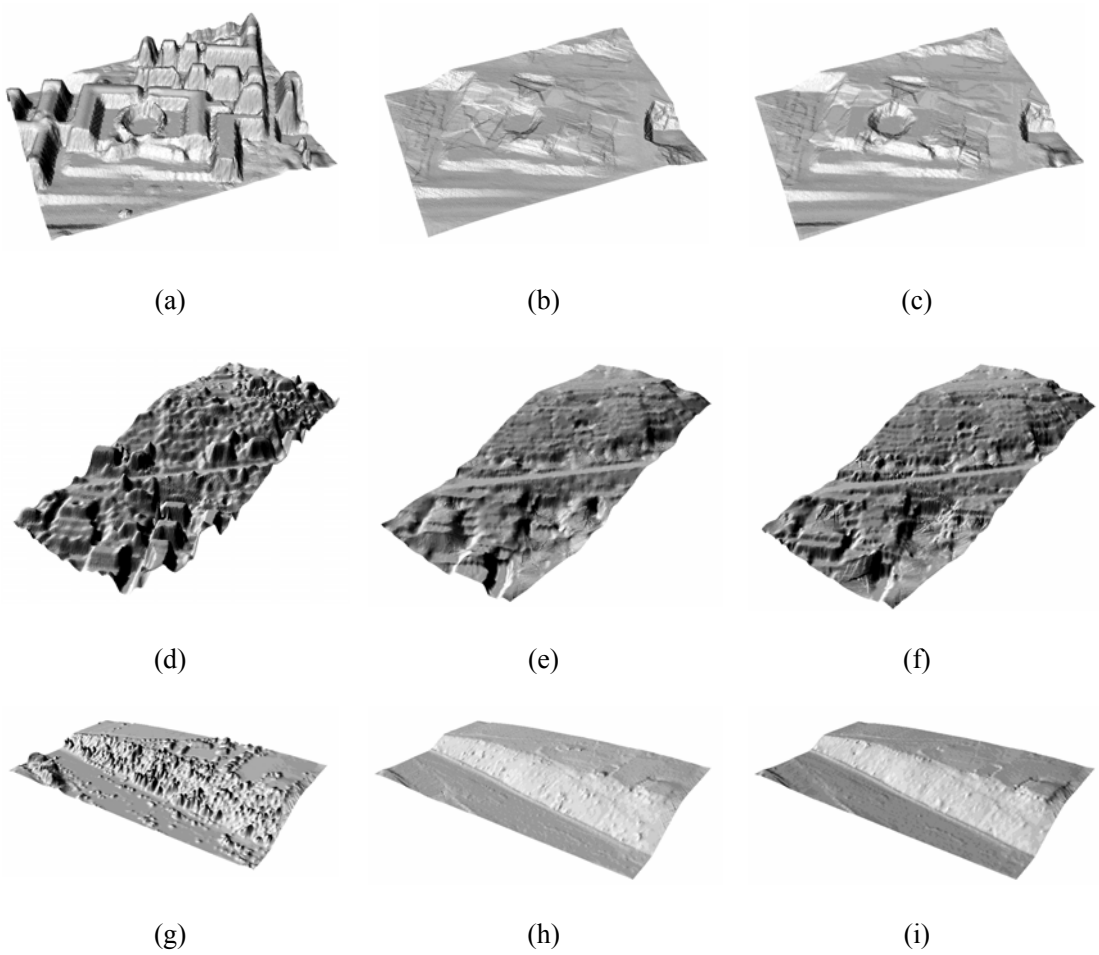

Figure 1.7. (a)-(c), (d)-(f), (g)-(i) are the DSM, filtered DEM, and true DEM for sample 23, sample 11, and sample 51, respectively.

There are steep slopes in samples 11, 51, and 52. If the effects of missing data are disregarded and then sample 52 is excluded for analysis, it seems that this method can work well over both urban area (sample 11, see Figures 1.7(d)-(f)) and forest area (sample 51, see Figures 1.7(g)-(i)) with steep slopes. Another advantage of this

method is its ability to deal with discontinuity because it is an intrinsic property of morphological opening operation. Was building A in Figure 1.1 considered as terrain, opening would not change its shape only if the structural element is smaller than its size.

3.4 Effects of Pulse Density

It is important to test the performance of filtering methods in data with different pulses density because lower pulse density implies smaller costs for acquiring data. Only site 1 was tested since reference data are not available for site 8. The original dataset with point spacing of 1-1.5m was reduced to two new datasets with 2-3.5m and 4-6m point spacing, respectively. The parameters are the same for both original and reduced datasets. Table 1.5 and Figure 1.8 show that our algorithm achieved significantly lower total error than other methods for the reduced dataset, even though Axelsson's method is slightly better than our algorithm in the original dataset. Although the test in one site is not sufficient to make conclusive evaluation, the results show this algorithm has encouraging performance in filtering laser scanner data with low pulse density. Note that the same of parameters are used for different point spacing, indicating that no much trial and error is needed for setting parameters.

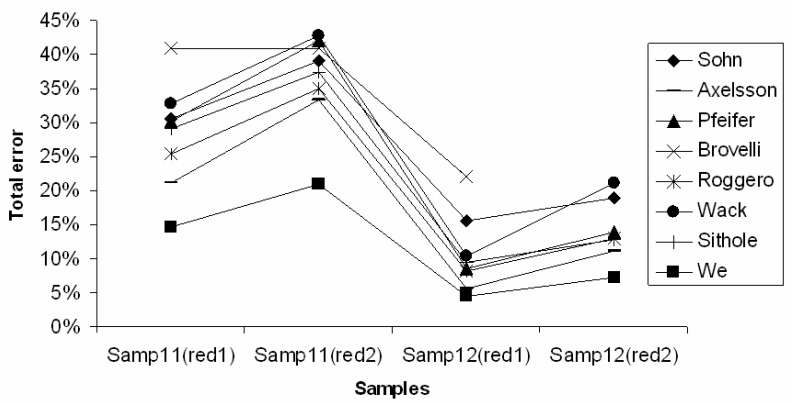

Figure 1.8. Errors of different algorithms for the samples with reduced pulse density.

Table 1.4 Comparison of total errors for all samples

Samples	*Elmqvist (%)*	*Sohn (%)*	*Axelsson (%)*	*Pfeifer (%)*	*Brovelli (%)*	*Roggero (%)*	*Wack (%)*	*Sithole (%)*	*We (%)*	*Mean (%)*	*Min (%)*	*Max (%)*
1(Sample11)	22.40	20.49	10.76	17.35	36.96	20.80	24.02	23.25	13.92	21.11	10.76	36.96
2(Sample 12)	8.18	8.39	3.25	4.50	16.28	6.61	6.61	10.21	3.61	7.52	3.25	16.28
3(Sample 21)	8.53	8.80	4.25	2.57	9.30	9.84	4.55	7.76	2.28	6.43	2.28	9.84
4(Sample 22)	8.93	7.54	3.63	6.71	22.28	23.78	7.51	20.86	3.61	11.65	3.61	23.78
5(Sample 23)	12.28	9.84	4.00	8.22	27.80	23.20	10.97	22.71	9.05	14.23	4.00	27.80
6(Sample 24)	13.83	13.33	4.42	8.64	36.06	23.25	11.53	25.28	3.61	15.55	3.61	36.06
7(Sample 31)	5.34	6.39	4.78	1.80	12.92	2.14	2.21	3.15	1.27	4.44	1.27	12.92
8(Sample 41)	8.76	11.27	13.91	10.75	17.03	12.21	9.01	23.67	34.03	15.63	8.76	34.03
9(Sample 42)	3.68	1.78	1.62	2.64	6.38	4.30	3.54	3.85	2.20	3.33	1.62	6.38
10(Sample 51)	23.31	9.31	2.72	3.71	22.81	3.01	11.45	7.02	2.24	9.51	2.24	23.31
11(Sample 52)	57.95	12.04	3.07	19.64	45.56	9.78	23.83	27.53	11.52	23.44	3.07	57.95
12(Sample 53)	48.45	20.19	8.91	12.60	52.81	17.29	27.24	37.07	13.09	26.41	8.91	52.81
13(Sample 54)	21.26	5.68	3.23	5.47	23.89	4.96	7.63	6.33	2.91	9.04	2.91	23.89
14(Sample 61)	35.87	2.99	2.08	6.91	21.68	18.99	13.47	21.63	2.01	13.96	2.01	35.87
15(Sample 71)	34.22	2.20	1.63	8.85	34.98	5.11	16.97	21.83	3.04	14.31	1.63	34.98%

* The algorithms with the lowest total error are underlined for each sample.

Table 1.5 Comparison of total errors in site 1 with reduced pulse density

Samples	*Sohn (%)*	*Axelsson (%)*	*Pfeifer (%)*	*Brovelli (%)*	*Roggero (%)*	*Wack (%)*	*Sithole (%)*	*We (%)*	*Mean (%)*	*Min (%)*	*Max (%)*
Sample 11(red1)	30.64	21.11	30.13	40.91	25.42	32.72	29.00	14.64	28.07	14.64	40.91
Sample 11(red2)	38.99	33.34	42.01	40.91	35.06	42.82	37.39	20.89	36.43	20.89	42.82
Sample 12(red1)	15.49	5.47	8.46	22.02	8.13	10.35	9.49	4.49	10.49	4.49	22.02
Sample 12(red2)	18.89	11.17	13.90	NA	12.90	21.10	12.84	7.28	14.01	7.28	21.10

* The algorithms with the lowest total error are underlined for each sample

4 Discussion

Although the test results demonstrate the ability of this method, it is worthwhile mentioning that the reference data were available after the test results submission deadline for the previous participants. Unlike in this study, they had no chance to optimize their algorithms for these reference samples. Therefore, it is not 100% fair to compare this method with those participants.

The focus of this study is the filtering of bare earth and objects (especially vegetation and buildings). However, more research is needed to further differentiate attached (bridges, ramps, etc) and detached (buildings, vegetation, etc) objects (Sithole and Vosselman, 2004). Because these two categories of objects have different patterns of elevation changes around their boundaries, it is possible to extend this method for classifying them. One problem of this method is that it will remove the elevation variations smaller than d_{min} in the opened grid, leading to missed terrain points in over-rugged area. If a very fine DEM at the scale smaller than d_{min} is required, new methods are needed for extracting those terrain pulses.

5 Conclusions

In this study, a morphological method for filtering laser scanner data is proposed. Such topics as missing data filling, outlier detection, and filtering in urban and vegetated area are covered. This method was applied into ISPRS Commission III, WG3 dataset and tested over 15 samples at 7 sites. It performed well in many complicated scenes such as areas with discontinuity, large buildings, steep slopes,

bridges, ramps, and vegetation on steep slopes. The almost same set of parameters for differentiating buildings and terrain (p_min, p_prctile5, p_prctile20, p_prctile40, and p_prctile80) can be used for different places. When necessary, they only need slight adjustment. Therefore, basically only two parameters (d_{min} and d_{max}) need to be specified in the algorithm, which can be easily determined by trial and error. The major factor affecting the performance is the discontinuity caused by missing data. This situation can be improved with either the advances in sensor design or overlapping swaths of the data.

References

Axelsson, P. E., 1999. Processing of laser scanner data - algorithms and applications, *ISPRS Journal of Photogrammetry and Remote Sensing*, 54(2-3): 138-147.

Axelsson, P. E., 2000. DEM generation from laser scanner data using adaptive TIN models, *International Archives of Photogrammetry and Remote Sensing,* XXXIII (B4), Amsterdam, The Netherlands, pp.110-117.

Brandtberg, T., T. A. Warner, Landenberger, R. E., and J. B. McGraw, 2003. Detection and analysis of individual leaf-off tree crowns in small footprint, high sampling density lidar data from the eastern deciduous forest in North America, *Remote Sensing of Environment*, 85(3): 290-303.

Flood, M., 2001. LIDAR activities and research priorities in the commericial sector, *International Archives of Photogrammetry and Remote Sensing*, XXXIV(WG IV/3), Annapolis, Maryland, pp. 678-684.

Flood, M. and B. Gutelius, 1997. Commercial implications of topographic terrain

mapping using scanning airborne laser radar, *Photogrammetric Engineering and Remote Sensing*, 63(4): 327-&.

Gong, P., G. Biging, R. Standiford, 2000. The potential of digital surface model for hardwood rangeland monitoring, *Journal of Range Management*, 53:622-626.

Gong, P., Y. Sheng, G.S. Biging, 2002. 3D model-based tree measurement from high resolution aerial imagery, *Photogrammetric Engineering and Remote Sensing*, 68(11): 1203-1212.

Haugerud R.A., Harding D.J., 2001. Some algorithms for virtual deforestation (VDF) of LIDAR topographic survey data, *International Archives of Photogrammetry and Remote Sensing*, XXXIV(WG IV/3), Annapolis, Maryland, pp. 211-218.

Hoekman, D.H., and C. Varekamp, 1998, High resolution single-pass interferometric radar observation of tropical rain forests trees, in *Proceedings of the Second International Workshop on Retrieval of Bio & Geo-Physical Parameters from SAR data for Land Applications,* 21-23 October, Noordwijk, The Netherlands, European Space Agency, SP 441, pp. 233-240.

Huising E.J and Gomes Pereira L. M., 1998. Errors and accuracy estimates of laser altimetry data acquired by various laser scanning systems for topographic applications, *ISPRS Journal of Photogrammetry and Remote Sensing*, 53(5): 245-261.

Kilian, J., N. Haala, and M. Englich, 1996. Capture and evaluation of airborne laser scanner data, *International Archives of Photogrammetry and Remote Sensing*, XXXI (B3), Vienna, Austria, pp.385-388.

Kraus, K. and N. Pfeifer, 1998. Determination of terrain models in wooded areas

with airborne laser scanner data. *ISPRS Journal of Photogrammetry and Remote Sensing*, 53(4): 193-203.

Lee, H. S. and N. H. Younan, 2003. DTM extraction of lidar returns via adaptive processing, *IEEE Transactions on Geoscience and Remote Sensing*, 41(9): 2063-2069.

Sheng, Y., P. Gong, G.S. Biging, 2001. Model-based conifer crown surface reconstruction from high-resolution aerial images, *Photogrammetric Engineering and Remote Sensing,* 67(8): 957-965.

Sithole, G. and G. Vosselman, 2004. Experimental Comparison of Filter Algorithms for Bare Earth Extraction From Airborne Laser Scanning Point Clouds, *ISPRS Journal of Photogrammetry and Remote Sensing*, 59 (1-2): 85-101.

Soille, P., 2003. *Morphological Image Analysis: Principles and Applications*, 2nd ed., Springer-Verlag, NY, 391p.

Vosselman G., 2000. Slope based filtering of laser altimetry data, *International Archives of Photogrammetry and Remote Sensing*, XXXIII (B3), Amsterdam, The Netherlands. pp. 935-942.

Zhang, K. Q., S. C. Chen, Whitman, D., Shyu, M. L., Yan, J. H., and C. C. Zhang, 2003. A progressive morphological filter for removing nonground measurements from airborne LIDAR data, *IEEE Transactions on Geoscience and Remote Sensing*, 41(4): 872-882.

Chapter 2 Isolating Individual Trees in a Savanna Woodland Using Small Footprint LIDAR Data

Abstract

This study presents a new method of detecting individual treetops from LIDAR (Light Detection and Ranging) data and applies marker-controlled watershed segmentation into isolating individual trees in savanna woodland. The treetops were detected by searching local maxima in a canopy maxima model (CMM) with variable window sizes. Different from previous methods, the variable windows sizes were determined by the lower-limit of the prediction intervals of the regression curve between crown size and tree height. The canopy maxima model was created to reduce the commission errors of treetop detection. Treetops were also detected based on the fact that they are typically located around the center of crowns. The tree delineation accuracy was evaluated by a five-fold cross-validation method. Results showed that the absolute accuracy of tree isolation was 64.1%, which was much higher than the accuracy of the method which only searched local maxima within window sizes determined by the regression curve (37.0%).

1 Introduction

Isolating individual trees and extracting relevant tree structure information from remotely sensed data have significant implications in a variety of applications. For example, detailed information at the individual-tree level can be used for monitoring forest regeneration (Gougeon and Leckie, 1999; Clark *et al*., 2004a and

2004b), reducing field work required for forest inventory (Gong *et al*., 1999) and assessing forest damage (Leckie *et al*., 1992; Levesque and King, 1999; Kelly *et al*., 2004). To study the interactions between vegetation and climate, we are applying an individual-tree based model, called MAESTRA, over an eddy covariance tower site in Ione, California for quantifying the carbon fluxes. To parameterize the individual-tree based model, our research is ongoing to extract individual-tree structure parameters such as tree height, crown height, crown size, leaf area index (LAI), and biomass using small-footprint LIDAR data over an area of 800m by 800m around the eddy covariance tower. However, to obtain such individual tree parameters, the initial process is to isolate individual trees and delineate tree crown boundaries.

Intensive research has been done on isolating individual trees using remotely-sensed data. However, previous data focus on large-scale aerial photos or high-spatial resolution remotely sensed imagery. The methods for isolating individual trees from imagery or photos include: local maxima detection (Dralle and Rudemo, 1996), local maxima filtering with fixed or variable window sizes (Wulder *et al*., 2000; Pouliot *et al*., 2002), valley-following (Gougeon, 1995), edge detection using scale-space theory (Brandtberg and Walter, 1998), template-matching (Pollock, 1996; Larsen and Rudemo, 1998), local transect analysis (Pouliot *et al*., 2002), 3-D modeling (Sheng *et al*., 2001; Gong *et al*., 2002), and watershed segmentation (Schardt *et al*., 2002; Wang *et al*., 2004). When isolating trees from a monocular image or photo, these methods are mostly based on the assumption that there are

“peaks” of reflectance around the treetops and “valleys” along the canopy edges. However, the “peaks” and “valleys” are not always distinct since canopy reflectance is affected by various factors such as illumination conditions, canopy spectral properties and complex canopy structure.

Recently, researchers have begun to apply LIDAR data into individual tree isolation and canopy information extraction (Hyyppä *et al*., 2001; Persson *et al*., 2002; Brandtberg *et al*., 2003; Leckie *et al*., 2003; Popescu *et al*., 2003; Popescu and Wynne, 2004). Compared with passive imaging, LIDAR has the advantage of directly measuring the three dimensional coordinates of canopies. Therefore, the geometric, rather than spectral, “peaks” and “valleys” can be detected. Several studies have extended methods developed for optical imagery and aerial photos into LIDAR data for tree detection (Brandtberg *et al*., 2003; Leckie *et al*., 2003; Popescu *et al*., 2003). Brandtberg *et al*. (2003) extended the scale-space theory to detecting crown segments. Leckie *et al*. (2003) applied the valley-following approach into both LIDAR and multi-spectral imagery and found that the LIDAR can easily eliminate most of the commission errors that occur in the open stands while the optical imagery performs better for isolating trees in Douglas-fir plots.

This study attempts to use marker-controlled watershed segmentation in tree isolation. Watershed segmentation, first proposed by Beucher and Lantuejoul (1979), is a well-known image segmentation method that incorporates the advantages of other segmentation methods such as region-growing and edge-detection (Soille 2003). To avoid the over-segmentation problem, Meyer and Beucher (1990)

introduced marker-controlled watershed segmentation. The idea is to perform watershed segmentation around user-specified markers rather than the local maxima in the input image. The image indicating the locations of markers is called a *marker function* and the image for producing watersheds is called a *segmentation function*. Marker-controlled watershed segmentation is well suited for tree isolation. With appropriate marker and segmentation functions, marker-controlled watershed segmentation can be used to delineate the boundaries of individual crowns. This characteristic makes it superior to local transect or profile methods (Pouliot *et al*., 2002; Popescu *et al*., 2003), which can only obtain crown radii for limited directions.

Marker-controlled watershed segmentation was applied for tree isolation in a CASI (Compact Airborne Spectrographic Imager) image (Wang *et al*., 2004). Schardt *et al*. (2002) used the threshold for isolating spruce trees in LIDAR data and suspected it to be unsuitable for deciduous tree species due to their complex canopy structure. In marker-controlled watershed segmentation, the forms of marker and segmentation functions play a key role in partitioning an image to meaningful objects. In particular, marker functions corresponding to treetops are crucial for its successful application in tree isolation. This study hypothesizes that individual trees can be isolated for deciduous trees only if appropriate marker and segmentation functions are generated from LIDAR data. Based on these, the objectives of this study are to present methods for generating treetop marker and segmentation functions from LIDAR data and test their application into tree isolation in savanna woodland

This paper is organized as follows: in section II, the methods of treetop detection with variable window sizes are discussed and a new method of creating marker and segmentation functions is introduced; in section III, the performance of these markers and segmentation functions is evaluated and relevant errors are analyzed; and section IV concludes the paper.

2 Methods

2.1 Study Area and LIDAR data

The study site is an open oak savanna woodland, located near Ione, California (latitude: 38.26'N, longitude: 120.57'W) (Figure 2.1).

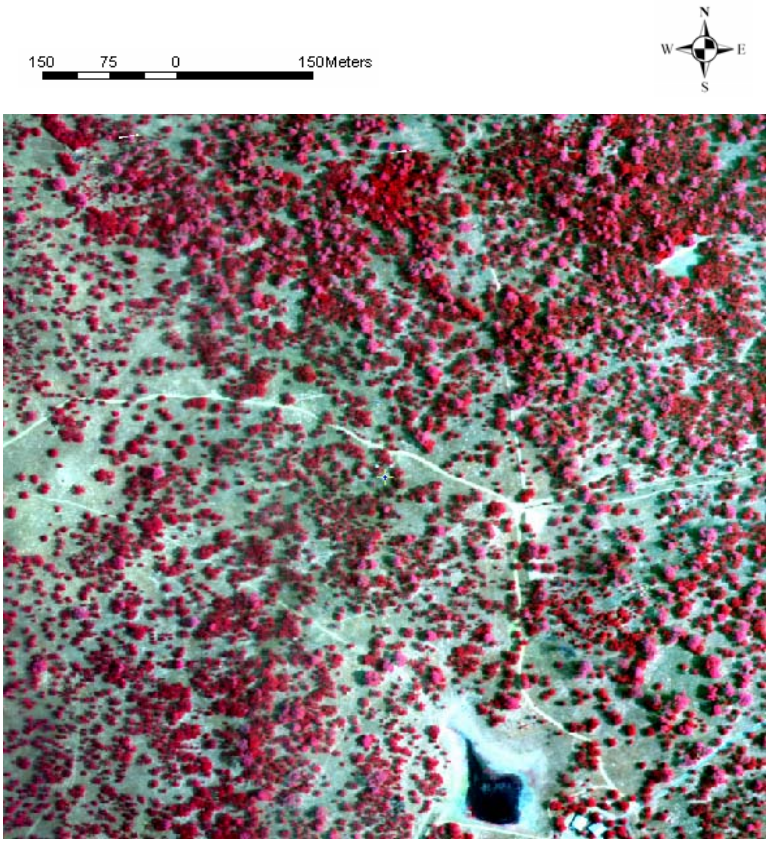

Figure 2.1. A CASI image covering the study area.

The site is on a private ranch and is part of the AmeriFlux network of eddy covariance field sites (Baldocchi *et al*., 2004). The landscape is characterized by flat

terrain (with a maximum slope of less than 15%) with a scattered, clumped distribution of blue oaks (*Quercus douglasii H.&A.*) and a minority of grey pines over a continuous layer of Mediterranean annual grasses. On August 24, 2003, laser altimetry data were acquired with Optech ALTM 2025, which recorded both first and last returns for each laser pulse. The scanning pattern was z-shape. The claimed vertical accuracy from the data provider is 18 cm with 95% confidence and the horizontal accuracy is 1/3000 of the flying height (WHO IS PROVIDER?). The swath is ca. 300m and the flying altitude is ca. 500m. The footprint size is about 18 cm. The average posting density is 9.5 points per square meter, resulting in an average spot spacing of about 32 cm. To obtain such a high pulse density, the site was flown twice. The data covering 800 by 800 m^2 around the eddy covariance tower was used in this study to isolate individual trees.

2.2 Digital Elevation Model

The tree isolation from LIDAR data is typically based on a canopy height model (CHM), which is the difference between canopy surface height and a digital elevation model (DEM) of the earth surface. The research on generating a DEM from laser altimetry data, also called *filtering*, is still in its infancy. Typically, the laser pulses are classified iteratively into terrain and non-terrain returns, and the extracted terrain pulses are used to generate a DEM by interpolation (Hyyppä *et al*., 2001; Persson *et al*., 2002; Brandtberg *et al*., 2003). In this study, the basic procedure of generating a DEM is as follows:

First, a grid with cell size of 1m by 1m was created. Each cell recorded the

lowest last return of all pulses falling in the cell. This grid is denoted as $g_{\min}$. If some cells have no pulses within them, they were filled with the nearest cell value. This filled grid is denoted as $g_{f\min}$. Then, a surface approximating the terrain, denoted as $g_{o(f\min)}$, was created by morphologically opening the filled grid $g_{f\min}$. An initial set of terrain pulses were identified by calculating the difference between $g_{\min}$ and $g_{f\min}$. The cells with absolute value of difference less than 0.5m were treated as cells where terrain pulses are located. The triplex $\{X_i, Y_i, g_{\min,i}\}$ from these cells were used to create a DEM by kriging. A new set of terrain pulses were obtained by comparing the elevation of last return of each pulse with its DEM value. If their absolute value of difference was less than 0.5m, it was classified as a terrain pulse. The details on the algorithm are presented in another companion paper (Chen *et al*., 2004). Figure 2.2 shows the DEM.

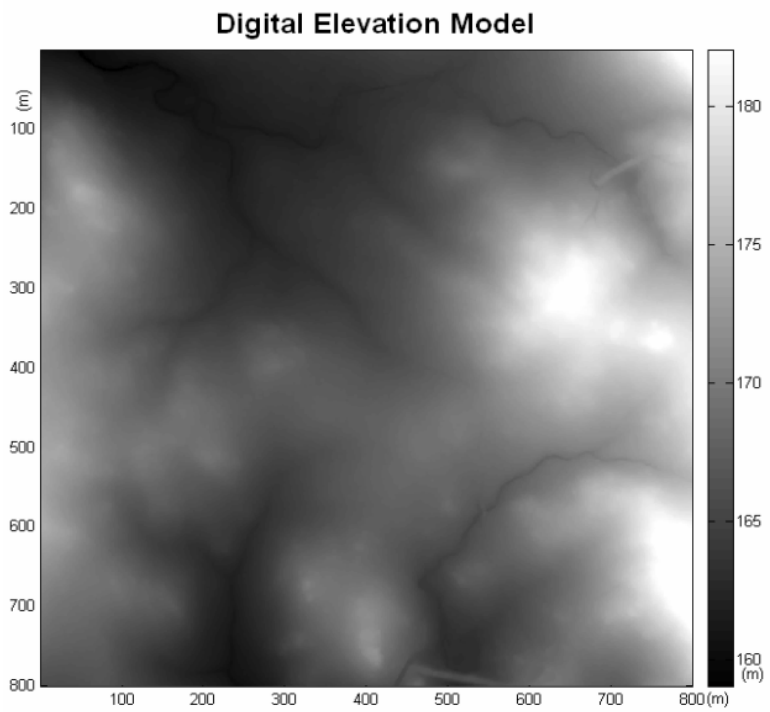

Figure 2.2. The DEM generated from LIDAR data.

To assess the accuracy of filtering, three plots, each with an area of 100m by 100m, were randomly located and the pulses were manually classified into terrain and vegetation returns, and this layer acted as subsequent ground truth. The accuracy of filtering was evaluated by calculating the type I, type II and total error (Sithole and Vosselman, 2003). Type I error is the percentage of terrain returns misclassified as vegetation returns. Type II error is the percentage of vegetation returns misclassified as terrain returns. Total error is the error weighted with the portion of each category of reference returns. The accuracy is summarized in Table 1. The high accuracy of filtering is partially due to the flat terrain over the study area.

Table 2.1. Filtering Accuracy assessment table for all plots

All plots		Filtered		Total	Error
		Terrain	Vegetation		(%)
Reference	Terrain	218189	2305	220494	1.04
	Vegetation	1650	92479	94129	1.75
Total		18647	19363	314623	1.26

2.3 Canopy Height Model

After the DEM has been created, the relative canopy height of laser pulses can be calculated and interpolated into a CHM. Previous research used kriging (Popescu and Waynne 2004), active contour algorithm (Persson *et al*., 2002), or VDEMINT program in PCI EASI (Leckie *et al*., 2003) to create a CHM or digital surface model (DSM). In Popescu and Waynne (2004), at first a grid was created, each cell of which recorded the elevation of the highest first-return of laser pulses within it; then, the elevations within these cells were interpolated into a CHM by kriging. This method is used in this study. The cell size of the grid is an important

parameter in constructing a CHM. A large cell size will reduce the variations of canopy height and make the "peaks" and "valleys" difficult to detect in the interpolated CHM. Nevertheless, a very small cell size could dramatically increase the data storage. If first-return density λ (returns/mP^{2P}) does notchange over the study area, the average distance between pulses is:

$$d = \sqrt{\frac{1}{\lambda}} \tag{1}$$

and cell size can be set to *d*. In practice, pulse density varies because there are side overlaps between swaths and pulse density is higher along the edges of a swath for this dataset. Therefore, a small cell size should be used when there are large pulse densities locally. The variations of λ were investigated by overlaying a grid of 1m by 1m cells over the first-returns. Results showed that λ varied from 0 to 115 returns per m^2. A large λ was chosen by calculating the *p*-th quantile of λ. In this study, *p* was set to be 0.99 and its corresponding λ value was 44. With equation (1), the cell size was set to be 0.2m.

2.4 Variable Window Sizes in Treetops Detection

Treetops can be detected by finding the local maxima (Hyyppä *et al*., 2001; Persson *et al*., 2002) or local maxima within fixed or variable window sizes in a CHM (Dralle and Rudemo, 1996; Wulder *et al*., 2000). The main problem encountered when using local maxima to detect treetops is large commission errors, that is, non-treetop local maxima are incorrectly classified as treetops. Wulder *et al*. (2000) detected treetops from high spatial resolution optical imagery by searching local maxima within variable window sizes. The window sizes were adaptively

calculated based on the semivariance range or local breaks in slope. Popescu and Waynne (2004) derived variable window sizes by assuming a relationship between tree height and crown size and used them to detect treetops from LIDAR data. Popescu and Waynne (2004)'s method was tested in this dataset.

To obtain a relationship between tree height and crown size, tree height and crown size were measured manually from the CHM. Tree height is the maximum height within a manually determined crown. Crown size is the average crown diameter along two perpendicular directions. The trees were sampled systematically over the whole study area with horizontal and vertical intervals of 53m. If there were no trees in the sampling locations, the nearest tree was selected. The final sample size was 196 trees.

There are several reasons for measuring tree height and crown sizes from the CHM rather than in the field. First, due to high pulse density of this LIDAR dataset, it is easy to identify individual trees from the CHM manually. Second, sampling in a CHM can greatly reduce the workload and is not limited by factors such as accessibility in the field. To evaluate the accuracy, another 26 trees were randomly chosen and their tree height and crown size of measured from both CHM and the field. In the field, the height of each tree was measured with a hypsometer for eight times and the measurements were averaged. Crown size was measured along two perpendicular directions and the average value was used. The mean absolute differences of tree height and crown size between CHM and field measurements were 0.37m and 0.58m, respectively. This indicates that the accuracy is acceptable

when sampling trees from CHM.

It was found that crown size has larger variability when a tree is higher (Figure 2.3), which will violate the assumption of homoscadasticity if a linear model is fitted. To avoid this issue, a nonlinear power model was fitted:

$$\text{Crown size} = 1.7425 \times (\text{Tree height})^{0.5566}. \quad (2)$$

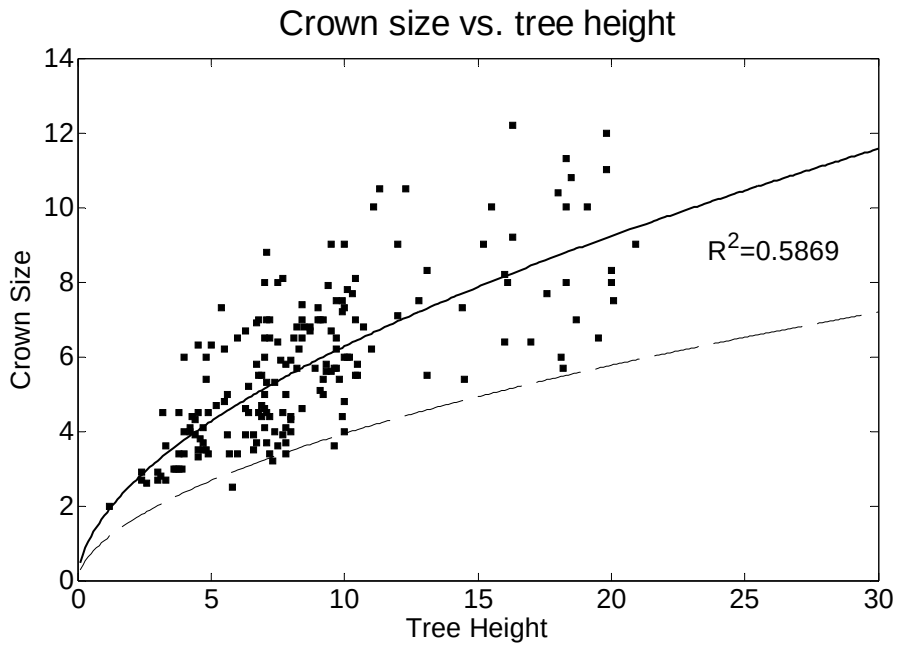

Figure 2.3. The relationship between crown size and tree height. The solid line is the regressive curve and the dashed line is the lower limit of the prediction intervals.

2.5 Variable Window Sizes from Prediction Interval

Using equation (2), the commission errors can be reduced since it will search local maxima within larger window sizes for higher trees. However, this will also lead to large omission errors. Statistically, a half number of the trees at a certain height have smaller crown sizes than the fitted value at this height (Figure 2.3). The treetops of these trees will possibly be missed if the window size is equal to the fitted value. In this study, the window sizes were determined by another curve which is the

1-α lower limit of one-sided prediction interval of the regression model (Figure 2.3). Consider a regression model $Y_x=\beta^T x+\varepsilon_i$. The curve is determined by:

$$\tilde{Y}_x=\hat{Y}-t(1-\alpha;n-2)\sqrt{s^2+xSx'} \quad (3)$$

where $\tilde{Y}_x$ is the lower prediction limit at a given tree height x, s^2 is the mean squared error, t is the inverse of Student's t cumulative distribution function, S is the covariance matrix of the coefficient estimates, $(X^TX)^{-1}s^2$, and $\hat{Y}$ is the fitted value at x. When α is 0.5, the lower limit $\tilde{Y}_x$ is exactly located at the fitted regression curve. When using this curve to determine window sizes for detecting treetops, the omission errors can be reduced by using a small α. However, a smaller α will lead to larger commission errors (see Figures 2.4(b) and (c)). Only if the window size is smaller than the crown size of a tree, there is a risk of including irrelevant local maxima as treetops.

2.6 Canopy Maxima Model

The previous analysis demonstrated that commission and omission errors of treetop detection cannot be decreased simultaneously by adjusting α when a canopy height model was used. This problem can be greatly alleviated when detecting treetops from a canopy maxima model (CMM), which is a regular grid with each cell recording the maximum laser height within its neighborhood. Compared with a CHM, many irrelevant local maxima can be removed in the CMM (Figure 2.4(d)). As detecting treetop markers, variable window sizes are used to creating a CMM. To prevent the “valleys” among crowns from being filled, the window size need to be smaller than the crown size of the smallest tree at a given height. This can be approximated statistically by obtaining the lower limit of one-sided prediction interval with a very small α in

equation (3). Previous researchers have reported that the tree density for blue oaks on gentle slopes has a maximum tree density of about 200 trees/ha (Kiang, 2002). Corresponding to such a number there is a maximum of about 12,800 trees for the study area of 800 by 800m. Based on this, α is set to be 0.0001. The tree height from the CHM was used to determine the window sizes with equation (3).

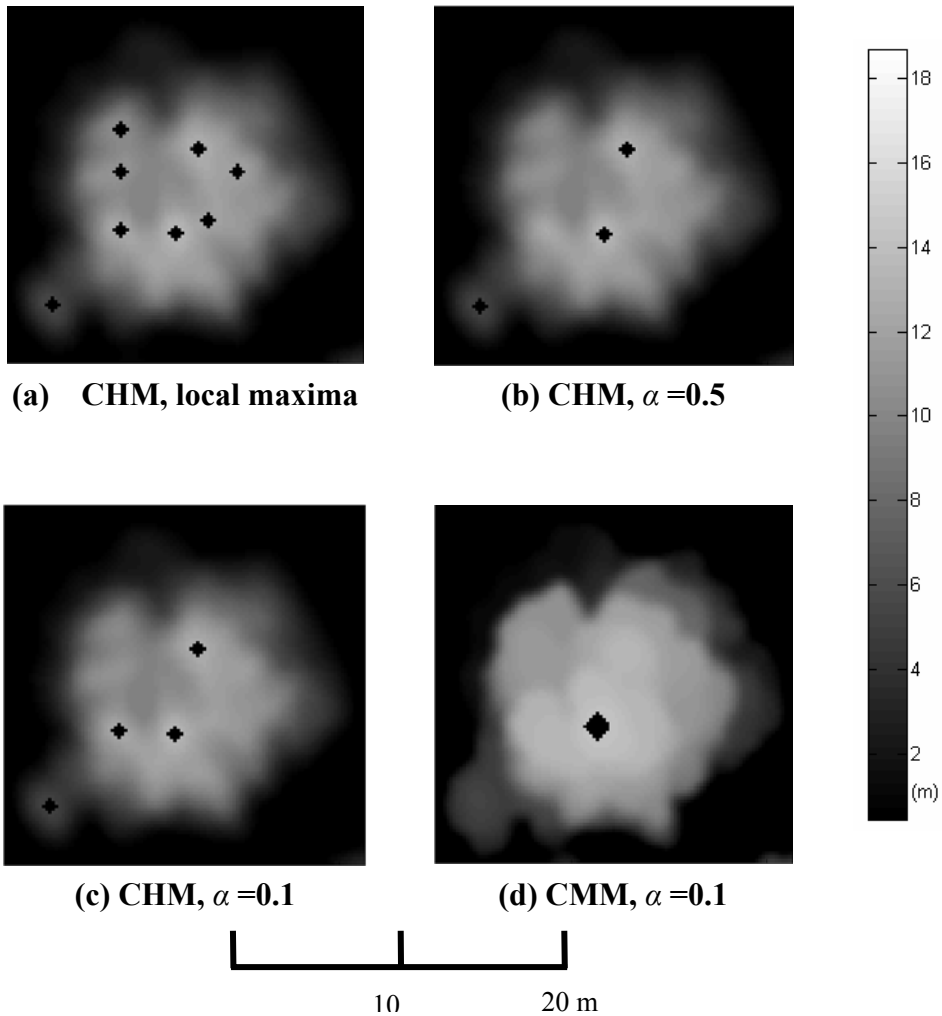

Figure 2.4. Treetops detected using different methods and parameters. (a) Treetops detected from a CHM by searching local regional maxima, (b) treetops detected from a CHM using variable window size when α =0.5, (c) treetops detected from a CHM using variable window sizes when α =0.1, and (d) treetops detected from a CMM using variable window size when α =0.1.

2.7 Gaussian Filtering

In the CMM, not all of the non-treetop local maxima could be removed since the neighborhood window size used for creating the CMM is usually smaller than the crown size, especially for trees which have large crowns at a certain height. Gaussian filtering is a typical procedure for suppressing irrelevant local maxima in treetop detection (Dralle and Rudemo, 1996; Hyyppä *et al*., 2001; Persson *et al*., 2002; Pouliot *et al*., 2002; Schardt *et al*., 2002; Wang *et al*., 2004). Dralle and Rudemo (1996) found that the standard deviation σ of a Gaussian filter is not very important. This conclusion was confirmed in this study and the value of σ was set to be 2. However, the filter size has a significant impact on the smoothed CMM. This study used the criteria that the filter size should not be larger than the crown size of the smallest (in terms of crown) tree over the study area. The determination of the smallest crown size was based on the crown sizes of the sampled trees from the CHM. The smallest crown size can be approximated from the sample by calculating the lower limit of the one-sided prediction intervals for *k* future observations at confidence level (1-α) (Hahn and Meeker, 1991):

$$\text{Lower Limit} = \bar{X} - t_{1-\frac{\alpha}{k}}(n-1)s\sqrt{1+\frac{1}{n}}, \qquad (4)$$

where $\bar{X}$, s, n are the mean, standard deviation, and size of the sample of crown size, respectively (Table 2.2). α was set to be 0.05. Based on the previous analysis, k was set to be 12,800.

When checking the crown size distribution of the sample, it was found that the distribution was skewed to the right. A Jarque-Bera test for the goodness-of-fit of

normal distribution indicated that the p-value was 0.0016, which was significantly different from a normal distribution at 5% level. When transformed into logarithm scale (with natural base *e*), the p-value was 0.2224. Therefore, equation (4) was used to get the lower limit of the one-sided prediction interval of crown sizes at the logarithmic scale. After transformed back to the original scale, a value of 1.0m was obtained for the minimal crown size, which was used as the Gaussian filter size.

Table 2.2. Descriptive statistics of sampled trees (n=196)

Variables	Min(m)	Max(m)	Mean(m)	Std.(m)
Tree height	2.0	12.2	5.8	2.1
Crown size	1.2	20.9	8.8	4.4

In a smoothed CMM, the spurious local maxima other than treetops were greatly reduceed (see Figures 2.4(c) and (d)) and the change of α in equation (4) would affect mostly the omission errors not the commission errors. Applying such a "divide-and-conquer" strategy, both the omission and commission errors for treetop detection can be reduced. After treetops had been detected, they were used for segmenting individual crowns.

2.8 Segmentation with CMM

The process of watershed segmentation can be illustrated in terms of flooding simulations (Soille 2003). Figure 2.5(a) shows a CMM. To simulate the process of flooding, we first calculated the complement of the CMM (Figure 2.5(b)), which resembles two catchment basins. Assume that each basin has a hole punched at its minimum. Then, when immersing it gradually into water, the catchment basins will be flooded. This algorithm can be thought to automatically build dams along the divide line to prevent water in two neighboring catchment basins from merging

(Figure 2.5(c)). The constructed dams are called watershed lines and will be used to partition trees.

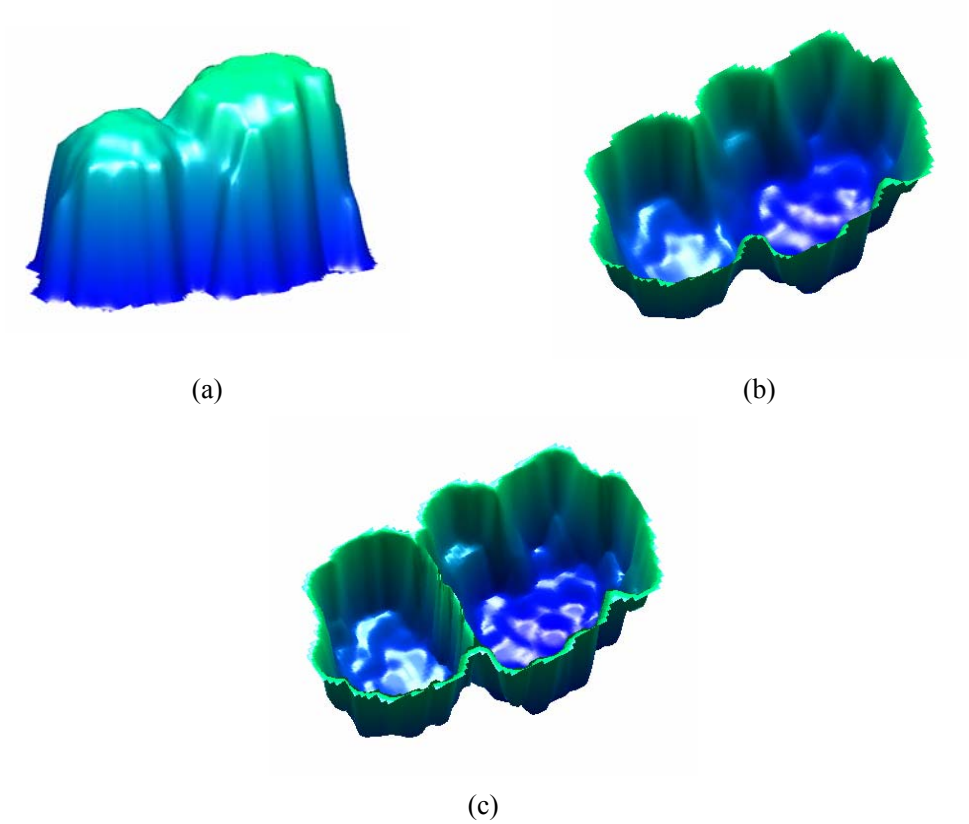

Figure 2.5. An illustration of watershed segmentation Algorithm. (a) A CMM, (b) the complement of the CMM, and (c) dams built at the divide line.

In marker-controlled watershed segmentation, the complement of the CMM is filtered by *minima imposition* before computing its watersheds so that all non-treetop minima have been removed. Suppose there is an image f, which is the complement of the CMM in this case, and a marker image f_m has been specified at each pixel p:

$$f_m(p) = \begin{cases} 0, & \text{if } p \text{ belong to a marker,} \\ \mathrm{t}_{\max} + 1, & \text{otherwise.} \end{cases} \tag{5}$$

where $\mathrm{t}_{\max}$ is the maximum value of the input image f. Minima imposition is to first calculate a pixel-wise minimum between $f+1$ and the marker image f_m,

denoted as $(f+1) \wedge f_m$, and then perform a morphological reconstruction by erosion of $(f+1) \wedge f_m$ from the marker image f_m:

$$f_{mp} = R^{\varepsilon}_{(f+1)\wedge f_m}(f_m), \tag{6}$$

where f_{mp} is the image after minima imposition, $R^{\varepsilon}_{(f+1)\wedge f_m}(f_m)$ is defined as the geodesic erosion of $(f+1) \wedge f_m$ with respect to f_m iterated until stability is reached (Soille, 2003). The geodesic erosion of $(f+1) \wedge f_m$ with respect to f_m is to perform morphological erosion for f_m, but the value of $(f+1) \wedge f_m$ is used only if the value after erosion is smaller than $(f+1) \wedge f_m$. Minima imposition can reconstruct the complement of CMM so that there are only minima corresponding to marked treetops. This illustration highlights the importance of finding a correct treetop marker function when applying marker-controlled watershed segmentation method.

2.9 Segmentation with Distance-Transformed Image

Deciduous trees such as oak have a relatively flat canopy surface, making treetops difficult to detect from the CMM or CHM (Figure 2.6(a)). Since treetops are typically located around the center of crowns, this fact can be exploited to further detect treetops. To implement that, at first, a binary image was created, where the canopy had values of ones while watershed lines and the background had values of zeros (Figure 2.6(b)). Then, a distance transform was performed on the binary image to calculate the distance from each nonzero pixel to its nearest zero pixel (Figure 2.6(c)). In the distance-transformed image, the center of a crown had large values. Like the CMM, the complement of this distance-transformed image, denoted as

$DIST_c$, can be used for segmentation. Treetops were detected from $DIST_c$ using h-minima transformation, which suppressed all minima shallower than *h*. The h-minima transformation of the $DIST_c$ is to perform the reconstruction by erosion of $DIST_c$ from $DIST_c+h$.

$$DIST_{c,\,h\min} = \mathrm{R}^{\varepsilon}_{DIST_c}(DIST_c + h) \tag{7}$$

where $DIST_{c,\,h\min}$ is the h-minima transformation of $DIST_c$. The regional minima of $DIST_{c,\,h\min}$ was marked as treetops. With these treetop markers and the segmentation function $DIST_c$, marker-controlled watershed segmentation were used for delineating tree crown segments (Figure 2.6(d)). Note that the threshold *h* directly affects the performance of detecting treetops. An optimal value of *h* was obtained from the training data.

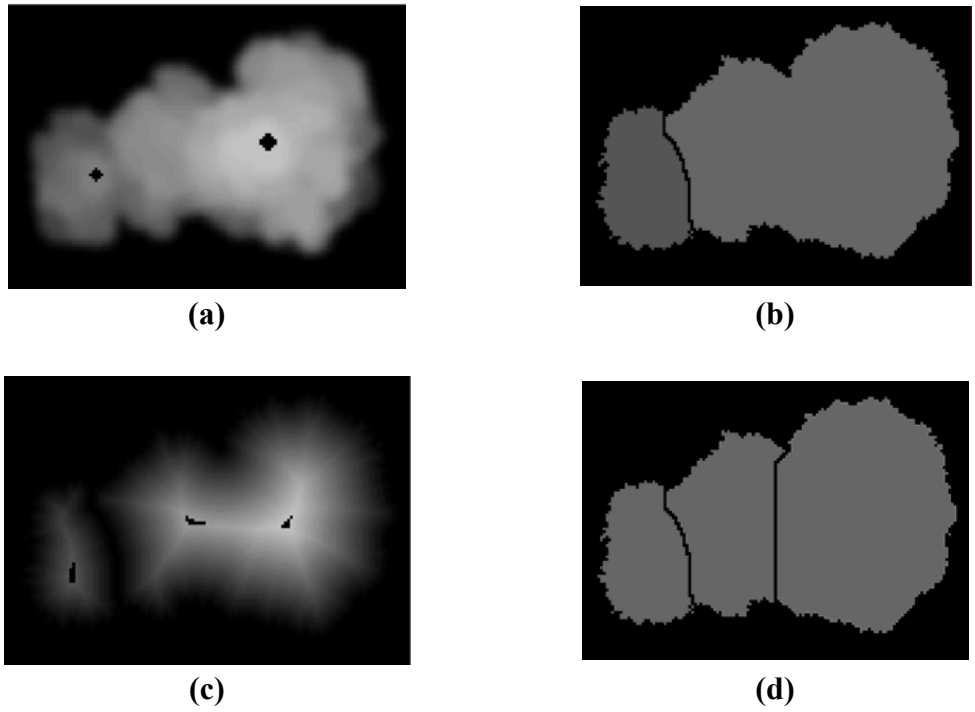

Figure 2.6. Distance-transformed image for treetops detection. (a) Treetops found in CMM, (b) segmentation results using treetops in CMM, (c) distance-transformed

image and treetops detected using h-minima transform, and (d) segmentation results based on distance-transformed image.

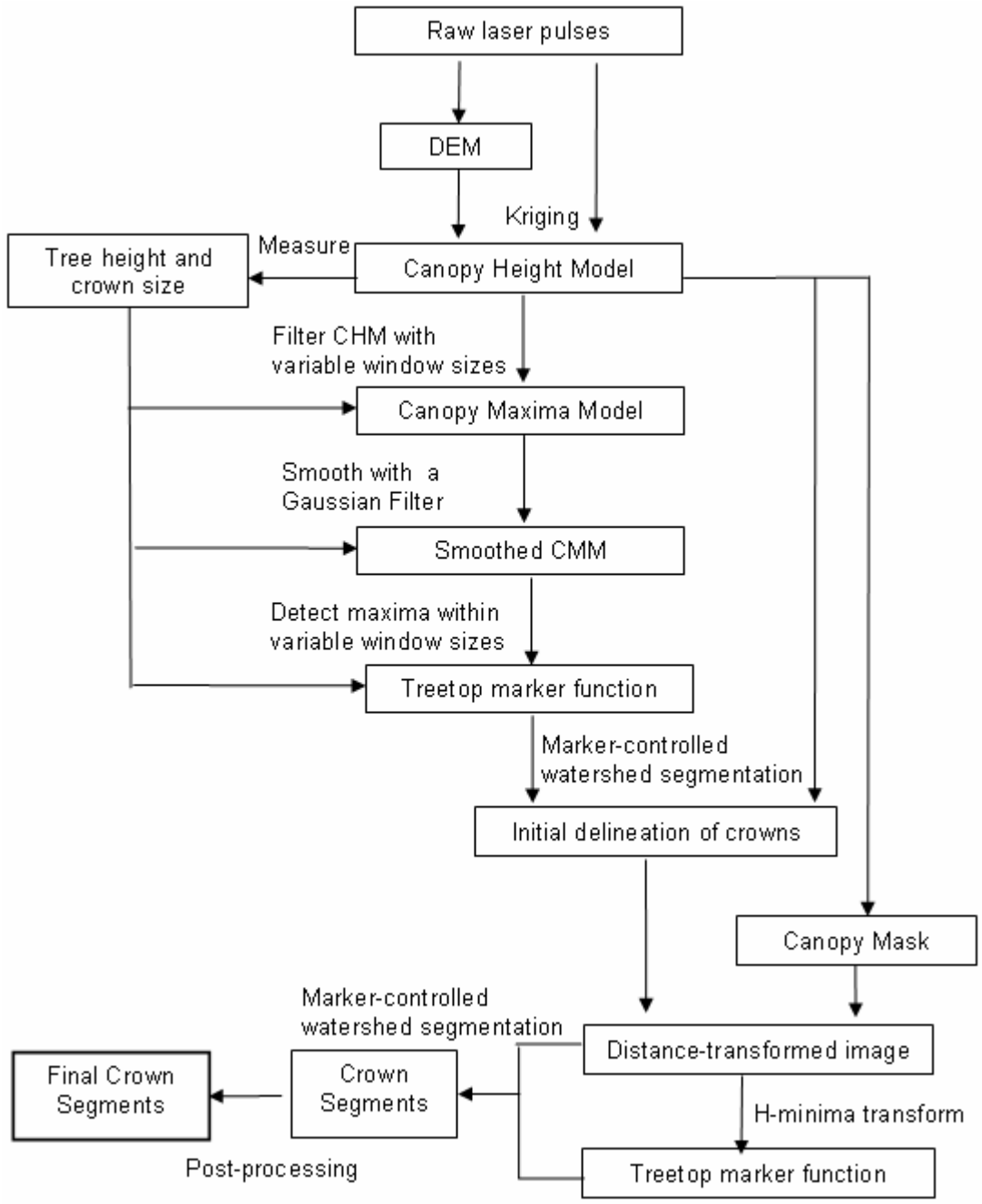

Figure 2.7. Flow chart of the method for tree isolation.

Because there are some dead trunks and some instruments for ecological studies in the sites, the segments were post-processed by removing all segments which are shorter than 2m. Also all segments adjoining the boundary of the study site were

removed. The whole procedure for isolating individual trees is illustrated in Figure 2.7.

3 Results and Discussions

3.1 Accuracy Assessment

To evaluate accuracy, a ground truth crown map for two transects (Figure 2.8), each with an area of 100 by 300m, was acquired by manually delineating the crowns boundaries on the prints of the CHM in the field. Airphotos were used in the field to aid the delineation of tree crowns. After the crown boundaries had been outlined in the field, they were further verified and refined by examining the laser point cloud with a 3D visualization software (ArcGIS 3D Analyst, ESRI) in the laboratory. There are a total of 772 trees in the two transects. The absolute accuracy for tree isolation (AATI) was used for evaluating delineation accuracy:

$$\mathrm{AATI} = \frac{N_{1,1}}{N_r} \tag{8}$$

where $N_{1,1}$ is the number of crowns which has one-to-one relationship with the ground truth crown polygon, N_r is the number of crowns in the field, and N_s is the total number of automatically delineated segments. One-to-one relationship means that the overlaying area S_o between a ground truth crown polygon and one segment overlaying with it is within the range of $S_r \pm 10\% * S_r$, where S_r is the area of the reference crown polygon.

There are two free parameters in the tree isolation method: α in equation (4) and h in equation (7). The tree isolation accuracy was assessed by the five-fold cross-validation method, which divided the ground truth data into five folds

randomly. Each time four folds were used for training and the parameters that achieved the highest AATI for the training data were used to evaluate the accuracy of the fold left out. This process was repeated for five times and the accuracies for five folds were averaged. When parameters were tuned, the domains of α and h were limited to be {0.01, 0.1, 0.2, 0.3, 0.4, 0.5} and {0.1, 0.2, 0.3, 0.4, 0.5, 0.6, 0.7}, respectively. It was found that when any four folds were used for training, the highest AATI was obtained when the highest AATI was obtained when α was 0.01 and h was 0.5m. The AATI for different folds varied from 61.3% to 68.2%. The average cross-validation accuracy was 64.1%. With these parameters values, there were a total of 9386 segments delineated (Figure 2.8).

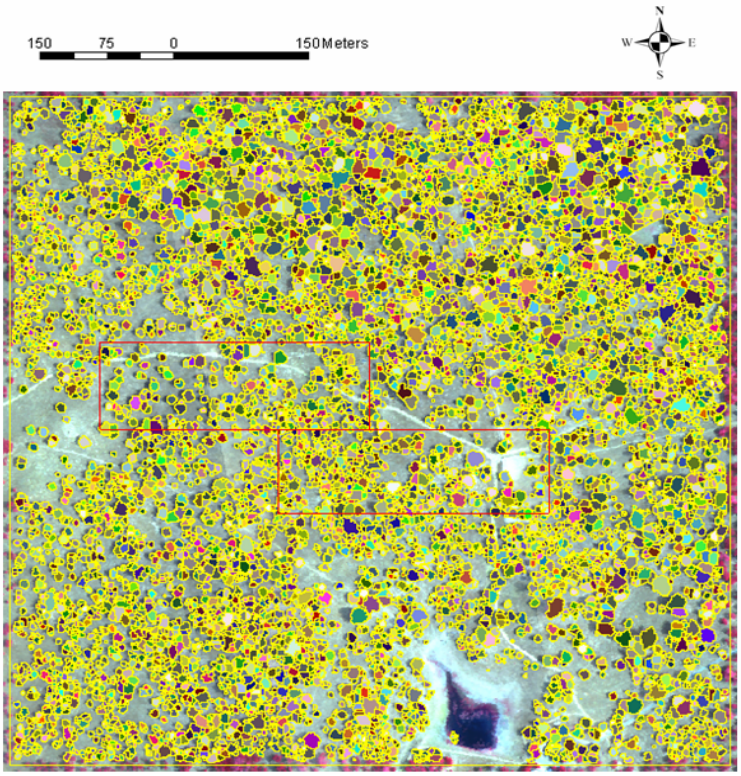

Figure 2.8. Crown delineation map (α=0.01 and h=0.5m). The two rectangles show the locations of transects for accuracy assessment.

Because different studies use different accuracy assessment methods, it is difficult to compare our accuracy with those from other studies. Persson *et al*. (2002) delineated crown segments of conifers such as Norway spruce, Scot pines, and Birch in southern Sweden. They linked the segments with field trees by searching all segments within two pixels (2/3m) around a field tree. In total, 71 percent of trees were correctly detected. Brandtberg *et al*. (2003) adopted the fuzzy concept to quantify the accuracy of the segmentation results and designed an index *A*, the value of which is 1 if the segment polygon overlaid perfectly with the delineated polygon in the field. Finally, their *A* values varied from 0.21 to 0.35 for six 1-ha plots in a deciduous forest with species including oaks, maple and poplar. Leckie *et al*. (2003) treated it as a "perfect" match when there is a one-to-one correspondence between ground reference polygons and delineated segments and their overlaps are greater than 50%. They obtained a 59% "perfect" match for a conifer forest. When compared with these studies, the criteria for accuracy assessment used in this study are much stricter. Therefore, the accuracy obtained with our method is encouraging.

3.2 Effects of α and h

To examine the effects of *α* and *h*, the AATIs for all combinations of these two parameters were calculated for all trees in the ground truth transects (Table 2.3).

Table 2.3. Tree isolation accuracy

AATI	h=0.1	h=0.2	h=0.3	h=0.4	h=0.5	h=0.6	h=0.7
α=0.01	59.2%	60.8%	62.0%	62.8%	64.1%	63.3%	62.3%
α=0.1	58.4%	59.2%	60.5%	61.9%	62.8%	61.7%	60.1%
α=0.2	57.9%	58.2%	58.8%	60.4%	62.6%	61.3%	59.8%
α=0.3	57.3%	57.1%	57.6%	58.4%	59.7%	58.4%	56.9%
α=0.4	57.0%	56.9%	57.5%	58.2%	59.2%	58.2%	56.9%
α=0.5	56.7%	56.6%	57.3%	57.8%	58.8%	57.5%	56.1%

When investigating the effects of the threshold *h* on tree isolation accuracy, there was a consistent pattern showing that *h*=0.5m is the best value for this dataset (Figure 2.9 (a)). When *h* is very small, spurious local minima could be counted as treetops and tree crowns will be over-segmented. When h is very large, treetops will be missed, leading to the under-segmentation issues. Therefore, when *h* lies between these two extrema, the highest accuracy can be obtained. For α, it seems that the tree isolation accuracy increases when decreasing α. One of the possible reasons is that when using smoothed CMM to detect treetops, the commission errors have been greatly reduced. As a result, decreasing α will reduce the omission errors while having little effects on the commission errors (Figure 2.9(b)).

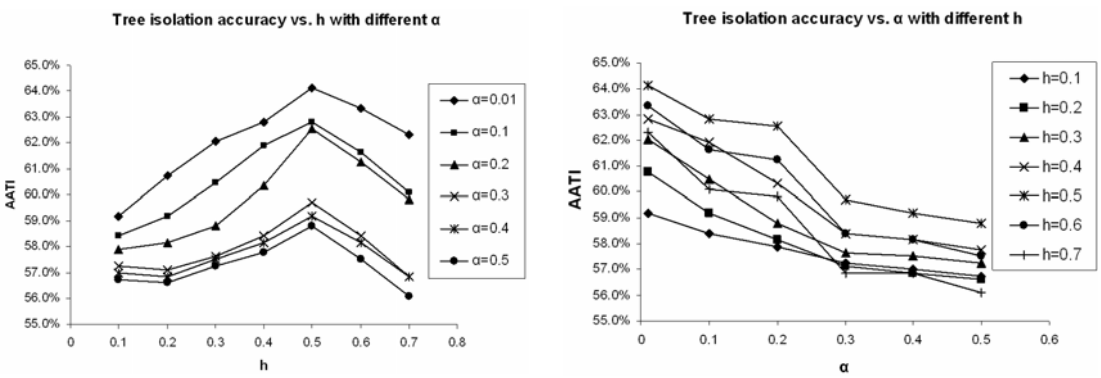

(a) (b)

Figure 2.9. The effects of parameters on tree isolation.

3.3 Comparison of Different Treetop-detection Methods

In addition to the above method, three other methods of treetop detection were applied into marker-controlled watershed segmentation for tree isolation: 1) the first method was based on Popescu and Wynne (2004), which detected treetops by searching local maxima within variable window sizes in the CHM. The window sizes were determined by the fitted regression curve, 2) in the second method,

treetops were detected from the CMM and variable window sizes were determined by the lower-limit of the prediction interval of the regression curve, but the distance-transformed image was not used for detecting treetops, and 3) in the third method, treetops were detected by finding local maxima in the CHM. For all of these three methods, the segmentation function is the CHM.

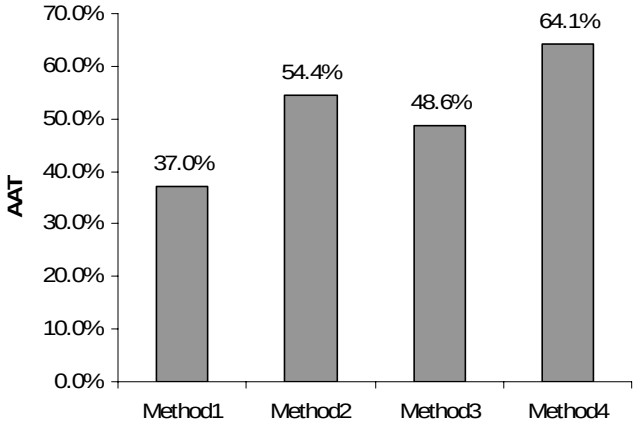

Figure 2.10. Comparison of tree isolation accuracy from different treetop detection methods. Method 1: detect treetops from CHM and window sizes are based on the fitted regression curve; method 2: detect treetops from CMM and window sizes are based on the lower-limit of the prediction interval of the regression curve; method 3: treetops are local maxima within CHM; and method 4: detect treetops from distance-transformed image in addition to method 3.

The AATIs for these three methods were 37.0%, 54.4%, and 48.6%, respectively (Figure 2.10). The method based on Popescu and Wynne (2004) had the lowest accuracy. This is not surprising since previous analysis shows that potentially about a half number of trees would be missed if window sizes are determined by the fitted regression curve. In the second method, the accuracy was much higher than

that in the first method when treetops were detected from the CMM and the window sizes were determined by the lower-limit of the prediction interval. Compared with the second method, the method which additionally detected treetops from distance-transformed image can increase the accuracy by about 10%. The accuracy from the third method is also higher than Popescu and Wynne (2004)'s method. This is because the omission errors in this method are low.

3.4 Error Analysis

The omission and commission errors will lead to under- or over-segmentation of tree crowns. When the branches of neighboring trees are interwinded or trees with different heights are growing closely, it is usually difficult to separate them. The over-segmentation problem mostly occurred for very old oak trees. These old and large oak trees usually grow in open space. With little competition of light and nutrient with surrounding trees, their branches can reach far in various directions and grow into irregular shape. When each large branch looks like a tree, the over-segmentation problem happens. When the "valleys" among trees were not discernable in CMM or distance-transformed image, the crown boundaries were wrongly delineated.

4 Conclusion

In this study, previous methods of detecting treetops by searching local maxima within variable window sizes were revisited and it was found that using fitted regression curve to determine window sizes could lead to large omission errors. The proposed method intended to reduce the omission and commission errors in

three means: 1) creating a CMM to reduce the spurious local maxima, 2) detecting treetops from the CMM using variable window sizes which were based on the lower limit of the prediction intervals, and 3) detecting treetops using distance-transform, which was based on the fact that treetops are located around the center of each crowns. The first means was to reduce commission errors and the rest two were to reduce omission errors. It was found that this "divide-and-conquer" method can achieve much higher accuracy than traditional methods. Also, applying distance-transform image to detect treetops can significantly increase the tree isolation accuracy. However, compared with previous methods, this method requires field data to train two additional parameters α and h. More research is needed to test this method over other forest types and examine the effects of α and h. Overall, the accuracy of this method is encouraging, especially considering the strict criteria used in accuracy assessment. The results showed that marker-controlled watershed segmentation can be used for isolating individual trees for deciduous tree species. The tree isolation results can be further used to extract other forest parameters such as tree height, crown size, biomass, and LAI. With individual tree information extracted from remotely sensed data, biogeochemistry models can be parameterized to scale up from individual trees to landscapes for better understanding of various ecological processes.

References

Baldocchi, D.D., L. Xu, and N. Kiang, 2004. How plant functional-type, weather, seasonal drought, and soil physical properties alter water and energy fluxes of an

oak-grass savanna and an annual grassland, *Agricultural and Forest Meteorology*, 123:13-39.

Beucher, S., and C. Lantuejoul, 1979. Use of watersheds in contour detection, *International Workshop on image processing, real-time edge and motion detection/estimation*, Rennes, France.

Brandtberg, T., and F. Walter, 1998. Automated delineation of individual tree crowns in high spatial resolution aerial images by multiple-scale analysis, *Machine Vision and Applications*, 11:64-73.

Brandtberg, T., T.A. Warner, R.E. Landenberger, and J.B. McGraw, 2003. Detection and analysis of individual leaf-off tree crowns in small footprint, high sampling density lidar data from eastern deciduous forest in North America, *Remote Sensing of Environment*, 85:290-303.

Chen, Q., P. Gong, and D. D. Baldocchi., 2004. Filtering airborne laser scanning data with morphological methods, *Photogrammetric Engineering and Remote Sensing*, submitted.

Clark, D. B., C. S. Castro, L. D. A. Alvarado, and J. M. Read, 2004a. Quantifying mortality of tropical rain forest trees using high-spatial-resolution satellite data, *Ecological Letters*, 7:52-59.

Clark, D. B., J. M. Read, M. L. Clark, A. M. Cruz, M. F. Dotti, and D. A. Clark, 2004b. Application of 1-m and 4-m resolution satellite data to ecological studies of tropical rain forests, *Ecological Applications*, 14:61-74.

Dralle, K., and M. Rudemo, 1996. Stem number estimation by kernel smoothing of

aerial photos, *Canadian Journal of Forest Research*, 26:1228–1236.

Gong, P., G.S. Biging, S.M. Lee, X. Mei, Y. Sheng, R. Pu, B. Xu, K. Schwarz, and M. Mostafa, 1999. Photo ecometrics for forest inventory, *Geographic Information Science*, 5:9-14.

Gong, P., Y. Sheng, and G.S. Biging, 2002. 3D Model-based Tree measurement from high-resolution aerial imagery, *Photogrammetric Engineering and Remote Sensing*, 68:203-1212.

Gougeon, F.A., 1995. A crown-following approach to the automatic delineation of individual tree crowns in high spatial resolution aerial images, *Canadian Journal of Remote Sensing*, 21: 274–284.

Gougeon, F.A., and D.G. Leckie, 1999. Forest Regeneration: Individual Tree Crown Detection Techniques for Density and Stocking Assessment, *Proceedings of the International Forum on Automated Interpretation of High Spatial Resolution Digital Imagery for Forestry*, 10–12 February 1998, Victoria, B.C. Pacific Forestry Center, Canadian Forest Service, Natural Resources Canada, pp. 11–23.

Hahn, G. H. and W. Q. Meeker, 1991. *Statistical Intervals: A Guide for Practitioners*, John Wiley & Sons, Inc., New York.

Hyyppä, J., O. Kelle, M. Lehikoinen, and M. Inkinen, 2001. A segmentation-based method to retrieve stem volume estimates from 3-D tree height models produced by laser scanners, *IEEE Transactions on Geoscience and Remote Sensing*, 39:969-975.

Kelly, M., D. Shaari, Q. H. Guo, and D. S. Liu, 2004. A comparison of standard and hybrid classifier methods for mapping hardwood mortality in areas affected by

"sudden oak death", *Photogrammetric Engineering and Remote Sensing*, 70:1229-1239.

Kiang, N.Y., 2002. *Savannas and seasonal drought: The landscape-leaf connection through optimal stomatal control,* PhD dissertation, Department of Environmental Science, Policy, and Management, University of California at Berkeley, Berkeley, California, 303p.

Larsen, M., and M. Rudemo, 1998. Optimizing templates for finding trees in aerial photographs, *Pattern Recognition Letters*, 19(12):1153-1162.

Leckie, D.G., X. Yuan, D.P. Ostaff, H. Piene, and D.A. Maclean, 1992. Analysis of high spatial resolution multispectral MEIS imagery for spruce budworm damage assessment on a single tree basis, *Remote Sensing of Environment*, 40:125-136.

Leckie D., F. Gougeon, D. Hill, R. Quinn, L. Armstrong, and R. Shreenan, 2003. Combined high-density lidar and multispectral imagery for individual tree crown analysis, *Canadian Journal of Remote Sensing*, 29(5):1-17.

Levesque, J., and D.J. King, 1999. Airborne digital camera image semivariance for evaluation of forest structural damage at an acid mine site, *Remote Sensing of Environment*, 68:112-124.

Meyer, F., and S. Beucher, 1990. Morphological segmentation, *Journal of Visual Communication and Image Representation*, 1:21-46.

Persson, Å, J. Holmgren, and U. Söderman, 2002. Detecting and measuring individual trees using an airborne laser scanner, *Photogrammetric Engineering and Remote Sensing*, 68:925-932.

Pollock, R., 1996. *The Automatic Recognition of Individual Trees in Aerial Images of Forests Based on a Synthetic Tree Crown Model*, Ph.D. dissertation, Department of Computer Science, University of British Columbia, Vancouver, B.C.

Popescu, S. C., R. H. Wynne, and R. F. Nelson, 2003. Measuring individual tree crown diameter with lidar and assessing its influence on estimating forest volume and biomass, *Canadian Journal of Remote Sensing*, 29:564-577.

Popescu, S.C., and R.H. Wynne, 2004. Seeing the trees in the forest: using lidar and multispectral data fusion with local filtering and variable window size for estimating tree height, *Photogrammetric Engineering & Remote Sensing*, 70, 589-604.

Pouliot, D. A, D. J. King, F. W. Bell, and D. G. Pitt, 2002. Automated tree crown detection and delineation in high-resolution digital camera imagery of coniferous forest regeneration, *Remote Sensing of Environment*, 82:322–334.

Schardt, M., M. Ziegler, A. Wimmer, R. Wack, and J. Hyyppae, 2002. Assessment of Forest Parameters by Means of Laser Scanning, *International Archives of Photogrammetry and Remote Sensing*, XXXIV part 3A. pp.302-309, Graz, Austria.

Sithole, G. and G. Vosselman, 2003. Comparison of filtering algorithms, *Proceedings of the ISPRS working group III/3 workshop "3-D reconstruction from airborne laserscanner and InSAR data"*, URL:Uhttp://www.isprs.org/commission3/wg3/workshop_laserscanning/U, 8-10 October 2003, Dresden, Germany (last date accessed: 28 February 2004)

Soille, P., 2003. *Morphological image analysis: principles and applications, 2nd edition*, Springer-Verlag, Berlin, Germany, 391p.

Wang, L., P. Gong, and G. S. Biging, 2004. Individual tree-crown delineation and treetop detection in high-spatial-resolution aerial imagery, *Photogrammetric Engineering and Remote Sensing*, 70:351-358.

Wulder, M., K. O. Niemann, and D. Goodenough, 2000. Local maximum filtering for the extraction of tree locations and basal area from high spatial resolution imagery, *Remote Sensing of Environment*, 73:103-114.

Chapter 3 Estimating Basal Area and Stem Volume for Individual Trees from LIDAR Data

Abstract

This study proposed a new metric called canopy geometric volume G, which is derived from small-footprint LIDAR data, for estimating individual-tree basal area and stem volume. Based on the plant allometry relationship, we found that basal area B is exponentially related to G ($B=\beta_1 G^{3/4}$, where β_1 is a constant) and stem volume V is proportional to G ($V=\beta_2 G$, where β_2 is a constant). The models based on these relationships were compared with a number of models that based on tree height and/or crown diameter. The models were tested over individual trees in a deciduous oak woodland in California in the cases that individual tree crowns are either correctly or incorrectly segmented. When trees are incorrectly segmented, the theoretical model $B=\beta_1 G^{3/4}$ has the best performance (adjusted R^2, R_a^2=0.78) and the model $V=\beta_2 G$ has the second to the best performance (R_a^2=0.78). When trees are correctly segmented, the theoretical models are among the top three models for estimating basal area (R_a^2=0.77) and stem volume (R_a^2=0.79). Overall, these theoretical models are the best when considering a number of factors such as the performance, the model parsimony, and the sensitivity to errors in tree crown segmentation. Further research is needed to test these models over sites with multiple species.

1 Introduction

Accurate forest structural information is crucial to a number of applications including forest management (Maltamo *et al.*, 2004a), fire behavior analysis (Riaño *et al.*, 2004), and global warming and carbon management (Birdsey and Lewis, 2002). Compared to optical remotely sensed imagery, LIDAR (Light Detection and Ranging) can directly measure the vertical canopy information and is gaining popularity in forest and ecological studies (Lefsky *et al.*, 2002a; Hall *et al.*, 2005). With the high pulse-density of small-footprint LIDAR data, nowadays it is possible to isolate individual trees and directly extract individual-tree locational and dimensional parameters including treetop locations, tree heights, crown sizes, and even crown boundaries (e.g., Popescu *et al.*, 2003; Hyyppä *et al.*, 2001; Persson *et al.*, 2002). We developed a new method to delineate individual tree crowns in a savanna woodland in California using small-footprint LIDAR data (Chen *et al.*, 2006). This companion study is to further extract individual-tree structural parameters including basal area and stem volume, which cannot be directly measured by LIDAR but can be potentially related to tree dimensional information such as tree height and crown size. This study is part of a large project, in which we parameterize an individual-tree based biogeochemical model called MAESTRA (Medlyn, 2003) for spatially-explicit ecological modeling.

Extracting individual-tree structural parameters from small-footprint LIDAR data is useful not only for our detailed ecological modeling but also for the large-scale

forest inventory. There are at least three kinds of methods to perform the large-scale forest inventory with small-footprint LIDAR data: the first is called *stand-level regression method*. This method is to create regression models between canopy structural parameters and the laser pulses statistics at the stand or plot levels (Means *et al.*, 2000; Holmgren *et al.*, 2003; Næsset *et al.*, 2004; Næsset, 2004; Riaño *et al.*, 2004; Hall *et al.*, 2005). The statistics used in the regression models typically include the height mean, minimum, maximum, variance, coefficient of variance, percentiles, and the percentage of canopy returns.

The second is called *individual-tree integration method*. If the tree dimensional information such as individual tree height and crown size can be accurately extracted, the individual tree canopy structure parameters can be derived based on allometric equations or regression models (Hyyppä, *et al.*, 2001; Persson *et al.*, 2002; Næsset and Økland, 2002; Riaño *et al.*, 2004; Roberts *et al.*, 2005). Then, the canopy structure information over a large area can be obtained by simply integrating individual tree values. Compared to the *stand-level regression method*, the ground truth canopy structure measurements for developing the regression models are needed only for a sample of trees instead of many of plots or stands, which can significantly reduce the field work. However, not many studies have used the *individual-tree integration method* for the large-scale forest inventory because previous research has shown that the accuracy of isolating individual trees is typically low due to the complexity of canopy surface (Persson *et al.*, 2002; Brandtberg *et al.*, 2003; Leckie *et al.*, 2003; Maltamo *et al.*, 2004a; Morsdorf *et al.*,

2004). We applied a method by Popescu and Wynne (2004) to our study site, a woodland of deciduous oak trees, and obtained an accuracy of 37%; when we used an improved method that can reduce both the commission errors and omission errors, the accuracy increased to 64.1%, which is still not very high (Chen *et al.*, 2006).

Although the low accuracy of the individual tree analysis methods makes it difficult to integrate individual tree values to obtain the forest canopy structure information over a large area (Riaño *et al.*, 2004), especially in deciduous forests, some researchers found that the individual tree analysis results are useful for predicting stand-level information with a method called *hybrid regression method*. In this method, a series of plot or stand level statistics are first derived based on the individual tree isolation results, such as the total number of trees, the maximum and mean tree height, and the mean crown size. Then, these statistics are used in the regression models for predicting canopy structure parameters at the plot or stand level (Holmgren *et al.*, 2003; Popescu *et al.*, 2003; Popescu *et al.*, 2004; Maltamo *et al.*, 2004b). Such a method might improve the accuracy of forest plot/stand structural information prediction (Popescu *et al.*, 2003) but cannot reduce the field work since the ground-truth measurements still need be collected at the plot or stand level for developing the models.

Since the *individual-tree integration* method can minimize the field work, it is expected to have great potential in the large-scale forest inventory, especially if we can develop some individual-tree level models that are not much affected by the

errors in tree isolation and crown delineation. To search for such models, let us assume that the structure parameter Y_i for a tree *i* is related to a LIDAR metric X_i by:

$$Y_i=f(X_i) \quad (1)$$

Suppose this tree is over-segmented into *n* parts and the corresponding metrics are: $X_{i,1}, X_{i,2}, \ldots, X_{i,n}$.

Then the predicted structure parameter $Y_{p,i}$ is:

$$Y_{p,i}= f(X_{i,1})+f(X_{i,2})+\ldots+f(X_{i,n}) \quad (2).$$

If assume that (i) the structural parameter Y is proportional to the LIDAR metric X ($Y=\alpha X$, where α is a constant) even at the scale of a part of a tree, which means

$$f(X_{i,1})+f(X_{i,2})=f(X_{i,1}+ X_{i,2}) \quad (3),$$

and (ii) the sum of the LIDAR metrics for each part is equal to the LIDAR metric for the tree:

$$X_{i,1}+X_{i,2}+\ldots+X_{i,n}= X_i \quad (4),$$

then $Y_{p,i}= f(X_{i,1})+f(X_{i,2})+\ldots+f(X_{i,n})= f(X_{i,1}+ X_{i,2}+\ldots+ X_{i,n})= f(X_i)=Y_i$. This means that if Equations (3) and (4) are satisfied, the predicted canopy structure parameter will not be affected by the over-segmentation of tree crowns. It is easy to verify that this is also true in the case of the under-segmentation of tree crowns. Our hypothesis is that if either or both equations are satisfied the prediction of canopy structural

parameters is not much affected by the errors of tree isolation and crown segmentation. So, now the question is to find some metrics that satisfy Equation (4) and test whether the canopy structural parameter is proportional to the metrics (Equation (3)).

There are at least two LIDAR metrics that satisfy Equation (4): crown area and canopy geometric volume. Crown area has been used in a number of studies for estimating canopy structure parameters (e.g., Holmgren *et al*., 2003; Maltamo *et al*., 2004b). However, canopy geometric volume (denoted as G) is a new metric first proposed in this study. Therefore, the main objective of this study is to examine (a) whether basal area and stem volume are proportional to canopy geometric volume, and if not, what the functional relationships are, and (b) how the different models based on canopy geometric volume perform when tree crowns are incorrectly segmented. Since trees are growing in a three-dimensional space, it is hypothesized that their canopy structural characteristics can be better predicted with three-dimensional metrics such as canopy geometric volume. Thus, the second objective of our study is to compare the models based on canopy geometric volume with those based on either canopy height or crown size metrics. In the companion study on tree isolation (Chen *et al.*, 2006), we found that some tree crowns were over-segmented (a tree on the ground is segmented into several parts) or under-segmented (several trees on the ground correspond to only one segment) due to the irregular canopy shape and the coexistence of dominant and co-dominant trees in deciduous forests. Correspondingly, we will address the above research questions

by testing the models over correctly and incorrectly segmented trees, respectively.

2 Materials and Methods

2.1 Study area

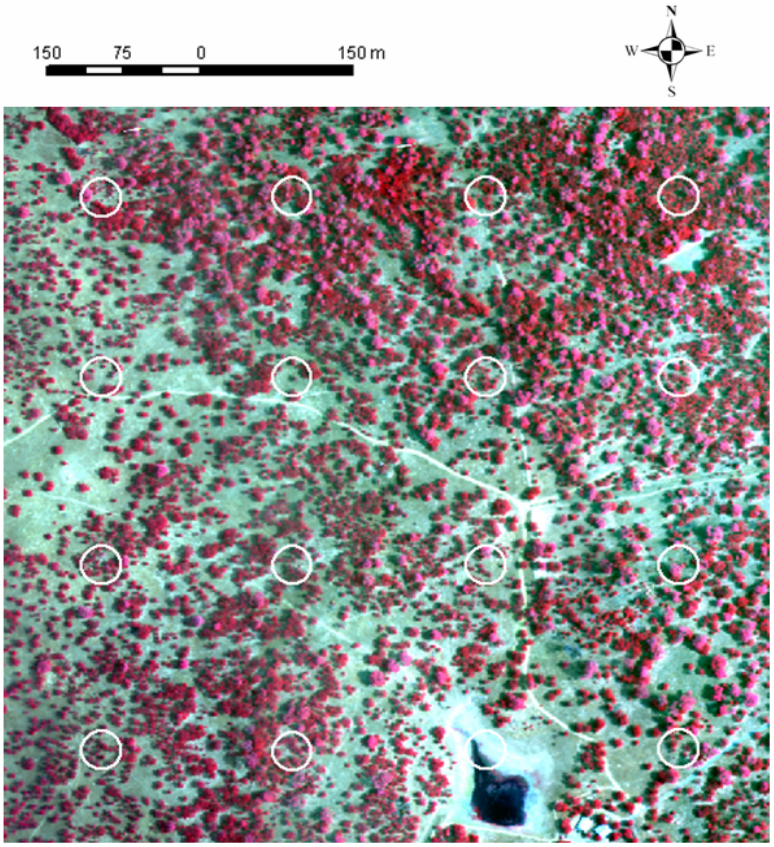

Figure 3.1. The sample plots in the study area. Plots are systematically distributed and each has an area of 0.13ha.

The study site is an open oak savanna woodland, located near Ione, California (latitude: 38.26'N, longitude: 120.57'W) (Figure 3.1). The site is on a private ranch and is part of the AmeriFlux network of eddy covariance field sites (Baldocchi *et al.*, 2004). The landscape is characterized by flat terrain (with a maximum slope of less than 15%) with a scattered, clumped distribution of blue oaks (*Quercus douglasii*)

and a minority of grey pines (*Pinus sabiniana*) over a continuous layer of Mediterranean annual grasses.

2.2 LIDAR data

On August 24, 2003, laser altimetry data were acquired with an Optech ALTM 2025, which recorded both first and last returns for each laser pulse. The scanning pattern was z-shaped. The scanning angle is 17° and the flying altitude was about 500m, corresponding to a swath of about 300m. The data provider claimed that the vertical accuracy and horizontal accuracy are 18cm and 17cm with 95% confidence. The footprint size was about 18 cm. The average posting density was 9.5 points per square meter, resulting in an average spot spacing of about 32 cm. To obtain such a high pulse density, the site was flown over twice. The data covering 800m by 800m around the eddy covariance tower were used to segment individual tree crowns (Chen *et al.*, 2006).

2.3 Field data

Ground truth data were collected for 16 circular plots systematically distributed over the study area, with a spacing of 200m in two perpendicular directions (Figure 3.1). Each plot has an area of about 0.13ha and a radius of 20m. The centers of the plots were located with a Trimble AgGPS 132 receiver. The claimed "pass-to-pass" accuracy measured over a 15-minute time period is 10-30cm. Under forest canopy, GPS systems tend to produce from 1.5 to 3 times less accurate solutions (Popescu *et al.*, 2003). Since the trees in this woodland are more sparsely distributed than those

in Popescu *et al.*'s study site, it is expected that the accuracy of plot center measurements was at the submeter level.

The tree height and DBH (diameter at breast height) were measured for all trees larger than 12.5cm DBH. A total of 313 oak trees and eight grey pines were located in these plots. Since the number of grey pines is too small to perform reliable regression analysis, this study only focused on the blue oak trees. The tree height was measured to the nearest 0.1m with a laser rangefinder (Opti-LOGIC, Tullahoma, TN) and the DBH was measured to the nearest 0.01m. The basal area of individual trees was calculated from the measurements of DBH. Based on the measurements of tree height and DBH, the stem volume for individual trees was calculated using the blue oak allometric equation developed by Pillsbury and Kirkley (1984).

2.4 LIDAR metrics

The tree crown segments automatically generated from LIDAR data (Chen *et al.*, 2006) were used to extract relevant the LIDAR metrics for basal area and stem volume estimation. There were a total of 291 segments corresponding to the blue oaks in these plots. For each tree segment, a total of 44 metrics (42 height metrics, crown area, and canopy geometric volume G) were extracted (Table 3.1). All of these metrics except the canopy geometric volume G have been applied in previous studies (Means *et al.*, 2000; Næsset and Økland, 2002; Popescu *et al.*, 2003). The canopy height metrics H_x were calculated based on the laser pulses falling in each segment. The height statistics, including percentile from 0 to 100 by 10, mean,

standard deviation, and coefficient of variance, were calculated for first, last, and all canopy returns, respectively. Canopy returns were defined as the returns that are 0.5m higher than the ground. The crown area C_d is the area of each crown segment. The canopy geometric volume G of each segment is the volume under the canopy height model (CHM). To produce a CHM, a DEM was first created with a method developed by Chen *et al.* (in press) and then the relative canopy height of laser pulses was interpolated into a CHM by kriging (Chen *et al*., 2006).

Table 3.1. The LIDAR metrics used in the regression models

Independent variables		Dependent variables
Category	Metrics	
Canopy height (H_x , m)	For first canopy returns, $H_{i,f}$, where i=0,10, …,100%, percentile height $H_{mean,f}$, mean of height $H_{std,f}$, stand deviation of height $H_{cv,f}$, coefficient of variance of height For last canopy returns, $H_{i,l}$, where i=0,10, …,100%, percentile height $H_{mean,l}$, mean of height $H_{std,l}$, stand deviation of height $H_{cv,l}$, coefficient of variance of height For all canopy returns, $H_{i,a}$, where i=0,10, …,100%, percentile height $H_{mean,a}$, mean of height $H_{std,a}$, stand deviation of height $H_{cv,a}$, coefficient of variance of height	Basal Area: (B, m^2) Stem Volume: (V, m^3)
Crown area (C_a, m)	The area of individual crown segment	
Canopy geometric volume (G, m^3)	The geometric volume for a segment under the CHM	

2.5 Regression analysis

The regression models were developed only based on the correctly segmented trees, which are those that have 1-to-1 relationship with the LIDAR-derived tree segments. A 1-to-1 relationship means that the overlaying area S_o between a crown polygon validated in the field and its corresponding segment is within the range of $S_r \pm 10\%*S_r$, where S_r is the area of the validated crown polygon (Chen *et al.*, 2006). The regression models for predicting basal area and stem volume are summarized in Tables 2 and 3, respectively.

Table 3.2. The models for predicting basal area

No.	*General form of the models*	*Number of specific models*
B.1	$B = \beta_1 H_x^c$	42
B.2	$B = \beta_1 C_a^c$	1
B.3	$B = \beta_1 G^c$	1
B.4	$B = \beta_1 G$	1
B.5	$B = \beta_1 G^{3/4}$	1
B.6	$DBH=\beta_0 + \beta_1 H_x + \beta_2 C_a$ $B=\pi(DBH/2)^2$	42
B.7	B=stepwise({H_x}, C_a, G)	1
B.8	B=stepwise({H_x}, C_a)	1
B.9	B=stepwise({H_x})	1

The univariate power models were developed with tree height, crown area, or geometric canopy volume as independent variables, respectively (Models B.1-3 and V.1-3). These power functions are justified by the theories in plant science: many structure and functional variables of organisms (Y) scale as power functions of measures of sizes (S) such as body mass, length, diameter, area, and volume (Norberg, 1988; West *et al.*, 1999; Enquist, 2002):

$$Y=\alpha S^{\beta}, \quad (5)$$

where α is a constant that varies with the type of variables and the kind of plants, and β is the allometric exponent. The power models, especially with height, have been used in a number of studies (e.g., Lim *et al.*, 2003; Hall *et al.*, 2005).

Table 3.3. The models for predicting stem volume

No.	*General form of the model*	*Number of specific models*
V.1	$V = \beta_1 H_x^c$	42
V.2	$V = \beta_1 C_a^c$	1
V.3	$V = \beta_1 G^c$	1
V.4	$V = \beta_1 G$	1
V.5	$DBH = \beta_0 + \beta_1 H_x + \beta_2 C_a$ V=allometric(DBH, $H_{100,a}$)	42
V.6	V=stepwise($\{H_x\}$, C_a, G)	1
V.7	V=stepwise($\{H_x\}$, C_a)	1
V.8	V=stepwise($\{H_x\}$)	1

* $\{H_x\}$ means the set of all height metrics.

With canopy geometric volume as the independent variable, we test two kinds of models. First, a simple linear regression model with no intercept was tested for basal area and stem volume, respectively, since such a model satisfies Equations (3) and (4) and therefore has an advantage of not being affected by the errors of tree isolation (Models B.4 and V.4). Second, we developed theoretical models based on the recent progresses in the plant allometry: Enquist (2002) found such allometric relationships: $DBH \propto M^{3/8}$ and $H \propto M^{1/4}$, where M is the plant mass and H is the tree height. If assuming that the plant is filled with a tissue density that is approximately constant across sizes, the plant mass M is proportional to canopy geometric volume G (West *et al.*, 1999; Enquist, 2002). Therefore, $DBH \propto G^{3/8}$ and $H \propto G^{1/4}$. Since basal area B $\propto DBH^2$ and stem volume $V \propto DBH^2 * H$,

$$B \propto DBH^2 \propto G^{3/4} \quad (6)$$

$$\text{and } V \propto DBH^2 * H \propto V^{3/4} * V^{1/4} \propto G. \quad (7)$$

Equation (6) indicates that theoretically the basal area is not proportional to the canopy geometric volume G, based on which Model B.5 is developed. However, Equation (7) indeed reveals that the stem volume V is proportional to canopy geometric volume G. This equation has significant implications since it can provide theoretical support for Model V.4.

Although these allometric equations are developed at the individual tree level, there is a biological basis for them to be applied over a part of canopy: most terrestrial

plants have a transport system that moves water, minerals, and nutrients through the plant body by plant tissues such as xylem and phloem. To support the maintenance and growth of leaves and branches within any certain portion of the canopy, there are corresponding conducting tubes in the stem for transporting water and nutrients (West et al., 1999), which correspond to a portion of basal area or stem volume. Therefore, canopy geometric volume can be related to basal area or stem volume even at the scale of a portion of an individual tree.

Besides the above univariate models, we also tested a multiple linear regression model that depend on both a height metric and crown area (Models B.6 and V.5). The hypothesis for these models is that the combination of the height and the crown area can characterize the canopy structure in a three-dimensional space (Hyyppä *et al.*, 2001, Holmgren *et al.*, 2003; Hall *et al.*, 2005). Finally, considering their popularity in many studies (Means *et al*., 2000; Næsset, 2002; Popescu *et al*., 2003), we tested stepwise regression models that depend on all metrics (Models B.7 and V.6), all height metrics plus crown area (Models B.8 and V.7), or all height metrics (Models B.9 and V.8), respectively.

2.6 Model Evaluation

The adjusted coefficient of determination and root mean square error were used for model evaluation. Although different formulas of R^2 exist, Kvålseth (1985) recommended the following equation to calculate the adjusted R^2:

$$R^2 = 1 - \frac{n-1}{n-p}\frac{\sum(y-\hat{y})^2}{\sum(y-\bar{y})^2} \tag{8}$$

where $\hat{y}$ is the fitted value of basal area or stem volume y, $\bar{y}$ is the mean of all y's, n is the number of observations, and p is the number of parameters in the regression model, not including the residual variance. The coefficient of determination (R^2) is perhaps the single most extensively used measure of goodness of fit for regression models (Kvålseth, 1985). However, there are problems with R^2 for the no-intercept model and for transformed variables (Anderson-Sprecher, 1994). Therefore, in addition to the above two statistics, the Akaike's information criterion (AIC) was used to compare different models.

Akaike's information criterion was developed from the Kullback-Leibler information, which can be used to quantify the distance between a regression model and reality. Based on the philosophy that reality cannot be modeled, AIC is to calculate the "relative" distance between the regression model and reality. In practice, the second-order bias correction version called AIC_c is used, especially when the sample size is small (Burnham and Anderson, 2002):

$$\mathrm{AIC_c} = n\log\left(\frac{\sum(y-\hat{y})^2}{n}\right) + 2K + \frac{2K(K+1)}{n-K-1} \tag{9}$$

In this case, K is the total number of parameters in the model, including the residual variance. Therefore, K equals p plus 1. The smaller the AIC_c, the more closely a model approaches reality.

The individual AIC_c values are not interpretable since they contain arbitrary constants (Burnham and Anderson, 2002). When comparing different models, the common practice is to rescale these values with the minimum value of these models:

$$\Delta_i = AIC_i - AIC_{min}, \tag{10}$$

where AIC_{min} is the minimum of the different AIC_i values. This transformation forces the best model to have $\Delta=0$, while the rest of the models have positive values. Some simple rules are often useful in assessing the relative merits of models: Models with $\Delta_i <=2$ have substantial support (evidence), those in which $4<=\Delta_i <=7$ have considerably less support, and models with $\Delta_i >10$ have essentially no support (Burnham and Anderson, 2002). In the following analysis, AIC_c is preferred for evaluating different models. However, adjusted R^2 and RMSE are also analyzed since they have been widely used and are likely to be in continued use in the future (Anderson-Sprecher, 1994).

It is noteworthy that although the regression models were developed only based on correctly-segmented trees, they were evaluated for correctly-segmented and mis-segmented trees, respectively. Due to the errors of the tree isolation algorithm, only 181 trees of all 313 trees in the field have a 1-to-1 relationship. The remaining trees could be over-segmented (1-to-m) (Figure 3.2(a)) or under-segmented (n-to-1) (Figure 3.2(b)). In some cases, although the outer boundaries of a group of trees were correctly delineated, the internal boundaries to divide these crown segments were incorrect, leading to an n-to-m relationship (Figure 3.2(c)). To test the model

performance when mis-segmentation occurs, a segment (in the case of n-to-1) or a group of segments (in the case of 1-to-m and m-to-n) were linked to the corresponding tree(s) observed on the ground so that the overlaying area between this or these segmented and the ground located tree(s) was within the range of $S_{r,g} \pm 10\%*S_{r,g}$, where $S_{r,g}$ is the area of the corresponding tree(s) identified on the ground. In doing so, a total of 67 pairs were formed between 110 segments and 132 trees. After the pairs of LIDAR-derived segments and trees identified on the ground had been formed, the total basal area and stem volume for segments and the corresponding trees on the ground were used to calculate the adjusted R^2, root mean square error, and AIC_c. The test of the models over the mis-segmented trees can help evaluate how the models are sensitive to the errors in tree isolation and crown delineation.

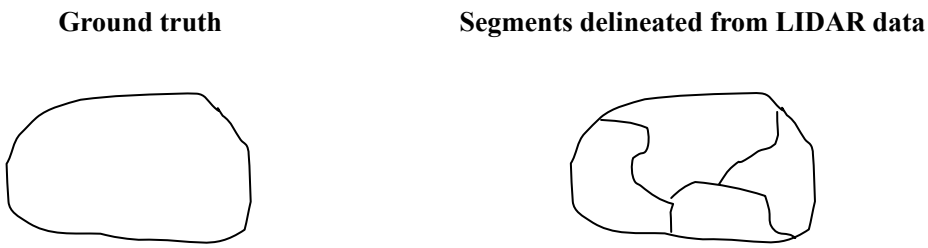

(a) 1-to-m (over-segmentation)

(b) n-to-1 (under-segmentation)

(c) n-to-m

Figure 3.2. Three possible cases that tree crowns are mis-segmented

3 Results

There are eight and nine general models for estimating basal area and stem volume, respectively. Note that for the general models that include height as independent variables, the number of the corresponding specific models should be multiplied by 42, the number of the height metrics. Therefore, there are a total of 89 and 131 specific models for basal area and stem volume estimation, respectively. For the models depending on any individual height metric, the maximum height of all laser pulses always leads to the best performance in this study, which will be discussed later in more detail. Therefore, only the fitting statistics for the models that depend on the maximum height are listed in Tables 4 and 5.

Among the models of predicting basal area, the power model B.1, which depends on the maximum height, is the worst. The best model for the correctly segmented trees is the model B.6, which depends on tree height and crown area. However, for the mis-segmented trees, the best model goes to the power model B.5, which predict basal area with the 3/4 power of the canopy geometric volume *G*.

Table 3.4. The fitting statistics for the models that predict basal area

Model	*Correctly segmented trees*				*Mis-segmented trees*				*Equation*
	R_a^2	RMSE ($10^{-3}m^2$)	AIC$_c$	Δ	R_a^2	RMSE ($10^{-3}m^2$)	AIC$_c$	Δ	
B.1	0.51	31.3	-1236.5	146.6	0.48	70.2	-314.4	51.9	$B = 0.0012H_{100,a}^{1.8}$
B.2	0.70	24.7	-1320.7	62.4	0.68	55.1	-343.5	22.8	$B = 0.0011C_a^{1.1}$
B.3	0.76	21.8	-1365.7	17.3	0.77	47.0	-362.6	<u>3.8</u>	$B = 0.0015G^{0.73}$
B.4	0.69	24.7	-1321.4	61.7	0.64	58.3	-337.8	28.5	$B = 0.0003G$
B.5	0.77	21.3	-1374.7	<u>8.4</u>	0.78	46.0	-366.3	<u>0.0</u>	$B = 0.0014G^{3/4}$
B.6	0.79	20.7	-1383.1	<u>0.0</u>	0.62	60.2	-331.6	34.7	$DBH=2.29+1.6H_{100,a}+0.26C_a$; $B=\pi(DBH/2)^2$
B.7	0.79	20.7	-1380.2	<u>2.9</u>	0.74	50.2	-350.7	<u>15.6</u>	$B = -0.008+0.0001G+0.005H_{100,f}-0.003H_{80,l}+0.0006C_a$
B.8	0.78	20.9	-1374.6	<u>8.4</u>	0.72	51.6	-344.4	21.9	$B = -0.03+0.012H_{mean,a}+0.005H_{100,f}+0.008H_{0,l} -0.007H_{10,l}-0.004H_{80,l}+0.001C_a$
B.9	0.62	27.4	-1279.8	103.3	0.61	61.1	-327.1	39.2	$B = -0.03+0.02H_{mean,a}-0.006H_{mean,l}-0.03H_{90,f}+0.04H_{100,l}$

* (1) For models B.1 and B.6, only the fitting statistics of the best model are listed. (2)The equations whose Δ values are the lowest three are underlined.

Table 3.5. The fitting statistics for the models that predict stem volume

Model	*Correctly segmented trees*				*Mis-segmented trees*				*Equation*
	R_a^2	RMSE (m^3)	AIC_c	Δ	R_a^2	RMSE (m^3)	AIC_c	Δ	
V.1	0.54	327.6	-395.4	146.0	0.58	730.8	-33.2	42.9	$V = 0.0026H_{100,a}^{2.4}$
V.2	0.64	289.4	-439.8	101.5	0.58	725.8	-34.1	42.0	$V = 0.0027C_a^{1.4}$
V.3	0.78	227.5	-525.9	15.4	0.77	538.1	-70.0	<u>6.1</u>	$V = 0.0028G^{1.008}$
V.4	0.79	219.1	-540.5	<u>0.8</u>	0.78	528.4	-73.3	<u>2.8</u>	$V = 0.0029G$
V.5	0.79	218.8	-540.6	<u>0.7</u>	0.57	738.1	-30.8	45.3	DBH= $-7.7 + 1.82H_{100,a} + 0.78C_a$; V=allometric (DBH, $H_{100,a}$)
V.6	0.80	217.3	-541.3	<u>0.0</u>	0.80	506.0	-76.1	<u>0.0</u>	$V = -0.06 + 0.003G + 0.08H_{std,f}$
V.7	0.76	234.0	-507.8	33.5	0.77	541.5	-58.9	17.2	$V = -0.07 + 0.1H_{mean,a} - 1.6H_{cv,l} + 0.08H_{0,l} - 0.16H_{10,l} - 0.06H_{30,l} - 0.05H_{80,l} + 0.16H_{100,l} + 0.01C_a$
V.8	0.65	283.4	-441.7	99.6	0.68	635.3	-43.1	33.0	$V = 0.04 + 0.14H_{mean,a} - 1.82H_{cv,a} - 0.12H_{70,f} - 0.14H_{10,l} - 0.1H_{30,l} + 0.29H_{100,l}$

* (1) For models V.1 and V.5, only the fitting statistics of the best model are listed. (2)The equations whose Δ values are the lowest three are underlined.

Among the models of predicting stem volume, neither the height metric H_x nor the crown area C_a is a good predictor when a power model is used. Like basal area, the power model V.1, which depends on the height metric H_x, is the worst for predicting stem volume. The best model for both correctly and incorrectly segmented trees is stepwise regression model V.6, which has all metrics as input variables initially and depends on the canopy geometric volume *G* and a height metric in the final model.

4 Discussion

4.1 Height metrics

Although the height metrics are the major predictors for most studies for estimating canopy structure parameters from LIDAR (e.g., Means *et al.*, 2000; Hyyppä *et al.*, 2001; Næsset 2002; Persson *et al.*, 2002; Lim *et al.*,2003; Popescu *et al.*, 2003; Maltamo *et al.*, 2004b; Hall *et al.*, 2005), this study shows that when a power model is used the height metric H_x is worse than the crown area C_a or the canopy geometric volume G for predicting either basal area or stem volume. When all the height metrics are combined to create stepwise regression models (Models B.9 and V.8), the models improve but are still worse than the power models depending on C_a or G (Models B.2-3 and V.2-3) for predicting basal area. For predicting stem volume, the stepwise regression model with all height metrics as input variables can achieve a slightly better performance than the power model depending on crown area C_a while the performance is still much worse than the power model depending on G.

Despite the height metrics are not powerful for predicting basal area and stem volume at the individual tree level, they have been most widely used for canopy structure parameter estimation since they can directly be derived from the LIDAR measurements. To explore more about these metrics, we compared the performance of the power models that depend on any individual height metric (Tables 6 and 7). Note that the adjusted R^2 values for some models are negative, which highlighted the preference of using AIC_c for model evaluation. The patterns of AIC_c values for different height metrics are similar for basal area and stem volume: among the four height statistics (including maximum, mean, standard deviation, and coefficient of variance), the order of overall performance from the best to the worst was maximum, standard deviation, mean, and coefficient of variance (see Tables 6 and 7). Among all percentile height metrics, the maximum height (100% percentile height) has the lowest AIC_c values and therefore the best performance (Figure 3.3). For the first canopy returns, there is a trend of improving performance when the height percentile increases from 0 to 100. Such a trend also exists for the last canopy returns except when the percentile is 0, where its AIC_c value is low than those at the immediate neighboring percentiles.

Table 3.6. The fitting statistics for the power models that predict basal area from height metrics

	First returns						*Last returns*						*All returns*					
	Correctly segmented			Mis-segmented			Correctly segmented			Mis-segmented			Correctly segmented			Mis-segmented		
Metric	R_a^2	RMSE ($10^{-3}m^2$)	AIC_c	R_a^2	RMSE ($10^{-3}m^2$)	AIC_c	R_a^2	RMSE ($10^{-3}m^2$)	AIC_c	R_a^2	RMSE ($10^{-3}m^2$)	AIC_c	R_a^2	RMSE ($10^{-3}m^2$)	AIC_c	R_a^2	RMSE ($10^{-3}m^2$)	AIC_c
H_0	-0.14	47.7	-1085.1	-0.19	106.5	-264.4	0.07	43.2	-1120.4	-0.07	101.0	-270.8	0.07	43.2	-1120.5	-0.07	100.8	-271.0
H_{10}	0.25	38.8	-1158.9	0.13	90.8	-283.5	-0.12	47.4	-1087.5	-0.23	108.1	-262.6	0.03	44.2	-1112.8	-0.03	99.2	-272.9
H_{20}	0.33	36.6	-1179.9	0.18	88.1	-287.1	-0.14	47.7	-1085.0	-0.19	106.4	-264.5	0.22	39.6	-1152.3	-0.02	98.5	-273.8
H_{30}	0.37	35.5	-1190.9	0.21	86.5	-289.3	-0.09	46.6	-1093.2	-0.16	105.0	-266.0	0.26	38.4	-1163.0	0.10	92.6	-281.2
H_{40}	0.36	35.8	-1187.7	0.22	86.0	-290.0	0.02	44.2	-1112.2	-0.11	102.6	-268.9	0.30	37.4	-1172.7	0.16	89.3	-285.5
H_{50}	0.39	35.1	-1195.3	0.26	83.8	-293.2	0.08	42.9	-1123.6	0.02	96.6	-276.0	0.34	36.2	-1183.5	0.20	87.1	-288.5
H_{60}	0.41	34.5	-1201.6	0.29	82.2	-295.4	0.16	41.0	-1139.6	0.12	91.6	-282.4	0.38	35.3	-1192.6	0.28	82.7	-294.7
H_{70}	0.42	34.2	-1204.5	0.34	79.4	-299.6	0.21	39.7	-1150.5	0.23	85.9	-290.2	0.40	34.5	-1201.1	0.32	80.7	-297.7
H_{80}	0.42	34.0	-1206.0	0.37	77.4	-302.7	0.30	37.3	-1173.0	0.35	78.9	-300.4	0.41	34.2	-1204.1	0.37	77.3	-302.8
H_{90}	0.44	33.6	-1210.4	0.40	75.6	-305.5	0.43	33.9	-1207.7	0.41	74.9	-306.6	0.44	33.6	-1210.5	0.39	75.9	-305.0
H_{100}	0.51	31.3	-1235.8	0.43	73.4	-309.1	0.51	31.3	-1236.5	0.48	70.2	-314.4	0.51	31.3	-1235.8	0.43	73.4	-309.1
H_{mean}	0.39	34.9	-1197.5	0.26	83.9	-293.1	0.10	42.4	-1127.4	-0.22	107.6	-263.1	0.34	36.3	-1183.3	0.16	89.4	-285.4
H_{std}	0.36	35.9	-1187.1	0.40	75.6	-305.5	0.44	33.5	-1212.1	0.46	71.5	-312.2	0.43	33.8	-1208.9	0.45	72.2	-310.9
H_{cv}	-0.10	46.9	-1091.1	-0.16	105.3	-265.8	0.25	38.7	-1160.1	0.23	85.7	-290.4	0.10	42.5	-1126.4	0.05	94.9	-278.2

* The maximum adjusted R^2, and the minimum RMSE and AIC_c were underlined for each column.

Table 3.7. The fitting statistics for the power models that predict stem volume from height metrics

	First canopy returns						*Last canopy returns*						*All canopy returns*					
	Correctly segmented			Mis-segmented			Correctly segmented			Mis-segmented			Correctly segmented			Mis-segmented		
Metric	R_a^2	RMSE (m^3)	AIC_c	R_a^2	RMSE (m^3)	AIC_c	R_a^2	RMSE (m^3)	AIC_c	R_a^2	RMSE (m^3)	AIC_c	R_a^2	RMSE (m^3)	AIC_c	R_a^2	RMSE (m^3)	AIC_c
H_0	-0.15	0.52	-232.8	-0.19	1.23	28.8	0.01	0.48	-259.6	-0.13	1.19	25.6	0.01	0.48	-259.7	-0.13	1.19	25.5
H_{10}	0.27	0.41	-314.3	0.25	0.97	1.2	-0.15	0.51	-233.6	-0.24	1.25	31.3	0.03	0.47	-263.9	0.04	1.10	15.8
H_{20}	0.34	0.39	-331.2	0.31	0.93	-4.0	-0.15	0.52	-232.6	-0.17	1.22	27.9	0.25	0.42	-308.8	0.10	1.06	11.8
H_{30}	0.37	0.38	-341.7	0.37	0.89	-9.1	-0.10	0.51	-240.5	-0.08	1.17	23.3	0.26	0.41	-311.1	0.25	0.97	1.0
H_{40}	0.35	0.39	-336.0	0.37	0.89	-9.2	0.04	0.47	-265.9	-0.03	1.14	20.0	0.28	0.41	-317.5	0.32	0.93	-4.4
H_{50}	0.38	0.38	-343.5	0.41	0.87	-12.8	0.13	0.45	-282.6	0.09	1.07	12.8	0.33	0.39	-328.9	0.35	0.91	-7.4
H_{60}	0.40	0.37	-349.8	0.44	0.84	-16.3	0.20	0.43	-297.0	0.20	1.01	5.4	0.37	0.38	-340.2	0.42	0.86	-14.1
H_{70}	0.41	0.37	-353.2	0.49	0.81	-21.5	0.21	0.43	-300.8	0.32	0.92	-5.1	0.39	0.37	-347.5	0.46	0.82	-18.9
H_{80}	0.41	0.37	-352.6	0.52	0.78	-25.4	0.28	0.41	-317.7	0.46	0.83	-18.3	0.40	0.37	-349.6	0.51	0.78	-25.0
H_{90}	0.42	0.37	-354.1	0.55	0.76	-29.2	0.41	0.37	-352.4	0.53	0.77	-26.5	0.42	0.37	-353.9	0.54	0.76	-28.2
H_{100}	0.54	0.33	-395.4	0.58	0.73	-33.2	0.52	0.33	-390.0	0.60	0.71	-36.1	0.54	0.33	-395.4	0.58	0.73	-33.2
H_{mean}	0.38	0.38	-343.9	0.42	0.86	-14.0	0.06	0.47	-268.6	-0.13	1.20	25.8	0.30	0.40	-321.5	0.33	0.92	-5.2
H_{std}	0.36	0.38	-337.7	0.42	0.86	-14.1	0.44	0.36	-361.3	0.43	0.85	-15.4	0.43	0.36	-358.6	0.45	0.83	-17.7
H_{cv}	-0.12	0.51	-237.4	-0.18	1.22	28.4	0.19	0.43	-295.6	0.17	1.03	7.6	0.05	0.47	-267.7	0.02	1.11	17.3

* The maximum adjusted R^2, and the minimum RMSE and AIC_c were underlined for each column.

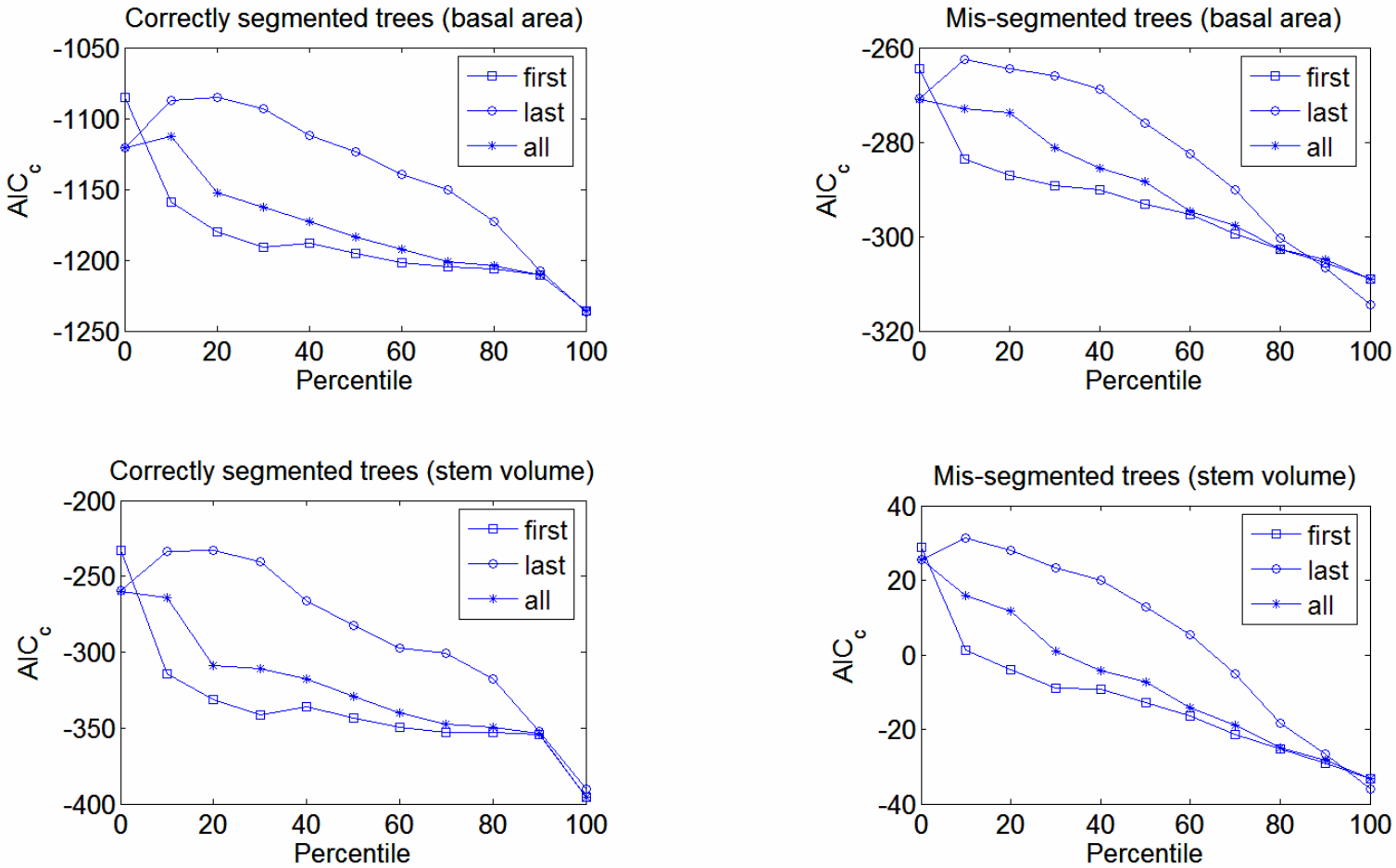

Figure 3.3. The AIC values for models that predict basal area with different percentile height metrics

The low AIC_c values (better performance) at the 0th height percentile (the minimum height) of the last canopy returns can be explained by such a fact: for a larger tree it is more possible that the lowest last canopy return is from the bottom of the tree. If examining the trees with basal area greater than 0.15m, we can find that the minimum height of last returns for a tree is very low and around 1m (Figure 3.4(b)). This pattern leads to a negative relationship. This phenomenon was not observed for the first canopy returns (Figure 3.4(a)). In dense forest, it is possible that all first canopy returns are from the upper portion of a tree and therefore the minimum of their percentile heights is relatively large. It is also possible that the minimum of the percentile heights is small if a pulse hits the lower-portion of a tree, which often happens if a pulse hits the side of a large isolated tree. Therefore, there is no much association between the basal area and the minimum height of the first canopy returns. Overall, the minimum heights of both first and last canopy returns were poor predictors for basal area. At most percentiles, the percentile height of the first canopy returns has better performance than that of last canopy returns. However, when the percentile increases to 100, their performance becomes close or identical. Since the maximum height is the best percentile height metric, it seems that dividing the canopy returns into first and last returns has little effects on improving model fitting.

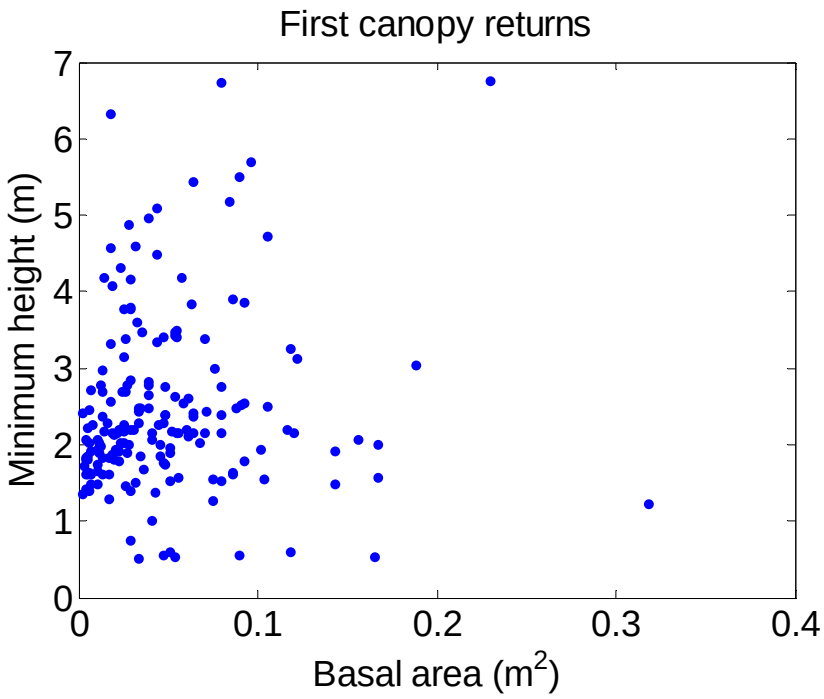

(a)

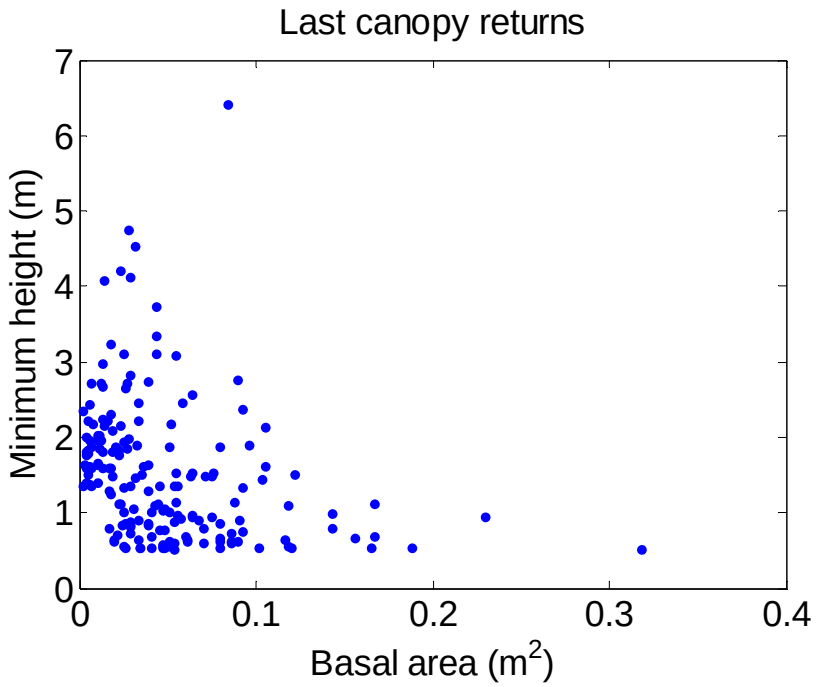

(b)

Figure 3.4. The relationship between basal area and minimum height for first and last canopy returns.

4.2 Crown area

Overall, the crown area is a better predictor than the height metrics for both basal area

and stem volume in the power models. For example, the adjusted R^2 for a power model of the crown area C_d is about 0.2 higher than that for a power model of the maximum height H_{max} for predicting basal area. Although crown area is a powerful metric, only a few studies have used it in the estimation of the canopy structure parameters (Hyyppä *et al.*, 2001; Persson *et al.*, 2002; Popescu *et al.*, 2004; Maltamo *et al.*, 2004b; Roberts *et al.*, 2005), mainly due to the difficulty in extracting this metric.

As in Models B.6 and V.5, many studies used crown area or diameter and tree height to predict the diameter at breast height (DBH), based on which other canopy structure parameters were predicted. Hyyppä *et al.* (2001) is the first to extract crown diameter from LIDAR data for forest studies. They used a segmentation-based method to extract crown diameter and applied it to the stand-level stem volume estimation of a boreal forest in Finland. They first fitted a linear regression model that depends on crown diameter and tree height to predict the diameter at breast height (DBH), based on which stem volume was calculated. When evaluating the accuracy at the stand level, they found that the stand errors for mean height, basal area, and stem volume are 1.8m, 2.0m^2/ha, and 18.5m^3/ha, respectively. The precision is better than that in conventional standwise forest inventory. Maltamo *et al.* (2004b) fitted such a linear regression model at the logarithmic scale and found that the RMSE for the estimates of timber volume are 22.5% in the same study site. Persson *et al.* (2002) applied the product of tree height and crown diameter derived from LIDAR to a simple linear regression model for predicting DBH. With the predicted DBH, the stem volume was

estimated for a boreal forest with dominant species of Norway spruce, Scots pine and birch. They found that 91 percent of the total stem volume was detected. Popescu *et al.* (2004) tested stepwise regression models that depended on the statistics of individual tree height and crown diameter to predict plot-level biomass. They found that the crown diameter parameters are significant variables in the stepwise regression models. Roberts *et al.* (2005) is the first to extract individual tree leaf area from LIDAR data. At a 16-year-old loblolly pine spacing trial in Mississippi, they found that LIDAR-derived estimates of leaf area based on height and crown diameter were on average within $0.1m^2$ of ground-based estimates for trees on plots initially planned at 1.5m×1.5m spacing.

When testing the above methods over our study site, we found that Models B.6 and V.5, which are based on Hyyppä *et al.* (2001)'s method, achieved the best results. For clarity, only the statistics for Hyyppä *et al.* (2001)'s method are shown in Tables 4 and 5. Compared to the power models of either tree height or crown area, the models depending on both tree height and crown area (Models B.6 and V.5) can achieve much better performance for correctly segmented trees. This implies that crown area and tree height are complementary to each other for estimating basal area and stem volume since they characterize the canopy structure information in the horizontal and vertical dimensions, respectively (Hyyppä *et al.*, 2001, Holmgren *et al.*, 2003; Hall *et al.*, 2005).

4.3 Canopy geometric volume

In the power models (Models B.1-3 and V.1-3), the canopy geometric volume G is a much better predictor than the tree height or crown area for predicting both the basal area and stem volume. The result confirms our hypothesis that canopy geometric volume can obtain better performance since it can characterize canopy structure in a three-dimensional space. Especially, the theoretical models based on the plant allometry (Models B.5 and V.4) have the lowest AIC_c values among all univariate models. These models are attractive in several aspects: first, it has a theoretical basis in plant allometry; second, it has only one parameter; and third, the parameter is easy to interpret. In particular, for the stem volume model, the coefficient β_1 can be interpreted as the stem volume density, similar as the leaf area volume density for predicting leaf area. Note that Model B.5 will overestimate the basal area in the case of over-segmentation of tree crowns and underestimate it in the case of under-segmentation; however, the estimation of stem volume with Model V.4 is not affected by over-segmentation or under-segmentation theoretically. The 3/4 and 1 exponents in Models B.5 and V.4 can also be confirmed to some extent by analyzing the confidence intervals of the exponents in Model B.3 and V.3. The 95% confidence interval of the exponent in Model B.3 is (0.67, 0.80), which includes the exponent 3/4. Likewise, the 95% confidence interval of the exponent in Model V.3 is (0.93, 1.09), which includes the exponent 1. As expected, the simple linear model with no intercept for predicting basal area (Model B.4) has much worse performance than the Model B.5 since the analysis based on the plant allometry show that basal area is

proportional to $G^{3/4}$ instead of G.

Lefsky *et al.* (1999) proposed a canopy volume method (CVM) to describe the three-dimensional canopy structure and applied it to predict the total forest biomass for Douglas-fir/western hemlock forests in western Oregon. Their method is the first to take advantage of the ability of a waveform-recording sensor (SLICER) to directly measure the three-dimensional distribution of canopy structure (Lefsky *et al.*, 2002b). However, the canopy volume derived from their method is different from the one in this study. Lefsky *et al.* (1999) first derived the canopy height profile from the returned waveform within a footprint and then divided the canopy within that footprint into four parts (closes gap, oligophotic zone, euphotic zone, and open space) and summed up the height of the euphotic and oligophotic zones to get the total volume of "filled" canopy (Figure 3.5). The problem with their method is that it cannot accurately describe the canopy structure variability in the horizontal plane within the footprint. Figure 3.5 shows the waveforms and their cumulative power profiles within two footprints. There are two trees within footprint (a) and only one tree within (b). However, the total volume of "fill" canopy, which is the sum of the euphotic zone and oligophotic zone height, is the same for the two waveforms even though the total geometric canopy volumes of trees within these two footprints are different. Therefore, their method can indicate whether there is canopy along the vertical direction (Lefsky *et al.*, 1999) but cannot completely describe the canopy structure information in a three-dimensional space.

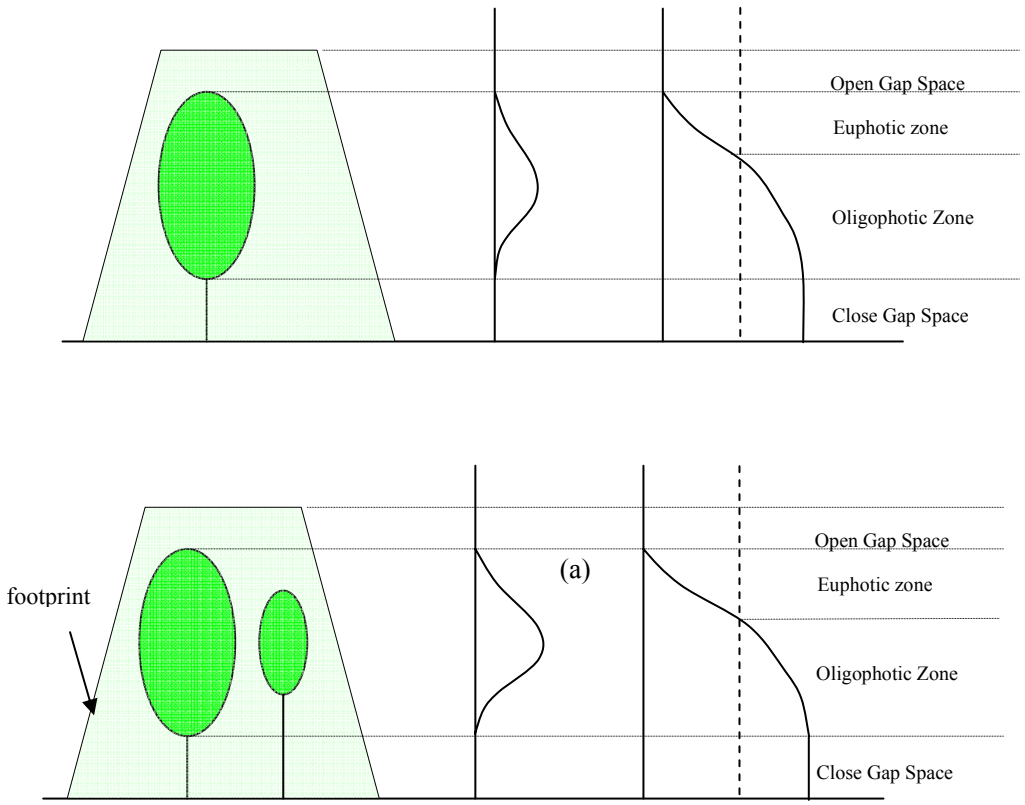

Figure 3.5. Illustration of the canopy volume method by Lefsky et al. (1999) (adapted from Figure 2 in Lefsky *et al.*, 1999)

4.4 Comparison

(b)

The research on applying the *individual-tree integration* method in forest studies is still in its infancy. Most studies that extracted the individual tree dimensional information have been using the *hybrid-regression* method (e.g., Hyyppä *et al.*, 2001; Popescu *et al.*, 2003; Maltamo *et al.*, 2004b) and therefore their accuracy assessment is typically performed at the plot level (Riaño *et al.*, 2004). There are only a few studies (Persson *et al.*, 2002; Næsset and Økland, 2002; Riaño *et al.*, 2004; Roberts *et al.*, 2005) that evaluated the accuracy of canopy structure estimation at the individual tree level. Persson *et al.* (2002) used the product of tree height and crown diameter to predict DBH, and then calculate stem volume using allometric equations. They

obtained a R^2 value of 0.83 and 0.88 for DBH and stem volume estimation, respectively, for a sample of 135 trees. Næsset and Økland (2002) used a stepwise regression model for predicting tree height and crown length properties, but not basal area and stem volume. Riaño *et al.* (2004) evaluated the accuracy of estimating crown bulk density for Pinus sylvestris in a naturally regenerated and planted Scots pine forest in Spain and obtained a coefficient of determination of 0.l4. Roberts *et al.* (2005) predicted the leaf area index with tree height and crown size for individual trees in loblolly pine plantations. For trees on plots originally planted at square spacings of 2.4 m and 3.0 m, they reported an underestimate of 5.8m^2 and 14.5m^2, respectively and attributed the errors to the inability of generating accurate LIDAR-based estimates of crown dimensions. The low accuracy reported in Riaño *et al.* (2004) and Roberts *et al.* (2005) has revealed the difficulty of estimating individual-tree canopy structural information with the previous methods. The accuracy in Persson *et al.*'s study was relatively high. However, when their method was applied to our study site, the adjusted R^2 are 0.70 and 0.62 for basal area and stem volume estimation, respectively. Their study site is in a conifer forest, which could be a factor for their better model fit. Our theoretical models based on canopy geometric volume G can obtain a much higher adjusted R^2 of 0.77 and 0.79 for basal area and stem volume estimation, respectively. This proves to some extent the usefulness of the canopy geometric volume G and the associated theoretical models for estimating basal area and stem volume.

Among all models for basal area estimation, overall the theoretical model B.5 should

be recommended for use because 1) for the correctly-segmented trees it is among the top three models, and 2) for mis-segmented trees it is the best model and much better than others. For stem volume estimation, the stepwise regression model V.6 is the best. However, the theoretical model V.4 should be recommended for use due to a number of considerations: 1) its close performance to the best models, 2) the model parsimony (Burnham and Anderson, 2002), and 3) the model produced from a stepwise regression is usually site-specific.

5 Conclusions

This study proposed a new LIDAR metric called canopy geometric volume G for estimating basal area and stem volume of individual trees. Based on the plant allometry, it was found that basal area is proportional to the 3/4 power of G and stem volume is directly proportional to G. When tested over trees that were mis-segmented, the theoretical models based on these relationships have the best performance for basal area estimation and the second to best performance for stem volume estimation. Overall, we think these theoretical models have the best performance and should be recommended for basal area and stem volume estimation.

The major limitation of this research is that only one species was considered. If the linear model with no intercept (Model V.4) is used for stem volume estimation, the coefficient β_1 in the model, which is interpreted as the stem volume density, could differ for different species. It is unknown whether such a model has a better performance than other models over sites with multiple species. It is hypothesized that

Model V.4 can still be used since the coefficient could be understood as the effective stem volume density for all species in an area. For example, the coefficient could be defined for boreal, temperate, tropic forests, etc. if an approximate estimation of stem volume is required at a large scale. Such a hypothesis needs to be tested in future studies. It is also possible to fuse LIDAR data with species information derived from optical imagery to estimate canopy structural parameters for each species separately.

References

Anderson-Sprecher, R. 1994. Model comparisons and R^2. *The American Statistician*, 48, 113-117.

Baldocchi, D.D., L. Xu,, and N. Kiang, 2004. How plant functional-type, weather, seasonal drought, and soil physical properties alter water and energy fluxes of an oak-grass savanna and an annual grassland. *Agricultural and Forest Meteorology*, 123, 13-39.

Birdsey, R.A., and G.M. Lewis, 2002. *Carbon in United States Forests and Wood Products, 1987-1997*. Newtown Square, PA: USDA Forest Service.

Brandtberg, T., T. Warner, R. Landenberger, and J.B. McGraw, 2003. Detection and analysis of individual leaf-off tree crowns in small footprint, high sampling density lidar data from eastern deciduous forest in North America. *Remote Sensing of Environment*, 85, 290-303.

Burnham, K.P., and D.R. Anderson, 2002. *Model Selection and Multimodel Inference:*

a Practical Information-theoretic Approach. 2nd Edition. New York: Springer-Verlag Press.

Chen, Q., P. Gong, D.D. Baldocchi, and G. Xie, in press. Filtering airborne laser scanning data with morphological methods. *Photogrammetric Engineering and Remote Sensing*.

Chen, Q., D.D. Baldocchi, P. Gong, and M. Kelly, 2006. Isolating individual trees in a savanna woodland using small footprint LIDAR data. *Photogrammetric Engineering and Remote Sensing*, forthcoming.

Enquist, B.J., 2002. Universal scaling in tree and vascular plant allometry: Toward a general quantitative theory linking plant form and function from cells to ecosystems. *Tree Physiology*, 22, 1045–1064.

Hall, S.A., I.C. Burke, D.O. Box, M.R. Kaufmann, and J.M. Stoker, 2005. Estimating stand structure using discrete-return lidar: an example from low density, fire prone ponderosa pine forests. *Forest Ecology and Management,* 208, 189–209.

Holmgren, J., M. Nilsson, and H. Olsson, 2003. Estimation of tree height and stem volume on plots using airborne laser scanning. *Forest Science*, 49, 419-428.

Hyyppä, J., O., Kelle, M., Lehikoinen, and M. Inkinen, 2001. A segmentation-based method to retrieve stem volume estimates from 3-D tree height models produced by laser scanners. *IEEE Transactions on Geoscience and Remote Sensing*, 39, 969-975.

Kvålseth, T.O. 1985. Cautionary note about R^2. *American Statistician*, 39, 279-285.

Leckie, D., F. Gougeon, D. Hill, R. Quinn, L. Armstrong, and R. Shreenan, 2003. Combined high-density lidar and multispectral imagery for individual tree crown

analysis. *Canadian Journal of Remote Sensing*, 29, 1-17.

Lefsky, M., W. Cohen, A. Acker, G. Parker, T. Spies, and D. Harding, 1999. Lidar Remote Sensing of the Canopy Structure and Biophysical Properties of Douglas-Fir Western Hemlock Forests. *Remote Sensing of Environment*, 70, 339-361.

Lefsky, M.A., W.B. Cohen, G.G. Parker, and D.J. Harding, 2002a. Lidar remote sensing of above-ground biomass in three biomes. *Global Ecology and Biogeography*, 11, 393-399.

Lefsky, M.A., W.B. Cohen, G.G. Parker and D.J. Harding. 2002b. Lidar remote sensing for ecosystem studies. *Bioscience*, 52, 19-30.

Lim, K., P. Treitz, K. Baldwin, I. Morrison, and J. Green, 2003. Lidar remote sensing of biophysical properties of tolerant northern hardwood forests. *Canadian Journal of Remote Sensing*, 29, 658-678.

Maltamo, M., K., Mustonen, J. Hyyppä, J. Pitkänen, and X. Yu, 2004a. The accuracy of estimating individual tree variables with airborne laser scanning in a boreal nature reserve. *Canadian Journal of Forest Research*, 34, 1791-1801.

Maltamo, M., K., Eerikäinen, J. Pitkänen J. Hyyppä, and M. Vehmas, 2004b. Estimation of timber volume and stem density based on scanning laser altimetry and expected tree size distribution functions. *Remote Sensing of Environment*, 90, 319-330.

Means, J., S. Acker, B. Fitt, M. Renslow, L. Emerson, and C. Hendrix, 2000. Predicting forest stand characteristics with airborne scanning lidar. *Photogrammetric Engineering and Remote Sensing*, 66, 1367-1371.

Medlyn, B. E., 2003. A MAESTRO Retrospective. *Forests at the Land-Atmosphere Interface* (M. Mencuccini, J. Moncrieff, K. McNaughton and J. Grace, editors). CABI Publishing.

Morsdorf F., E. Meier, B. Kötz, K. I. Itten, M. Dobbertin, and B. Allgöwer, 2004. LIDAR-based geometric reconstruction of boreal type forest stands at single tree level for forest and wildland fire management. *Remote Sensing of Environment*, 3(92):353-362.

Næsset, E. 2004. Practical Large-scale Forest Stand Inventory Using a Small-footprint Airborne Scanning Laser. *Scandinavian Journal of Forest Research*, 19, 164-179.

Næsset, E., T. Gobakken, J. Holmgren, H. Hyyppä, J. Hyyppä, M. Maltamo, M. Nilsson, H. Olsson, Å. Persson, and U. Söderman, 2004. Laser scanning of forest resources: the Nordic experience. *Scand. J. For. Res.*, 19, 482-499.

Næsset, E., and T. Økland, 2002. Estimating tree height and crown properties using airborne scanning laser in a boreal nature reserve. *Remote Sensing of Environment*, 79, 105-115.

Norberg, A., 1988. Theory of growth geometry of plants and self-thinning of plant populations: geometry similarity, elastic similarity, and different growth modes of plants parts. *American Naturalist*, 131, 220-256.

Persson, Å, J. Holmgren, and U. Söderman, 2002. Detecting and measuring individual trees using an airborne laser scanner. *Photogrammetric Engineering and Remote Sensing*, 68, 925-932.

Pillsbury, N.H., and M.L. Kirkley, 1984. *Equations for Total, Wood, and Saw-Log*

Volume for Thirteen California Hardwoods. Research Note PNW-414. Portland, OR: U.S. Department of Agriculture, Forest Service, Pacific Northwest Forest and Range Experiment Station.

Popescu, S.C., R.H. Wynne, and R.F. Nelson, 2003. Measuring individual tree crown diameter with lidar and assessing its influence on estimating forest volume and biomass. *Canadian Journal of Remote Sensing*, 29, 564-577.

Popescu, S.C., and R.H. Wynne, 2004. Seeing the trees in the forest: using lidar and multispectral data fusion with local filtering and variable window size for estimating tree height. *Photogrammetric Engineering and Remote Sensing*, 70, 589–604.

Popescu , S.C. , R.H. Wynne and J.A. Scrivani, 2004. Fusion of small-footprint lidar and multispectral data to estimate plot-level volume and biomass in deciduous and pine forests in Virginia, U.S.A. *Forest Science*, 50, 551-565

Riaño, D., E. Chuvieco, S. Condis, J. Gonzalez-Matesanz, and S.L. Ustin, 2004. Generation of crown bulk density for Pinus sylvestris L. from lidar. *Remote Sensing of Environment* 923: 345-352.

Roberts, S.D., T.J. Dean, D.L. Evans, J.W. McCombs, R.L. Harrington, P.A. Glass, 2005. Estimating individual tree leaf area in loblolly pine plantations using LiDAR-derived measurements of height and crown dimensions. *Forest Ecology and Management*, 213, 54-70.

West, G.B., J.H. Brown, and B.J. Enquist, 1999. A general model for the structure and allometry of plant vascular systems. *Nature*, 400, 664–667.

Chapter 4 Modeling Radiation and Photosynthesis of Heterogeneous Landscapes with a Markov Big-Leaf Model

Abstract

How to model radiation and ecological processes realistically for heterogeneous landscapes with simple models has been a pressing but challenging research question for decades. We proposed an analytical approach to calculate clumping factors for heterogeneous landscapes and used it in Markov big-leaf models to estimate radiation and photosynthesis. The clumping factor is dependent on i) tree spacing vs. crown width ratio, ii) crown depth vs. crown width ratio, iii) leaf area volume density in m^2/m^3, iv) G-function, and v) solar zenith angle. In a savanna woodland in California, we explore how the parameterization of canopy geometry will affect simulation of radiation and photosynthesis by comparing three different scenarios: 1) the individual tree location and structural information are spatially-explicitly specified, 2) the whole canopy is simplified as a box within which the leaf are randomly distributed so that the model looks like a big-leaf model, and 3) the canopy is simplified as a box but within it the leaves are clumped so that the model resembles a Markov big-leaf model. It was found that the Markov big-leaf model can achieve much better performance than the simple big-leaf model; incorporating the clumping factor in the big-leaf model can reduce the percent error of CO_2 assimilation estimation from around 50% to 10% when local leaf area index is 4.5 m^2/m^2. The results indicate that our approach of calculating clumping factors has tremendous applications in terrestrial ecosystem modeling.

1 Introduction

Savannas, inhabited by one-fifth of the world's population, are one of the world's major terrestrial biomes (Ramankutty and Foley, 1999). Since savannas are anticipated to be among the ecosystems that are most sensitive to future land use and climate changes (Bond et al., 2003, Sankaran et al., 2005), it is important to gain a mechanistic understanding of vegetation-atmosphere exchange with processed-based ecological models. However, modeling savanna ecosystems is very challenging because savannas, typically characterized with sparsely distributed individual trees or clumps, are both horizontally and vertically heterogeneous.

Since radiation is the driver of various ecological processes, one of the major challenges is to model the radiation realistically for such heterogeneous landscapes. A three-dimensional individual-tree based model can be used to characterize the canopy morphology details as much as possible (Charles-Edwards and Thorpe, 1976; Allen, 1974). However, at broad spatial scales simpler models such as big-leaf models, which simplify the canopy as a box, are highly preferred because of the computation and parameterization concerns. If the canopy is simplified as a box, it is essential to know that, first, when compared to an individual-tree based model what are the errors of radiation modeling due to the simplification of canopies? and, second, how to improve the big-leaf models so that they can achieve comparable performance to individual-tree models?

For the first question, previous studies have found the big-leaf model will generally overestimate the intercepted radiation for heterogeneous canopies (Asrar et al., 1992; Jarvis & Leverenz, 1983; Norman and Wells, 1983; Andrieu and Sinoquet, 1993). Asrar et al. (1992) simulated canopies with different leaf area index and canopy cover within a plot of 50 by 50 m^2 and compared the 1D and 3D models. They found that the 1D approach results in an overestimation of both canopy reflectivity and PAR absorptivity as compared to a 3D calculation. The discrepancy is especially greater at lower canopy leaf area indices (ca. 1-3) and generally decreases with increasing leaf area. Their analysis indicated that the leaf area index of a canopy is less of an instructive parameter than ground cover and clump leaf area index for these canopies. Norman and Wells (1983) tested a three-dimensional general array model in a crop canopy in Ontario, Canada and compared it with a big-leaf model. They found that at a leaf are index of four, the general ellipsoidal array model predicts the same direct beam PAR intercepted as the random model on a daily basis. However at leaf area indices of 0.5, 1.0, and 2.0 the random model overestimates daily intercepted PAR by 25, 17, and 7%, respectively. Another finding is that the sunfleck fraction is most affected by clumping foliage at intermediate leaf area indexes when adjacent rows are just beginning to approach closure. Andrieu and Sinoquet (1993) compared a two-dimensional model (one dimension in vertical direction, the other is one horizontal direction) and a big-leaf model in predicting the gap fraction of an artificial row canopy. It was found that the big-leaf model significantly underestimated the gap fraction and overestimated the light interception.

As a remedy, researchers have attempted to incorporate a clumping factor in the big-leaf model so that it can produce the same light penetration probability or interception probability as the individual-tree model:

$$P = \exp(-k\Omega L) \tag{1}$$

$$I = 1 - \exp(-k\Omega L) \tag{2}$$

where L is the leaf area index, k is the extinction coefficient, and Ω is the clumping factor. Such a model can be called a Markov big-leaf model. Norman and Wells (1983) derived the clumping factor by assuming that the Markov model can intercept the same amount of radiation as the individual-tree model. They found that the clumping factor varied with zenith angle and leaf area index. Andrieu and Sinoquet (1993) derived the clumping factor with a similar approach, however, using the constraint of the same gap fraction. It was also found that the clumping factor depends on zenith angle. Kucharik et al. (1999) calculated clumping factors based on Monte Carlo simulation, but their method is still heuristic and semi-empirical. Despite of these efforts, there are still no fully mechanistic (instead of empirical or heuristic) approaches for calculating clumping factor.

Note that if a Markov model can produce the same gap fraction or interception probability as an individual-tree based model, it also implies that it can produce the same sunlit leaf area index LAI_{sunlit}, which is evident in the equation of calculating LAI_{sunlit}:

$$\mathrm{LAI}_{\mathrm{sunlit}} = \frac{1-\exp(-k\Omega L)}{k} \quad (3).$$

In this study, we present an analytical approach to derive clumping factors for heterogeneous canopies based on the constraint that it can produce the same sunlit leaf area index. We use sunlit leaf area index as a constraint because it can help our derivation to intuitively link to physical meanings. In our approach, the clumping factor is dependent on i) tree spacing vs. crown width ratio, ii) crown depth vs. crown width ratio, iii) leaf area volume density in m^2/m^3, iv) G-function, and v) solar zenith angle.

To test this approach, we use a three-dimensional biogeochemistry model called MAESTRA to construct the canopy of a savanna woodland in California with three different ways: 1) the individual-tree shapes and locations are explicitly specified; within the individual-tree envelopes, leaves are randomly distributed, 2) the canopy is simplified as a box within which leaves are randomly distributed so the model resembles a big-leaf model, and 3) the canopy is simplified as a box within which leaves are clumped so the model looks like a Markov big-leaf model. We will explore how the gross primary productivity (GPP) will be modeled differently. The modeled GPP is also validated with the eddy covariance tower measurements.

2 An analytical approach for calculating clumping factors

To facilitate the calculation of sunlit leaf area index, the landscape is simplified as a mosaic of bare ground and trees, where the trees are regularly distributed (Figure

4.1(a)). All trees have the same size and box shapes. For the convenience of derivation, we normalized all of the dimensional variables with crown width so the value of crown width is 1. The crown height to width ratio and tree spacing to crown width ratio are denoted as *h* and *l*, respectively (Figure 4.1(b)). For simplicity, they are referred as crown height and tree spacing hereinafter.

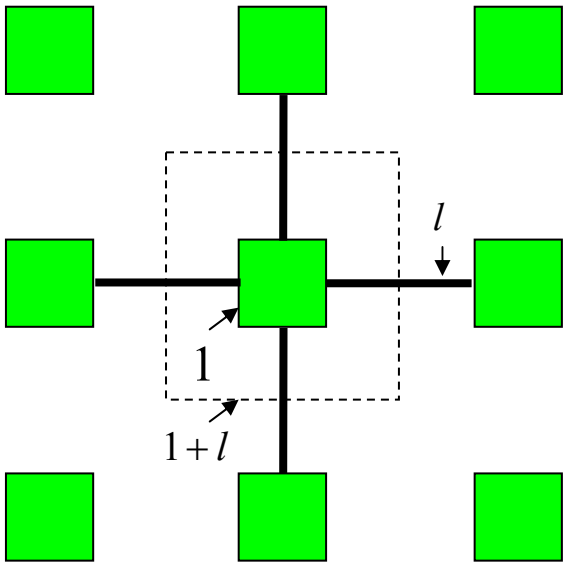

(a)

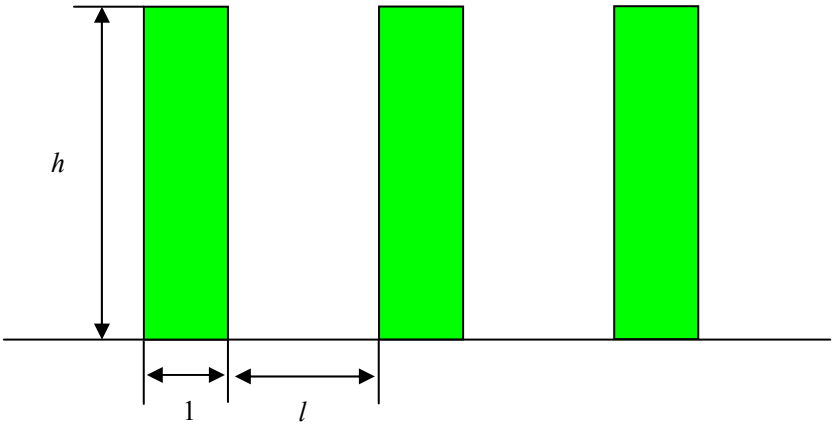

(b)

Figure 4.1. The configuration of a heterogeneous landscape

For any elementary volume *dv=dxdydz* within the crown, the sunlit leaf area, SLA, can be calculated by:

$$\mathrm{SLA_{dV}} = \rho * P_{sunlit}(x, y, z) dxdydz \tag{5}$$

where ρ is the leaf area volume density in m^2/m^3, which is assumed to be constant over the canopy, $P_{sunlit}(x, y, z)$ is the sunlit leaf area probability within the elementary volume, which can be written as:

$$P_{sunlit}(x, y, z) = \exp(-\rho G(\theta) s_{x,y,z}), \tag{6}$$

where $s_{x,y,z}$ is the within-canopy distance of light penetrating to the point (x,y,z). The sunlit leaf area of the tree, denoted as SLA_{tree}, can be calculated by integrating Equation (5) over the tree volume V.

$$\begin{aligned} SLA_{tree} &= \oiiint_{v \in V} \rho * P_{sunlit} dv = \oiiint_{v \in V} \rho * \exp(-\rho G(\theta) s_{x,y,z}) dv \\ &= \rho * \oiiint_{v \in V} \exp(-\rho G(\theta) s_{x,y,z}) dv \end{aligned} \tag{7}$$

For simplicity, let us assume that sunlight is parallel to one side of the box. We also define a coordinate system as follows: the origin is the upper corner that is closer to the sun, the x-axis is parallel to the sunlight and positive along the sunlight direction, y-axis is perpendicular to the sunlight, and z-axis is positive downward (Figure 4.2). Then, we know

$$SLA_{tree} = \rho * \int_{x=0}^{1} \int_{y=0}^{1} \int_{z=z_b^i}^{z_t^i} \exp(-\rho G(\theta) s_{x,y,z}) dxdydz$$
$$= \rho * \int_{x=0}^{1} \int_{z=z_b^i}^{z_t^i} \exp(-\rho G(\theta) s_{x,z}) dxdz \quad (8)$$

where z_t^i and z_b^i are the top and bottom limits along the z direction, respectively.

To calculate SLA_{tree}, we need to know $s_{x,z}$, which can be explicitly expressed if we break the tree volume V into subvolumes V_1, V_2, …, V_n as shown in Figure 4.2. For example, for V_1 in Figure 4.2, *s* is z/cos*θ*, for V_2, *s* is x/sin*θ*. More generally,

$$s_{x,z}^i = \begin{cases} \dfrac{z}{\cos\theta} - \dfrac{(i-1)*l}{2\sin\theta}, & \text{when i is odd} \\ \dfrac{x}{\sin\theta} + \dfrac{i-2}{2\sin\theta}, & \text{when i is even} \end{cases} \quad (9)$$

where *i* is the index of subvolume.

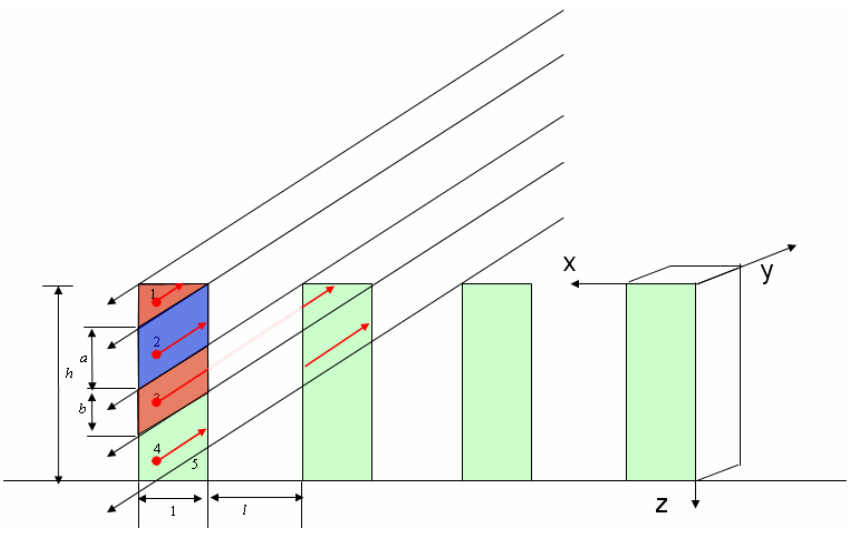

Figure 4.2 Calculation of sunlit leaf area index for heterogeneous landscapes. The red lines represent $s_{x,y,z}$, the within-canopy distance of light penetrating to the point (x,y,z).

Also, z_t^i and z_b^i are expressed as follows:

$$z_t^i = \begin{cases} 0, & \text{when i =1} \\ \min(\frac{x}{\sin\theta} + \frac{i-1}{2}a + \frac{i-3}{2}b, h), & \text{when i is odd and i>= 3} \\ \min(\frac{x}{\sin\theta} + \frac{i-2}{2}a + \frac{i-2}{2}b, h), & \text{when i is even} \end{cases} \quad (10)$$

$$z_b^i = \begin{cases} \min(\frac{x}{\sin\theta} + \frac{i-1}{2}a + \frac{i-1}{2}b, h), & \text{when i is odd} \\ \min(\frac{x}{\sin\theta} + \frac{i}{2}a + \frac{i-2}{2}b, h), & \text{when i is even} \end{cases} \quad (11)$$

where $a = l\cot\theta$, $b = \cot\theta$.

So, the sunlit leaf area for the tree can be obtained by integrating the sunlit leaf area for each subvolume separately and then summing them up:

$$SLA_{tree} = \rho * \sum_{i=1}^{n} \int_{x=0}^{1} \int_{z=z_b^i}^{z_t^i} \exp(-\rho G(\theta) s_{x,z}^i) dxdz \quad (12)$$

After the sunlit leaf area for individual trees is calculated according to Equation (12), as shown in Figure 4.1(a) the sunlit leaf area index over the landscape can be calculated as:

$$\text{LAI}_{\text{sunlit}} = \frac{SLA_{tree}}{(1+l)^2} \quad (13).$$

The total leaf area index L is:

$$L = \frac{\rho * h}{(1+l)^2} \quad (14)$$

Substitute Equations (13) and (14) to (3), and we can calculate the clumping factor.

3 The three-dimensional biogeochemistry model - MAESTRA

In the past three decades, a number of spatially-explicit 3D models have been developed to simulate radiation and ecological processes for heterogeneous canopies including crops (Allen, 1974), orchards (Charles-Edwards and Thorpe, 1976), and forests (Asrar et al., 1992; Kucharik et al., 1999; Mariscal et al., 2004). In this study, an individual-tree based model called MAESTRA (Medlyn, 2004) is used.

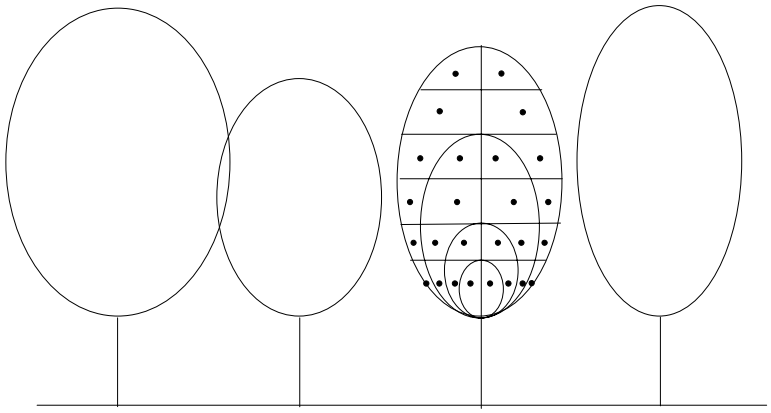

Figure 4.3 Representation of the canopy in MAESTRA. Positions and dimensions of each crown are specified. Grid volumes within the target crown are used for crown photosynthesis calculations. (From Medlyn, 2004)

MAESTRA is a model updated and renamed from MAESTRO (Wang and Jarvis, 1990). MAESTRA incorporates the three-dimensional radiative transfer model of Norman and Welles (1983) for direct light transfer and the methods of Norman and Jarvis (1975) and Norman (1979) for diffuse light transfer. The most distinguishing feature of MAESTRA is its flexibility of representing canopy with diverse types of

discrete geometric envelopes (like cone, box, ellipsoid, etc) (Figure 4.3), which makes it ideal to explore the interactions between canopy structure and canopy processes in our study.

In MAESTRA, the net CO_2 assimilation rate A_n is calculated using Farquhar's model (Farquhar et al., 1980; Farquhar & Wong, 1984):

$$A_n = min\{A_v, A_j\} - R_d, \tag{15}$$

$$A_v = V_{c\max} \frac{c_i - \Gamma^*}{c_i + K_c(1 + o_i / K_o)}, \tag{16}$$

$$A_j = \frac{J}{4} \frac{c_i - \Gamma^*}{c_i + 2\Gamma^*}, \tag{17}$$

where A_v and A_j are the assimilation rate limited by Rubisco activity and electron transport (ribulose-1,5-bisphosphate, RuBP, regeneration), respectively, and R_d is the day respiration (mitochondrial respiration under illumination condition), which is the respiration from processes other than photorespiration, V_{cmax} is the maximum catalytic activity of Rubisco in the presence of saturating levels of RuBP and CO_2, c_i and o_i are the CO_2 and oxygen concentrations in the intercellular space, respectively, Γ^* is the CO_2 compensation point in the absence of day respiration and is equal to $0.5o_i / \tau$ (τ is the Rubisco specificity factor); K_c and K_o are Michaelis coefficients for CO_2 and O_2, respectively, and J is the potential rate of electron transport for a given incident photosynthetically active photon flux density I.

We calculate the potential rate of electron transport J using the following equation:

$$J = \frac{\alpha I}{\sqrt{1 + (\frac{\alpha I}{J_{\max}})^2}}, \tag{18}$$

where J_{max} is the maximum potential rate of electron transport, α is the quantum yield (mol electron per mol photon).

The Ball-Berry stomatal conductance model (Ball et al., 1987) is combined with the photosynthesis model and leaf energy balance model to solve the net assimilation, stomatal conductance, and intercellular CO_2 mol fraction c_i, iteratively.

$$g_{sc} = a_0 + \frac{a_1 A_n h_s}{c_s} \tag{19}$$

$$A_n = g_{sc}(c_s - c_i) = g_{bc}(c_a - c_s), \tag{20}$$

where g_{sc} and g_{bc} are the stomatal and boundary layer conductances for CO_2, c_s and c_a are the CO_2 concentrations at the leaf surface and in the free air, respectively, h_s is the relative humidity at the leaf surface, a_0 and a_1 are the empirical constants.

4 Modeling radiation and photosynthesis of a savanna ecosystem

4.1 Study site

The study site is an open oak savanna woodland, located near Ione, California (latitude: 38.26'N, longitude: 120.57'W). The site is also part of the AmeriFlux network of eddy covariance field sites. The landscape is characterized by flat terrain

(with a maximum slope of less than 15%) with a scattered, clumped distribution of blue oaks (*Quercus douglasii*) and a minority of grey pines (*Pinus sabiniana*) over a continuous layer of Mediterranean annual grasses. The mean annual air temperature of the region is 16.6°C. The mean annual precipitation is about 559mm per year (based on the data from the cooperative weather station in Ione, CA that operated between 1959 and 1977). Due to the Mediterranean climate of the region, rainfall is concentrated between October and next May; essentially no rain occurs during the summer months. The soil is classified as an Auburn very rocky silt loam (lithic haploxerepts). It contains 43% sand, 43% silt, and 13% clay. Its bulk density at surface layer (0–30 cm) is around 1.61 ± 0.10 g cm^3 (n = 54) (Baldocchi *et al.,* 2004).

4.2 Model parameterization

4.2.1 Canopy structure

Table 4.1. Canopy attributes for an area of 200m by 200m around the tower

Variable	Value (unit)
Tree number	576
Tree height	9.0 ± 2.7 (m)
Trunk height	1.9 ± 1.2 (m)
DBH	26 ± 11(cm)
Crown radius	2.9 ± 1.4 (m)
Leaf area index	0.43 (m^2/m^2)
Canopy cover	0.47

* The values after the sign ± are the standard deviation.

Our study area is 200m by 200m around the eddy covariance tower. We used airborne lidar data to map the individual-tree locations, delineate their boundaries, and extract the individual-tree structural information such as basal area, biomass, and leaf area (Chen et al., 2006; Chen, 2007; Chen et al., 2007). The canopy structure attributes

derived from lidar data are summarized in Table 4.1.

As introduced earlier, we construct the canopy with three different settings: 1) The tree height, crown radius, trunk height, and leaf area for all trees within 200m by 200m are specified with the information derived from lidar data. All trees are assumed to have ellipsoidal shapes and leaves are assumed to be randomly distributed within individual crowns, 2) the canopy is simplified as a 200m by 200m box. The mean tree height and trunk height are used to specify the dimensions of the box. The leaf area of the box is the total leaf area over the study area. Leaves are randomly distributed within the box, and 3) the same as 2), except that the leaves are clumped and the clumping factor is calculated with our approach. We will refer the models with these three different canopy structures as individual-tree model, big-leaf model, and Markov big-leaf model, respectively. To avoid the edge effects, we replicate the canopy for 9 times and arrange them as a 3 by 3 grid so that the landscape is 600m by 600m. The simulation is only performed for 200m by 200m in the middle of the landscape.

4.2.2 Photosynthesis, respiration, and stomatal conductance

The photosynthetic capacity V_{cmax}, maximum rate of electron transport J_{max}, and day respiration R_d of blue oak leaves were measured by Xu and Baldocchi (2003). They conducted gas exchange measurements of CO_2 and light response curves on blue oak leaves biweekly throughout the growing season with a portable photosynthesis system (LI-6400, Li-Cor, Lincoln, NE). It was found that there are pronounced seasonal

patterns of V_{cmax}, J_{max}, and R_d; however, the slope for the Bell-Berry stomatal model is quite stable. The values of V_{cmax}, J_{max} and R_d are normalized to 25 °C according to Equations 8 and 9 of Harley et al. (1992), and the temperature coefficients were from Bernacchi et al. (2001). A complete list of model parameters and the derived physiological parameters are listed in Table 4.2.

Table 4.2. Physiological and other parameters

Parameter	Description	Value (Unit)	Source
Photosynthesis and respiration			
α	quantum yield	0.24 (mol electron mol^{-1} photon)	XB2003
K_c	Michaelis-Menten constant for CO_2 (25°C)	275 μmol mol^{-1}	H1992
K_o	Michaelis-Menten constant for O_2 (25°C)	420 mmol mol^{-1}	H1992
τ	Rubisco specificity factor	2321	H1992
Activation energy for temperature dependency			
ΔH_a (K_c)		79.43 kJ mol^{-1}	B2001
ΔH_a (K_o)		36.38 kJ mol^{-1}	B2001
ΔH_a (τ)		-29.0 kJ mol^{-1}	B2001
ΔH_a (R_d)		46.39 kJ mol^{-1}	B2001
ΔH_a (V_{cmax})		65.33 kJ mol^{-1}	B2001
ΔH_a (J_{max})		79.5 kJ mol^{-1}	H1992
Deactivation energy for temperature dependency			
ΔH_d (V_{cmax})		202.9 kJ mol^{-1}	H1992
ΔH_d (J_{max})		201.0 kJ mol^{-1}	H1992
Entropy term for temperature dependency			
ΔS (V_{cmax})		0.65 kJ K^{-1} mol^{-1}	H1992
ΔS (J_{max})		0.65 kJ K^{-1} mol^{-1}	H1992
Stomatal conductance			
a_0	Intercept for Ball-Berry model	0.006 (mol m^{-2} s^{-1})	XB 2003

a_1	Slope for Ball-Berry model	8.88	XB 2003
<u>Other</u>			
	average leaf size	0.025 m	

Note: XB 2003 (Xu and Baldocch 2003); B2001 (Bernacchi et al., 2001); H1992 (Harley et al., 1992)

4.2.3 Meteorology

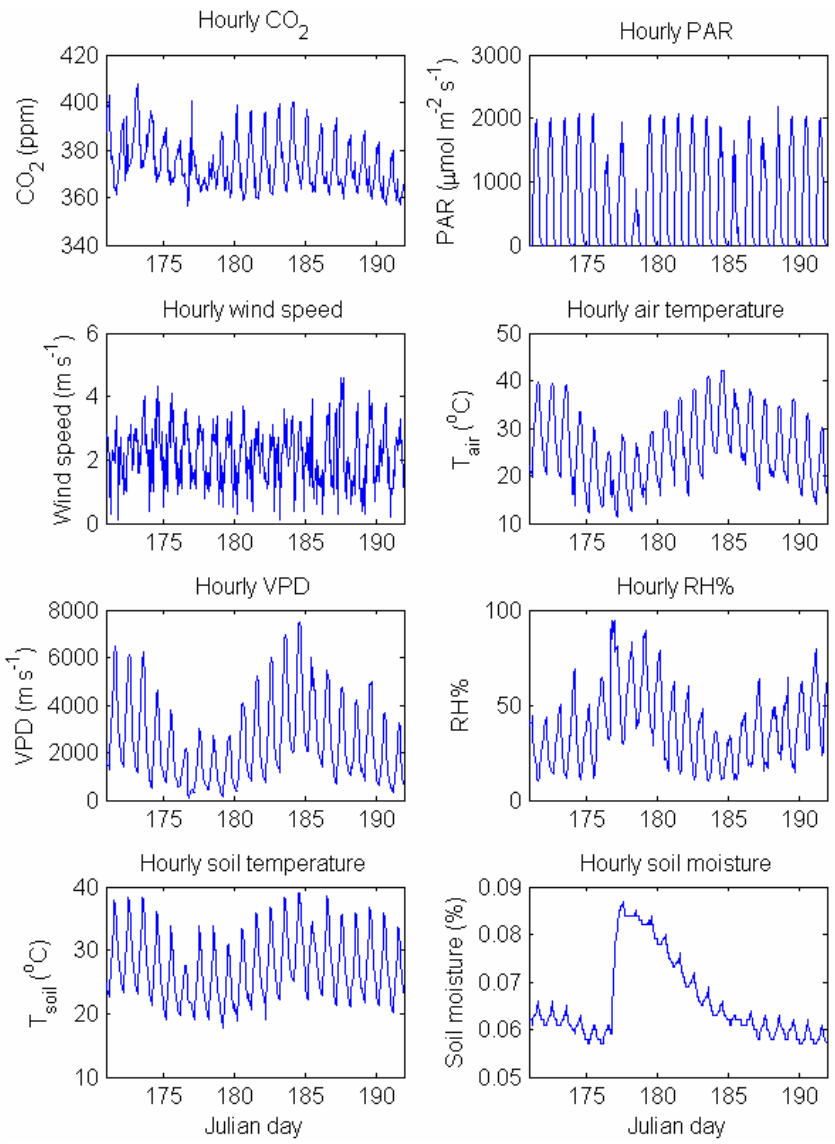

Figure 4.4. Meteorological data measured in the site

A large number of meteorological variables are measured in the site, including solar radiation, PAR, air temperature, relative humidity, volumetric soil moisture content, wind velocity, and carbon dioxide concentration (Baldocchi et al., 2004). We used the data between June 20 and July 10 in 2001 to run the model because 1) leaves are still active in photosynthesis, 2) the understory grass are dead so that trees are the only biota for photosynthesis, and 3) there is a slight amount of rainfall within this period so that there is larger variation of fluxes (Figure 4.4).

4.2.4 Spectral properties

We measured the leaf and soil reflectance with a spectroradiometer. For leaves, the reflectance is 0.08 and 0.52 for the PAR and NIR wavelengths, respectively. For soil, the reflectance is 0.1 and 0.25 for the PAR and NIR wavelengths, respectively. Other spectral properties are from the literature: the transmissivity of leaves is 0.1 and 0.4 for the PAR and NIR wavelengths; the soil reflectance and leaf transmissivity at the thermal wavelength is 0.1 and 0.05, respectively (Goudriaan 1977).

4.3 Eddy covariance CO2 flux

There are two eddy covariance systems, one at 23m and the other at 2m above the ground, to measure the CO_2, water, and energy fluxes simultaneously. Net ecosystem carbon exchange (NEE) was calculated with in-house software by processing the measurements into flux densities, correcting the canopy CO_2 storage, and filling in the missing data (Baldocch et al., 2003). Ecosystem respiration was estimated based on the statistical relationships between nighttime NEE and soil temperature at 4cm depth

for measurements with friction velocity greater than 0.1 m s^{-1}. Gross primary productivity is the difference between NEE and ecosystem respiration.

5 Results and Discussion

5.1 Comparison with eddy covariance measurements

Figure 4.5 (a)-(c) shows the comparison between the GPP derived from the eddy covariance measurements and the photosynthesis simulated from the individual-tree model. During the daytime, the mean GPP derived from the flux measurement is -2.04 ± 3.49 µmol m^{-2} s^{-1}. The photosynthesis from the individual-tree model is -2.68 ± 1.42 µmol m^{-2} s^{-1}, which overestimate the flux measurements by 31%. It is interesting that there is almost no difference between the fluxes estimations from individual-tree and big-leaf models. The big-leaf model produced a flux density of -2.71 ± 1.46µmol m^{-2} s^{-1}. The mean square error between individual-tree and big-leaf model is negligible (0.005 µmol m^{-2} s^{-1}).

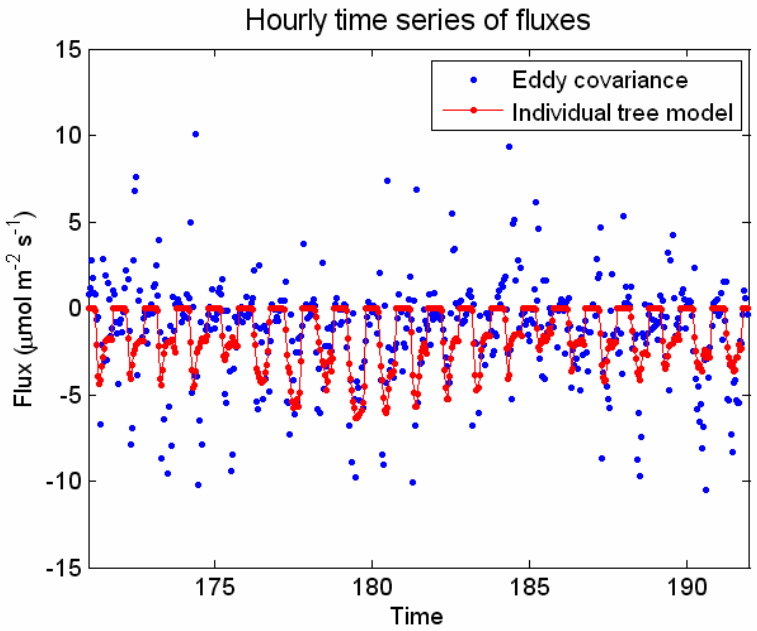

(a)

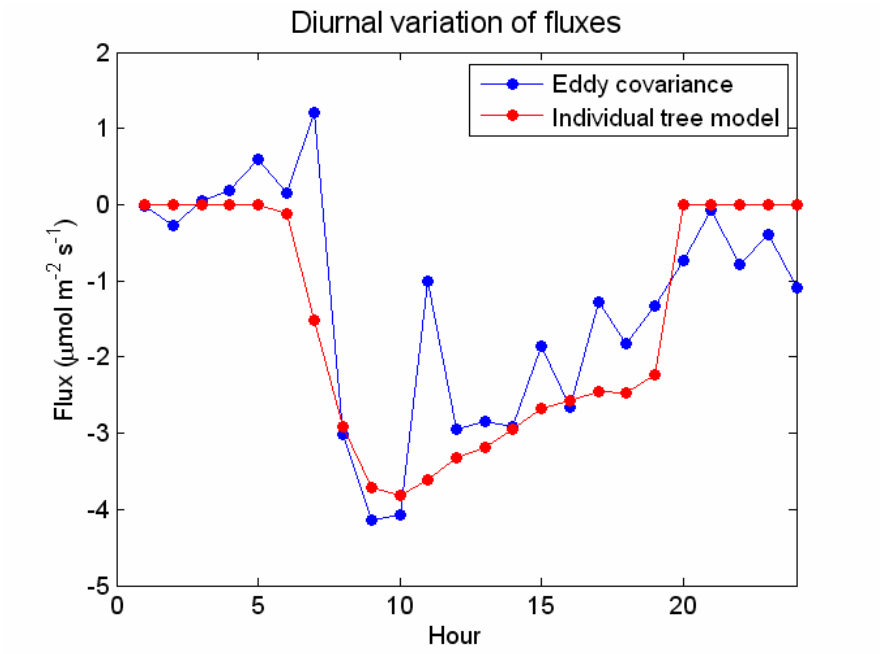

(b)

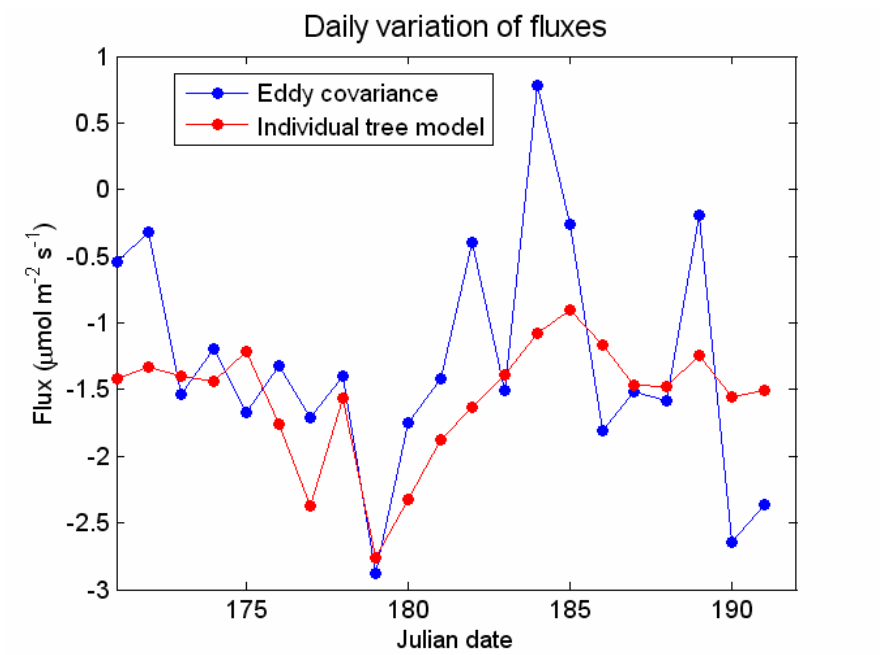

(c)

Figure 4.5 Comparison between individual-tree model simulation and eddy covariance measurements

5.2 Comparison between individual-tree, big-leaf, and Markov models

Since there is almost no difference between individual-tree and big-leaf models for modeling photosynthesis, we tried to examine how these two models differ under

other scenarios, especially for different canopy covers and leaf area index. The canopy cover of the site is 0.47. First of all, we randomly remove a certain number of trees so that the canopy cover varies from 0.4, 0.3, 0.2, to 0.1. For each canopy cover, we multiplied the leaf areas of each tree with a certain constant so that local LAI changes from 0.5, 1, 1.5, 2, 2.5, 3, 3.5, 4, to 4.5, where local LAI is the leaf area index for the canopy only. Therefore, there are a total of 36 different settings for the landscape. For each setting, we run the individual-tree, big-leaf, and Markov big-leaf models. The modeled canopy CO_2 assimilation is shown in Figure 4.6.

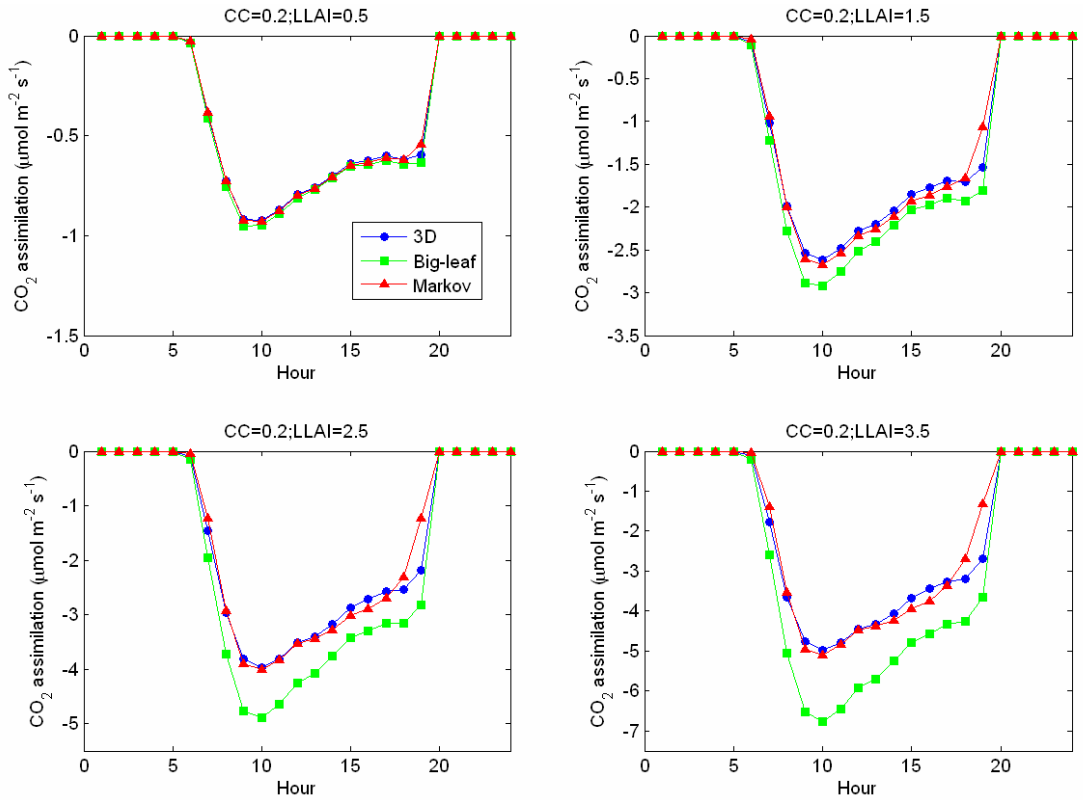

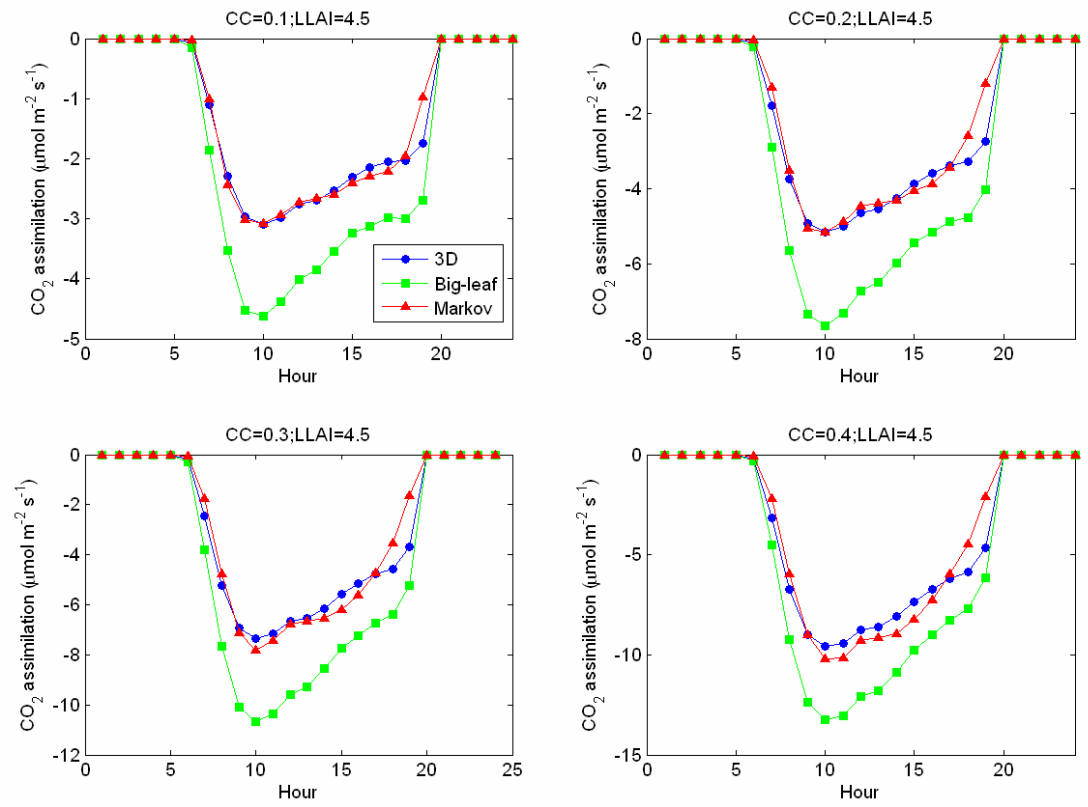

Figure 4.6 Comparison of individual, big-leaf, and Markov big-leaf models for modeling diurnal variation of canopy CO_2 assimilation. CC stands for canopy cover (CC) and LLAI stands for local leaf area index

The results show that 1) the Markov big-leaf model has much better estimation of assimilation than the big-leaf model when compared to the individual-tree model, 2) the big-leaf model constantly overestimates assimilation when compared to the individual-tree model, and 3) the Markov big-leaf model could overestimate or underestimate the assimilation. The overestimation of CO_2 assimilation by big-leaf model agrees well with the findings from previous studies because the big-leaf model will overestimate the light interception. It is very encouraging that the Markov big-leaf model has a close match with the individual-tree model. The discrepancy

between the Markov big-leaf model and the individual-tree model could be caused by a number of factors. For example, when we derive the clumping factor, we assume the trees are regularly distributed; however, the trees in a landscape might be clumped or patched. Also, the trees are assumed to be boxes instead of ellipsoids used in the individual-tree model.

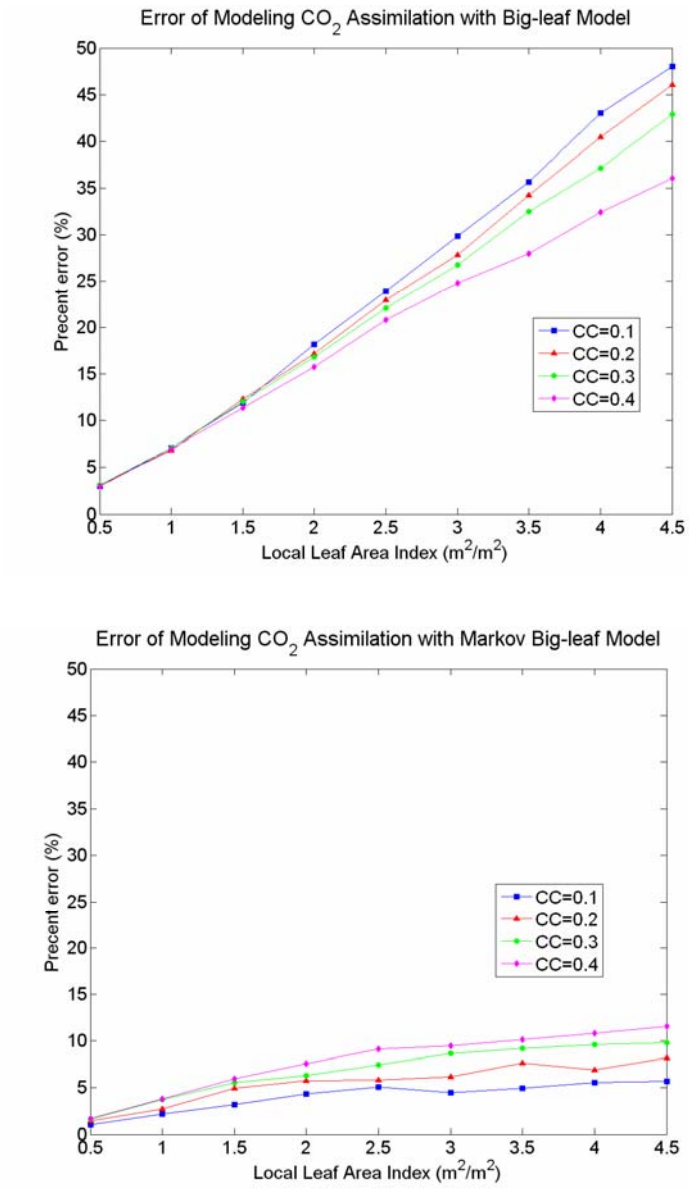

Figure 4.7 The dependence of percent errors of the big-leaf model and the Markov big-leaf model on canopy cover and local LAI.

To investigate the effects of canopy cover and local leaf area index on modeling errors, we calculate the root mean square root errors of the daytime assimilation fluxes for both the big-leaf model and Markov big-leaf model by assuming the individual-tree model to be the truth. We also calculate the percent error, which is the ratio between the mean square root error and mean flux density of the individual-tree model. The percent error increases with the local LAI for both the big-leaf and Markov big-leaf models (Figures 7). When local LAI is as small as 0.5 m^2/m^2, the errors for both models are very small. This means that there are not much difference between individual-tree model, big-leaf, and Markov big-leaf models for CO_2 assimilation estimation if LAI is small. For big-leaf models, the percent error could be as high as nearly 50% when local leaf area index is 4.5; however, the maximum percent error for the Markov big-leaf model is only about 10%.

Big-leaf model and Markov big-leaf model show different patterns of errors depending on canopy cover. For big-leaf model, the errors decrease with canopy cover. This is reasonable because canopy is more like a big-leaf as canopy cover increases. However, for Markov big-leaf model, the errors increase with canopy cover. This can be explained by the approach of calculating clumping factors. Larger canopy cover implies smaller tree spacing. Our analysis in the next section shows that the clumping factor is more sensitive to tree spacing when trees are close to each other. So, a small error in setting the tree spacing could cause a large variation of clumping factor, therefore, a larger error in carbon flux estimation.

5.3 Variation of clumping factors

Table 4.3. Parameter values and ranges used in the simulation.

Parameter	Description	Base value (Unit)	Range
h	Tree height vs. crown size ratio	10	(0 20)
l	Tree spacing vs. crown size ratio	1	(0 10)
ρ	Leaf area volume density	0.2 (m^2/m^3)	(0 1)
G	G-function value	0.5	(0 1)
θ	Solar zenith angle	45 (degree)	(0 90)

To examine how clumping factors vary with the independent variables, we set up a set of base values and their ranges for all of the five input parameters (see Table 4.3). Each time we change one of the parameters and fix the rest four (Figures 8(a), (c), (d), (e), and (f)). When tree spacing to crown width ratio (l) is zero, the clumping factor is 1 because the canopy is just like a big-leaf (Figure 4.8(a)). As l increases, it is interesting to see that the clumping factor drops quickly at the very beginning and then increases when l is around 1. The clumping factor seems to decrease with crown depth to crown size ratio (h), leaf area volume density (ρ), and G-function value (G) (Figures 8(c), (d), and (e)). When the leaf area volume density is small, the clumping factor is close to 1. This can explain why the individual-tree, big-leaf, and Markov big-leaf models have similar performance when local LAI is small (Figure 4.6). Clumping factors have no monotonic relationship with solar zenith angle. In Figure 4.8(f), the clumping factor first increases with solar zenith angle, reaches a maximum around 10°, and then decreases to 0 when the solar zenith angle is 90°. This is interesting because it implies that the canopy looks mostly random when the solar zenith angle is some value between 0 and 90°. The clumping factor changes slowly

when solar zenith angle is in the intermediate range and drops quickly when solar zenith angle is approaching to 90°.

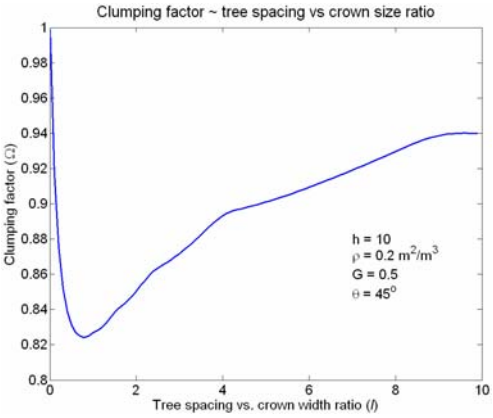

(a)

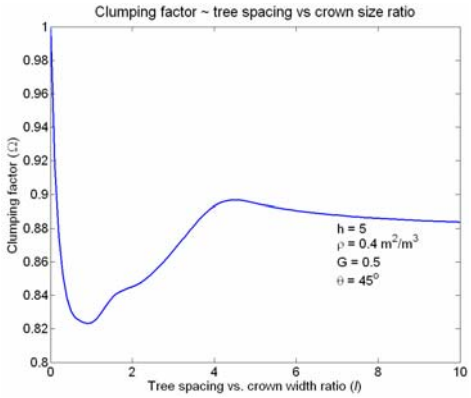

(b)

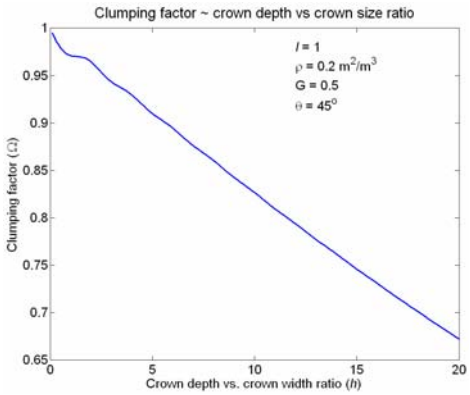

(c)

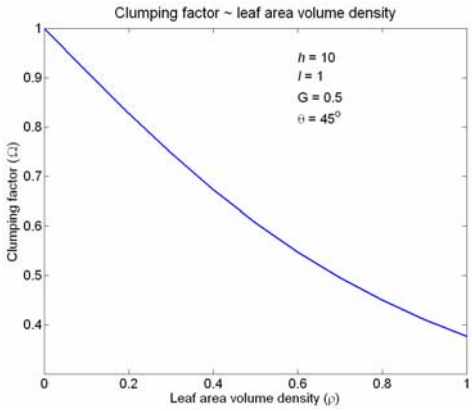

(d)

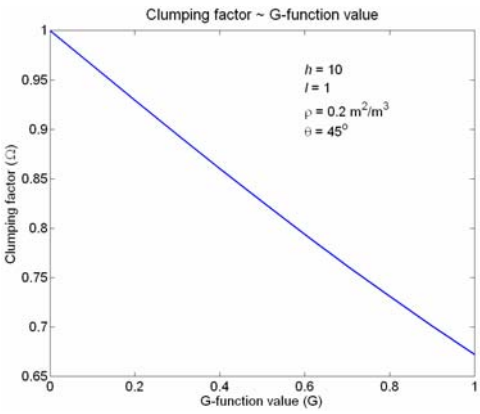

(e)

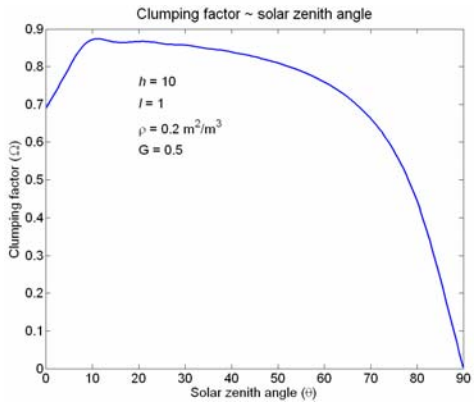

(f)

Figure 4.8 The variation of clumping factors depending on its input parameters.

It is worthwhile to notice that all of the discussions above only apply to the base

values of the parameters. The clumping factors might exhibit different patterns when any of the input parameters changes. For example, if we change the values of crown depth to crown size ratio (h) and leaf area volume density (ρ), the clumping factors have a different pattern depending on the tree spacing to crown width ratio (l). The usefulness of our analytical approach is evident because we do not need develop different equations for predicting the values of clumping factors according to different input parameters.

Also, our approach can be used to test the results summarized in previous literature. For example, Asrar et al. (1992) concluded that local leaf area index is a very useful parameter for modeling radiation for heterogeneous landscapes. Figures 8(a) and (b) have the same local leaf area index (2 m^2/m^2). When l is small, they do have similar values of clumping factors. However, the clumping factor decreases when $l>5$ in Figure 4.8(b) although it increases in Figure 4.8(a). This indicates that Asrar et al.'s conclusion holds only under certain circumstances.

6 Conclusions

This study presents an analytical approach to calculate clumping factors for heterogeneous landscapes and uses it in the Markov big-leaf model for modeling CO_2 assimilation of canopy. It was found that the CO_2 assimilation estimated by the Markov big-leaf model can closely match the one by the individual-tree based model for landscapes with different canopy cover and local leaf area index. It is expected that our approach can significantly improve our ability of predicting ecosystem

functions for heterogeneous landscapes from regional to global scales. Research is needed to explore how to estimate the input parameters at the broader spatial scales with remote sensing technologies such as LIDAR and MISR (Multiangle Imaging SpectroRadiometer).

Reference

Allen, L.H., 1974. A model of light penetration in a wide row crop, *Agronomy Journal* 66: 41-7

Asrar, G., Myneni, R.B. and Choudhury, B. J., 1992. Spatial heterogeneity in vegetation canopies and absorbed photosynthetically active radiation: A modeling study. *Remote Sens. Environ.*, 41: 85-103.

Andrieu, B., and Sinoquet, H., 1993, Evaluation of structure description requirements for predicting gap fraction of vegetation canopies. *Agricultural and Forest Meteorology*, 65, 202-227.

Ball, J.T., Woodrow, I.E., and Berry, J.A., 1987. A model predicting stomatal conductance and its contribution to the control of photosynthesis under different environmental conditions. In Progress in Photosynthesis Research, ed. J Biggins. M Nijhoff, Dordrecht, Vol. 4, pp 221-224.

Baldocchi, D. D., L. Xu, and N. Kiang, 2004. How plant functional-type, weather, seasonal drought, and soil physical properties alter water and energy fluxes of an oak-savanna and an annual grassland," *Agricult.Forest Meteorol.*, vol. 123, pp. 13–39.

Bernacchi, CJ, Singsaas, EL, Pimentel, C, Portis, Jr. AR and Long, SP, 2001. Improved temperature response functions for models of Rubisco-limited

photosynthesis. *Plant, Cell & Environment*, 24, 253-260.

Bond, W.J., Midgley, G.F., Woodward, F.I., 2003. The importance of low atmospheric CO 2 and fire in promoting the spread of grasslands and savannas. *Global Change Biology* 9:973-982

Charles-Edwards, D.A., and M.R. Thorpe, 1976. Interception of diffuse and direct beam radiation by a hedgerrow apple orchard. *Annals of Botany*, 40 :603-613.

Chen, Q., 2007, Airborne lidar data processing and information extraction, *Photogrammetric Engineering & Remote Sensing*, 73(2), 109-112

Chen Q., D.D. Baldocchi, P. Gong & M. Kelly, 2006. Isolating Individual Trees in a Savanna Woodland using Small Footprint LIDAR data. *Photogrammetric Engineering & Remote Sensing*, 72, 923-932.

Chen, Q., P. Gong, D.D. Baldocchi, and G. Xie., 2007, Filtering airborne laser scanning data with morphological methods, *Photogrammetric Engineering & Remote Sensing*, 73(2), 175-185

Farquhar, G.D., S. von Caemmerer, and J.A. Berry, 1980. A Biochemical Model of Photosynthetic CO2 Assimilation in Leaves of C3 species. *Planta* 149:78-90.

Farquhar, G.D. and S.C.Wong, 1984. An empirical model of stomatal conductance. *Aust. J. Plant Physiol*. 11:191–210.

Goudriaan J. 1977. Crop micrometeorology: a simulation study. Simulation Monographs. Wageningen (Netherlands): Pudoc. 257 pp.

Harley, P.C., R.B. Thomas, J.F. Reynolds and B.R. Strain. 1992. Modelling photosynthesis of cotton grown in elevated CO2. *Plant, Cell & Environment* 15,

271-282.

Jarvis, P.G., Leverenz, J.W., 1983. Productivity of temperate, deciduous and evergreen forests. In: Lange, O.L., Nobel, P.S., Osmond, C.B., Ziegler, H. (Eds.), *Encyclopedia of Plant Physiology*, 12D Physiological Plant Ecology IV. Ecosystem Processes: Mineral Cycling, Productivity and Man's Influence. Springer-Verlag, Berlin, pp. 234–280.

Kucharik, C.J., J.M. Norman, L.M. Murdock, and S.T. Gower, 1997. Characterizing canopy nonrandomness with a Multiband Vegetation Imager (MVI). *Journal of Geophysical Research*, 102(D24): 29,455-29,473.

Mariscal MJ, Martens SN, Ustin SL, Chen J, Weiss SB, Roberts DA., 2004. Light transmission profiles in an old-growth forest canopy: simulations of photosynthetically active radiation by using spatially explicit radiative transfer models. *Ecosystems* 23 7:454–467.

Medlyn, BE, 2004. A MAESTRO Retrospective. In: "*Forests at the Land-Atmosphere Interface*" Eds. M. Mencuccini, J.C. Grace, J. Moncrieff and K. McNaughton. CAB International. pp. 105-121.

Norman, J.M. and Jarvis, P.G., 1975. Photosynthesis in Sitka spruce (*Picea sitchensis* (Bong.) Carr.) V. Radiation penetration theory and a test case. *Journal of Applied Ecology* 12, 839-878.

Norman, J.M. 1979. Modeling the complete crop canopy. In *Modification of the Aerial Environment of Plants*. Eds. B.J. Barfield and J.F. Gerber. American Society of Agricultural Engineers, Michigan, pp 249--277.

Norman, J.M. and Welles, J.M., 1983. Radiative transfer in an array of canopies. *Agronomy Journal* 75, 481-488.

Ramankutty N, Foley J.A., 1999. Estimating historical changes in global land cover: croplands from 1700 to 1992. *Global Biogeochemical Cycles,* 13, 997-1027.

Sankaran, M. Hanan, N., Scholes, R.J., and 24 others including K.K. Caylor, 2005. Determinants of woody cover in African savannnas: A continental scale analysis, *Nature*, doi:10.1038/nature04070.

Wang, Y.P. & Jarvis, J.P., 1990. Description and validation of an array model-MAESTRO. *Agricultural and Forest Meteorology* 51, 257-280.

Xu L, Baldocchi DD. 2003. Seasonal trend of photosynthetic parameters and stomatal conductance of blue oak (Quercus douglasii) under prolonged summer drought and high temperature, *Tree Physiology* 23, 865-877.